

Universidade de São Paulo
Instituto de Física

O impacto de efeitos sistemáticos sobre a escada de distâncias cósmicas

Alexandra Turmina Petreca

Orientador: Prof. Dr. Edivaldo Moura Santos

Dissertação de mestrado apresentada ao Instituto de Física da Universidade de São Paulo, como requisito parcial para a obtenção do título de Mestre(a) em Ciências.

Banca Examinadora:

Prof. Dr. Edivaldo Moura Santos - Orientador (IF - USP)

Prof. Dr. Laerte Sodré Junior (IAG - USP)

Prof. Dr. Miguel Quartin (IF - UFRJ)



São Paulo
2024

FICHA CATALOGRÁFICA
Preparada pelo Serviço de Biblioteca e Informação
do Instituto de Física da Universidade de São Paulo

Petrecá, Alexandra Turmina

O impacto de efeitos sistemáticos sobre a escada de distâncias cósmicas. São Paulo, 2024.

Dissertação (Mestrado) – Universidade de São Paulo, Instituto de Física, Departamento de Física Experimental
Orientador(a): Prof^o Dr^o Edivaldo Moura Santos

Área de Concentração: Física

Unitermos: 1. Cosmologia; 2. Constante de Hubble; 3. Escada de distâncias cósmicas

USP/IF/SBI-006/2024

University of São Paulo
Physics Institute

The impact of systematic effects on the cosmic distance ladder

Alexandra Turmina Petreca

Supervisor: Prof. Dr. Edivaldo Moura Santos

Dissertation submitted to the Physics Institute of the
University of São Paulo in partial fulfillment of the
requirements for the degree of Master of Science.

Examining Committee:

Prof. Dr. Edivaldo Moura Santos - Supervisor (IF - USP)

Prof. Dr. Laerte Sodré Junior (IAG - USP)

Prof. Dr. Miguel Quartín (IF - UFRJ)

São Paulo
2024

À minha mãe, Neres

Agradecimentos

Gostaria de agradecer primeiramente ao meu orientador, professor Edivaldo, pela imensa paciência ao me instruir nesta etapa da minha trajetória acadêmica, pela dedicação aplicada em todas as atividades que desenvolvemos juntos e pelo esmero demonstrado no decorrer do meu projeto de mestrado. São incontáveis as suas contribuições tanto para este trabalho quanto para o meu amadurecimento acadêmico durante o desenvolvimento dele. Sou profundamente grata pelos aprendizados e pelas experiências e oportunidades que pude vivenciar graças ao seu apoio e incentivo.

Um agradecimento especial ao Adam Riess, pelos direcionamentos nos estágios iniciais deste trabalho aos repositórios de dados e códigos apropriados do SH0ES/Pantheon+, e aos professores Laerte Sodré Junior e Miguel Quartin por aceitarem o convite para compôr a banca avaliadora e por revisarem detalhadamente a presente dissertação.

Agradeço também ao Dr. Ronaldo Carlotto Batista pelas discussões durante as nossas reuniões semanais, as quais contribuíram grandemente para o andamento do projeto. E também ao grupo do Journal Club que, apesar das significativas contribuições para a pesquisa por meio de comentários e apresentações em nossas reuniões, será lembrado com muito carinho pelo companheirismo e esportividade. Aos demais amigos do IF, pela companhia, pelo apoio concedido em todas as fases do mestrado e por todos os momentos especiais que passamos juntos.

Aos meus pais, por todo o suporte fornecido e carinho dedicado a mim não só nesta etapa da minha vida, mas também nas que a antecederam. Nada disso teria sido possível sem o apoio imensurável que recebi de vocês ao longo de toda a minha trajetória.

Por fim, gostaria de agradecer à responsável por supervisionar a parte deste projeto desenvolvida na Itália, Dr. Micol Benetti, pelo seu empenho aplicado ao trabalho que desenvolvemos, entusiasmo demonstrado em todos os assuntos que estudamos e também pelo cuidado e preocupação que manifestou buscando me inserir no SPACE. Para mim foi um prazer trabalhar com você neste curto período de tempo que, apesar de breve, foi o suficiente para que eu pudesse desenvolver habilidades ainda não experimentadas no Brasil. Agradeço também ao professor Salvatore Capozziello e ao Dr. Rocco D'Agostino por todas as conselhos e discussões neste período e, também à todos que tive o imenso prazer de conhecer na Scuola Superiore Meridionale.

O presente trabalho teve apoio da Fundação de Amparo à Pesquisa do Estado de São Paulo (FAPESP), nº do processo 2021/13752-7 e apoio da CAPES, Coordenação de Aperfeiçoamento de Pessoal de Nível Superior, processo 8887.639564/2021-00. Além disso, parte

da dissertação resulta do projeto desenvolvido com a Bolsa Estágio de Pesquisa no Exterior FAPESP, nº 2022/14565-9. As opiniões, hipóteses e conclusões ou recomendações expressas neste material são de responsabilidade do autor e não necessariamente refletem a visão da FAPESP.

O trabalho foi desenvolvido com recursos computacionais da Superintendência de Tecnologia da Informação da Universidade de São Paulo (USP) e do Observatório Nacional (ON).

“Science, my lad, is made up of mistakes, but they are mistakes which it is useful to make because they lead little by little to the truth.”

(Verne, Jules; **A Journey to the Centre of the Earth**, 1864.)

Abstract

The main objective of this work is to analyze possible residual systematic effects associated with the determination of the Hubble constant (H_0). This is done by investigating the problem from an experimental point of view, through analysis and modeling of real and synthetic data used as input for the cosmic distance ladder method, and from a theoretical point of view, proposing a new model for the background evolution of the Universe. In the data analysis and modeling part, synthetic data samples were generated capturing all the important features of real data coming from cepheids and type Ia supernovae (SNeIa) made available by SH0ES and Pantheon+ teams. Systematic errors were added to these samples in order to check their impact on several parameters of the cosmic distance ladder, especially on H_0 . We verified claims in the literature that order 0.5% biases on apparent magnitudes of Supernovae (SNe) are enough to shift H_0 by a few $\text{km s}^{-1} \text{Mpc}^{-1}$, as long as they are not uniform across the second and third rungs of the ladder, that is, the calibration and Hubble flow samples. On the other hand, we show that H_0 and the absolute magnitudes of cepheids and supernovae are strongly protected against biases affecting cepheids metallicities. We also studied, using real and synthetic datasets, the impact on the distance ladder parameters of different SNeIa color correction models. Particular attention was given to a model where SNeIa from the calibration and the Hubble flow samples have different color slopes, as this effect has been recently claimed to solve the so called Hubble tension. Our results regarding such a color slope effect are inconclusive so far, but further studies are planned. Finally, a hybrid approach combining the standard cosmological model and cosmography was proposed to determine H_0 . Three orders of the so called Padé series (P_{21} , P_{22} and P_{32}) were used to parameterize the dark energy density contribution to the background evolution. The constraints on the cosmological parameters were made using CosmoMC, with data from CMB, baryonic acoustic oscillations, cosmic clocks and type Ia supernovae. The values of H_0 obtained with this hybrid approach are consistent with the one obtained from the CMB anisotropies assuming a spatially-flat Λ CDM cosmology.

Key-words: the Hubble tension, the cosmic distance ladder, the f(z)CDM approach.

Resumo

O objetivo principal do presente trabalho é analisar possíveis erros sistemáticos residuais associados à determinação da constante de Hubble (H_0). Isso é feito investigando o problema do ponto de vista experimental, através da análise e modelagem dos dados (reais e sintéticos) utilizados como entrada no método de escada de distâncias cósmicas, e do ponto de vista teórico, propondo um novo modelo para evolução de *background* do Universo. Na parte de análise e modelagem dos dados, amostras sintéticas foram geradas levando em consideração todas as características importantes dos dados reais de cefeidas e supernovas do tipo Ia disponibilizados pelas equipes SH0ES e Pantheon+. Erros sistemáticos foram adicionados a essas amostras com o intuito de verificar os seus impactos em vários parâmetros da escada de distâncias cósmicas, especialmente em H_0 . Verificamos afirmações da literatura de que desvios da ordem de 0.5% nas magnitudes aparentes das supernovas são suficientes para deslocar H_0 em alguns $\text{km s}^{-1} \text{Mpc}^{-1}$, desde que os desvios não sejam uniformes ao longo do segundo e terceiro degrau da escada de distância, ou seja, as amostras de calibração e do fluxo de Hubble. Por outro lado, mostramos que H_0 e as magnitudes absolutas das cefeidas e supernovas estão fortemente protegidas contra os enviesamentos que afetam as metalicidades das cefeidas. Estudamos também o impacto de diferentes modelos de correção de cor das supernovas nos parâmetros da escada de distância. Foi dada particular atenção a um modelo em que as supernovas das amostras de calibração e do fluxo de Hubble têm diferentes inclinações de cor, uma vez que este efeito foi recentemente proposto para resolver a chamada tensão de Hubble. Os nossos resultados relativos a este efeito de inclinação de cor são inconclusivos até o momento, mas estão sendo planejados novos estudos sobre o tema. Finalmente, foi proposta uma abordagem híbrida que combina o modelo cosmológico padrão e a cosmografia para determinar H_0 . Três ordens das chamadas séries de Padé (P_{21} , P_{22} e P_{32}) foram utilizadas para parametrizar a contribuição da energia escura para a evolução de *background*. As restrições dos parâmetros cosmológicos foram feitas através do CosmoMC, com dados da radiação cósmica de fundo (RCF), oscilações acústicas bariônicas, relógios cósmicos e supernovas do tipo Ia. Os valores de H_0 resultantes dessa abordagem híbrida são consistentes com o valor obtido via anisotropias da RCF em uma cosmologia do tipo Λ CDM espacialmente plana.

Palavras-chave: Tensão de Hubble, escada de distâncias cósmicas, abordagem $f(z)$ CDM.

List of Figures

2.1 Differences between the angular resolution of each satellite: COBE, WMAP and Planck.	7
2.2 Power spectra of the CMB temperature anisotropies varying cosmological parameters: τ , ω_b , Θ_{MC} , ω_c , $\ln(10^{10}A_s)$ and η .	13
2.3 H_0 as a function of Θ_{MC} .	16
3.1 The cosmic distance ladder.	20
3.2 One diagram explaining how geometric parallax works (on the left) and one period-luminosity diagram (on the right).	21
3.3 Light curves of supernovae before and after standardization via stretch and color parameters.	23
3.4 Light curves in different bands of the Sloan Digital Sky Survey (SDSS) for the example data set from SNCosmo [1]. This data set is synthetic and was generated based on the real sample of the SDSS.	24
3.5 Light curves in different bands of SDSS in which the parameters c and x_1 are changed.	25
3.6 Distributions of apparent magnitudes of SHOES cepheids in the LMC, separated by telescopes: Gaia and Hubble Space Telescope (HST).	31
3.7 Apparent magnitudes of SHOES first rung cepheids versus the period in logarithmic scale.	32
3.8 Sky maps for the cepheids from the first and second rung.	33
3.9 Sky maps for the supernovae from the second and the third rung.	34
3.10 Histograms of residuals for the real data of the first rung cepheids in the distance ladder, separated into anchors.	36
3.11 Histograms of the real data of the first and second rung cepheids in the distance ladder.	37
3.12 Histograms of the real data of the second and third rung SNeIa in the distance ladder.	37
3.13 Corner plots considering real data based on data from Riess et al. (2022).	40
3.14 Histograms of the real data of the second and third rung SNeIa obtained from Pantheon+.	42

3.15	Graphs of the distance modulus as a function of the redshift of the supernovae and two theoretical predictions of $\mu_0(z)$, one considering $H_0 = 67.36 \text{ km s}^{-1} \text{ Mpc}^{-1}$ and another considering $H_0 = 73.04 \text{ km s}^{-1} \text{ Mpc}^{-1}$.	43
3.16	Histograms of Δmag considering H_0 equal to 73.04 and 67.36 $\text{km s}^{-1} \text{ Mpc}^{-1}$.	43
4.1	H_0 and M_B as a function of the magnitude of a hypothetical bias on the apparent magnitudes of 2 nd rung synthetic SNeIa.	46
4.2	H_0 and M_B as a function of the magnitude of a hypothetical bias on the apparent magnitudes of 3 rd rung synthetic SNeIa.	47
4.3	H_0 and M_B as a function of the magnitude of a hypothetical bias affecting the apparent magnitudes of 2 nd and 3 rd rung synthetic SNeIa, simultaneously. The systematic errors are given in units of the statistical fluctuations $\sigma_{\text{stat}} = 0.098$ mag and $\sigma_{\text{stat}} = 0.135$, respectively.	48
4.4	H_0 and M_B as a function of the magnitude of a hypothetical uniform bias affecting the apparent magnitudes of 2 nd and 3 rd rung synthetic SNeIa, simultaneously. The systematic error is given in units of the statistical fluctuation $\sigma_{\text{stat}} = 0.15$ mag.	49
4.5	H_0 and M_H^W as a function of the magnitude of a hypothetical uniform bias affecting the metallicities of synthetic cepheids.	51
4.6	Corner plots considering synthetic data only and with a systematic error (0.098 mag) on the apparent magnitudes of the 2 nd rung SNeIa.	54
4.7	Corner plots considering synthetic data only and with a systematic error (0.135 mag) on the apparent magnitudes of the 3 rd rung SNeIa.	55
4.8	Corner plots considering synthetic data only and with systematic errors of 0.098 and 0.135 mag on the apparent magnitudes of the 2 nd and 3 rd rung SNeIa, respectively.	56
4.9	Corner plots considering synthetic data only and with a systematic error of 0.15 mag on the apparent magnitudes of the 2 nd and 3 rd rung SNeIa, simultaneously.	57
4.10	Corner plots considering synthetic data only and with a systematic error (0.25 dex) on the metallicity data of all cepheids.	58
5.1	Graphics of the theoretical distance modulus of supernovae $\mu_0(H_0, q_0, j_0, z)$ versus their experimental distance modulus $\mu_0 = m_B - M_B$ and of the color from the supernovae in function of their redshift.	60

5.2	On the left: plot of uncorrected apparent magnitudes as a function of color of all supernovae together with the fitted lines for each sample. On the right: histogram of pulls of real data from second and third rung supernovae selected on Pantheon+, considering a standard color correction model.	63
5.3	Histograms of residuals of the second and third rung supernovae real data, considering a color correction standard model.	64
5.4	Histograms of residuals of the second and third rung supernovae real data, considering a model with two color correction coefficients (β_{cal} and β).	66
5.5	Histograms of residuals from the synthetic data of the second and third rung supernovae, residuals were calculated considering a model with two color correction coefficients and a reference color.	68
6.1	Luminosity distance compared with Pantheon+ catalog, considering three different orders of the Padé series and the Taylor series.	76
6.2	d_L vs z considering P_{21} , P_{22} , P_{32} and the Taylor expansion with $q_0 = -0.2$, $q_0 = -0.55$, $q_0 = -1$, $j_0 = 1$, $j_0 = 2$ and $j_0 = 3$	77
6.3	The background evolution compared with Cosmic Chronometers data, considering three different orders of Padé series together with the Taylor series expansion.	78
6.4	P_1 , P_2 , P_3 , Q_1 and Q_2 coefficients behavior as a function of q_0 and j_0 for the three Padé series.	80
6.5	P_1 , P_2 , P_3 , Q_1 and Q_2 coefficients behavior as a function of s_0 for the three Padé series.	81
6.6	The \bar{q}_0 and \bar{j}_0 parameters from $f(z)$ CDM model as functions of the q_0 and j_0 cosmographic parameters, respectively.	84
6.7	Plots of $\bar{H}(z)$ as a function of z for three cases: considering P_{21} , P_{22} and P_{32} . Two redshift ranges are considered: $z < 2$ and $z < 10$	84
6.8	Posterior distributions for the cosmological and cosmographic parameters of the $f(z)$ CDM model.	88
B.1	All fitted parameters as a function of the magnitude of a hypothetical bias on the apparent magnitudes of 2 nd rung synthetic SNeIa. The systematic errors are given in units of the statistical fluctuation $\sigma_{\text{stat}} = 0.098$ mag.	94
B.2	All fitted parameters as a function of the magnitude of a hypothetical bias on the apparent magnitudes of 3 rd rung synthetic SNeIa. The systematic errors are given in units of the statistical fluctuation $\sigma_{\text{stat}} = 0.135$ mag.	95

B.3	All fitted parameters as a function of the magnitude of a hypothetical bias on the apparent magnitudes of 2 nd and 3 rd rung synthetic SNeIa. The systematic errors are given in units of the statistical fluctuations $\sigma_{\text{stat}} = 0.098$ mag and $\sigma_{\text{stat}} = 0.135$ mag, respectively.	97
B.4	All fitted parameters as a function of the magnitude of a hypothetical bias on the apparent magnitudes of 2 nd and 3 rd rung synthetic SNeIa. The systematic errors are given in units of the statistical fluctuation $\sigma_{\text{stat}} = 0.15$.	98
B.5	All fitted parameters as a function of the magnitude of a hypothetical bias on the metallicity data of cepheids. The systematic errors are given in units of the statistical fluctuation $\sigma_{\text{stat}} = 0.05$ dex.	100

List of Tables

2.1	Summary of the base- Λ CDM+ Ω_k parameters and their values obtained from the best fit performed by the Planck collaboration using the so called TT+TE+EE+lowE+lensing combined likelihood.	12
3.1	Fitted values obtained through χ^2 analysis and the median values taken from MCMC, considering the real sample from Riess et al (2022).	35
3.2	The parameter values fitted to the histograms for the real data.	38
3.3	Sampling configurations used on run_mcmc.py code. It were generated 10000 chains each one with 1000 walkers and, for the total number of chains, the first 6000 chains were eliminated. The convergence was monitored using emcee's recommended method to estimate the autocorrelation time τ and the burn-in time was set to be 5τ to allow chains to fully converge [2].	39
3.4	Fitted values obtained through χ^2 analysis, considering the real sample from Riess et al (2022) and Pantheon+.	41
4.1	Least squares solutions for H_0 and M_B using synthetic data affected by systematic shifts on the apparent magnitudes of second rung SNeIa with different magnitudes Δ_{sys} , in units of $\sigma_{\text{stat}} = 0.098$ mag.	46
4.2	Least squares solutions for H_0 and M_B using synthetic data affected by systematic shifts on data of third rung SNeIa with different magnitudes Δ_{sys} , in units of $\sigma_{\text{stat}} = 0.135$ mag.	47
4.3	Least squares solutions for H_0 and M_B using synthetic data affected by systematic shifts on data of the second and third rung SNeIa with different magnitudes Δ_{sys} , in units of $\sigma_{\text{stat}} = 0.098$ mag and $\sigma_{\text{stat}} = 0.135$ mag, respectively.	48
4.4	Least squares solutions for H_0 and M_B using synthetic data affected by systematic shifts on data of the second and third rung SNeIa with different magnitudes Δ_{sys} , in units of $\sigma_{\text{stat}} = 0.15$ mag.	49
4.5	Least squares solutions for H_0 , M_H^W , b_W and Z_W using the metallicity data affected by systematic shifts with different magnitudes Δ_{sys} , in units of $\sigma_{\text{stat}} = 0.05$ dex.	50
4.6	Fitted values obtained through χ^2 analysis for a consistent and an inconsistent analysis with the covariance matrix.	52

5.1	Fitted values obtained through χ^2 analysis considering the real sample and different models of color correction.	64
5.2	Least squares solutions considering the synthetic sample and different models of color correction.	69
6.1	Mean values and 1σ uncertainties for the cosmological and cosmographic parameters of each model considered in this work.	86
6.2	Mean values and 1σ uncertainties for the free parameters \bar{q}_0 and \bar{j}_0 for each Padé approximation considered in this work and the corresponding cosmographic values.	87
B.1	Least squares solutions for all fitted parameters using synthetic data affected by systematic shifts on the apparent magnitudes of second rung SNeIa with different magnitudes Δ_{sys} , in units of $\sigma_{\text{stat}} = 0.098$ mag.	96
B.2	Least squares solutions for all fitted parameters using synthetic data affected by systematic shifts on the apparent magnitudes of third rung SNeIa with different magnitudes Δ_{sys} , in units of $\sigma_{\text{stat}} = 0.135$ mag.	96
B.3	Least squares solutions for all fitted parameters using synthetic data affected by systematic shifts on the apparent magnitudes of second and third rung SNeIa with different magnitudes Δ_{sys} , in units of $\sigma_{\text{stat}} = 0.098$ mag and $\sigma_{\text{stat}} = 0.135$ mag, respectively.	99
B.4	Least squares solutions for all fitted parameters using synthetic data affected by systematic shifts on the apparent magnitudes of second and third rung SNeIa with different magnitudes Δ_{sys} , in units of $\sigma_{\text{stat}} = 0.15$ mag.	99
B.5	Least squares solutions for all fitted parameters using metallicity data of cepheids affected by systematic shifts with different magnitudes Δ_{sys} , in units of $\sigma_{\text{stat}} = 0.05$ dex.	101

Acronyms

AU Astronomical Unit

BAO Baryonic Acoustic Oscillations

CC Cosmic Clocks

CMB Cosmic Microwave Background

HST Hubble Space Telescope

ISW Integrated Sachs-Wolfe

JWST James Webb Space Telescope

LMC Large Magellanic Cloud

MCMC Monte Carlo Markov Chains

MW Milk Way

P-L Period-Luminosity

SH0ES Supernovae and H0 for the Equation of State of dark energy

SN Supernova

SNe Supernovae

SNeIa Type Ia Supernovae

SNIa Type Ia Supernova

SW Sachs-Wolfe

Contents

Abstract	IV
Resumo	V
1 Introduction	1
2 Cosmic microwave background	5
2.1 Anisotropies	6
2.2 The CMB temperature power spectrum	10
2.3 Constraints on cosmological parameters	11
2.3.1 CMB and the Hubble parameter	14
3 Cosmic distance ladder	17
3.1 The magnitude scale	18
3.2 The rungs of the cosmic distance ladder	20
3.3 Combined fit of all ladder rungs	27
3.4 Cosmic distance ladder data from R22	31
3.4.1 Best fit solution for R22 data	35
3.5 Cosmic distance ladder data from R22/Pantheon+	39
3.5.1 Best fit solution for R22/Pantheon+ data	41
4 Response of the distance ladder to systematic errors	45
4.1 Full covariance matrix	45
4.2 The role of data correlations	52
5 Cosmic distance ladder with different models of color correction	59
5.1 Standard color correction model	61
5.2 Model with two color correction coefficients	65
5.3 Model with two color correction coefficients and a reference color	67
5.4 Crosschecks with synthetic data	68
6 The $f(z)$CDM approach	71
6.1 Extensions to the standard cosmological model	71
6.2 Cosmography	72
6.3 Padé series	74

6.4	The $f(z)$CDM approach: connecting the ΛCDM model with cosmography	82
6.5	Parameter constraints with the $f(z)$CDM approach	84
6.6	Overview	87
7	Conclusions	90
A	Data covariance matrix	92
B	Complete tables and plots	94
C	Cosmographic expressions	102
	Bibliography	105

1 | Introduction

A century ago, Edwin Hubble discovered a single variable star (a cepheid) in the Andromeda galaxy. From the distance measurement of this star and the period-luminosity relationship established by Henrietta Leavitt [3], Hubble was able to take some subsequent measurements of extragalactic distances. By studying the correlation between these distances and the radial velocities of the observed objects, obtained through spectral measurements [4], Hubble has observed that most galaxies are moving away from Earth [5]. The first person to propose that this distancing is due to the expansion of the Universe was Georges Lemaître, but this idea was only consolidated with the publication of a paper in 1931 [6], the result of collaboration between Hubble and astronomer Milton Humason.

The current rate of this expansion is known as the Hubble constant (H_0). The value of the constant is fundamental to cosmology, as it sets the fundamental length and time scale of cosmic expansion. Accurate knowledge of H_0 is necessary to quantitatively test various aspects of the cosmological theory, such as: the predicted age of the Universe, the cosmological constant, comparisons between the nucleosynthesis of the Big Bang and observations of the matter density, predictions of the mass density of dark matter and the comparison of theories of structure formation with the anisotropies of the Cosmic Microwave Background (CMB) [7]. And precisely because it is related to various cosmological phenomena, this parameter can be determined in several different ways and independently, such as through measurements of the anisotropies of the CMB [8, 9], the Baryonic Acoustic Oscillations (BAO) [10, 11, 12], Cosmic Clocks (CC) [13, 14, 15, 16, 17, 18, 19, 20], gravitational waves [21, 22] and also by measuring the distance and recessional velocity of celestial bodies [23, 24, 25, 26, 27, 28, 29, 30, 31].

Due to technological limitations, it took a while for accurate measurements of these properties to be obtained. It was only in the 1990s that the first satellite to measure the cosmic microwave background radiation was launched, COBE, which was able to observe the anisotropies of the CMB [32, 33, 34] for the first time in full-sky mode. In the same decade, the Hubble Space Telescope (HST) and the Hubble Space Telescope Key Project team emerged, intending to measure the expansion rate of the Universe with an accuracy of 10%. This team in 2001, using data from the HST and a calibration based on cepheids, obtained a value of $H_0 = 72 \pm 3$ (statistical) ± 7 (systematic) $\text{km s}^{-1} \text{Mpc}^{-1}$ [23]. In the same year, COBE's successor, WMAP, went into operation. Through its measurements and assuming the Λ CDM model, a value of $H_0 = (71.9 \pm 2.6) \text{ km s}^{-1} \text{Mpc}^{-1}$ [35] was obtained. Four years later, the Supernovae and H0 for the Equation of State of dark energy (SH0ES) program

appeared with a proposal to end the degeneracy between the cosmological parameters used to model the CMB data and the equation of state parameter w . The first estimate of this program used data from 6 Type Ia Supernovae (SNeIa) and an anchor, the NGC4258 galaxy, which produced a value of $H_0 = (74.2 \pm 3.6) \text{ km s}^{-1} \text{ Mpc}^{-1}$ (Riess et al. 2009, hereafter R09) [24], which was consistent with the WMAP estimate and also with that of the Hubble Space Telescope Key Project team. A decade later, the SH0ES team increased the SNeIa sample to 8 and also added two more anchors to the fit: the Large Magellanic Cloud (LMC) and the Milk Way (MW). These new data resulted in $H_0 = (73.8 \pm 2.4) \text{ km s}^{-1} \text{ Mpc}^{-1}$ (Riess et al. 2011, hereafter R11) [25]. The sample was recalibrated by the HST Key Project team with other cepheid data and produced $H_0 = (74.4 \pm 2.2) \text{ km s}^{-1} \text{ Mpc}^{-1}$ (Freedman et al. 2012, hereafter F12) [26].

The scientific team running the successor mission of WMAP, the Planck collaboration, released its first results in 2013, which included a Hubble constant of $(67.2 \pm 1.2) \text{ km s}^{-1} \text{ Mpc}^{-1}$ [36], a reduction of 2σ with respect to WMAP and a difference of 3σ with respect to R11 and F12. This difference between H_0 values obtained via CMB and SNeIa indicated the possible existence of a cosmological tension. The third estimate done by the SH0ES team, with 19 supernovae and refined distance measurements from NGC4258 and LMC, produced a value of $H_0 = (73.2 \pm 1.7) \text{ km s}^{-1} \text{ Mpc}^{-1}$ (Riess et al. 2016, hereafter R16) [27], 3.4σ higher than the refined Planck value of $(66.9 \pm 0.6) \text{ km s}^{-1} \text{ Mpc}^{-1}$ (Planck Collaboration et al. 2016) [37]. The Planck data was reanalyzed in 2018, producing $H_0 = (67.37 \pm 0.54) \text{ km s}^{-1} \text{ Mpc}^{-1}$. In 2021, with more accurate cepheid parallax data obtained from Gaia, SH0ES determined $H_0 = (73.2 \pm 1.3) \text{ km s}^{-1} \text{ Mpc}^{-1}$ (Riess et al. 2021, hereafter R21) [30], raising the difference with Planck to 4.2σ . One year later, with an additional anchor M31 and a new sample of 42 SNeIa, the same group determined $H_0 = (73.04 \pm 1.01) \text{ km s}^{-1} \text{ Mpc}^{-1}$ (Riess et al. 2022, hereafter R22) [31], reaching a difference of 5σ with respect to the Planck estimate, confirming the Hubble tension.

It can be seen that, at present, measurements based on cepheids-SNeIa continue to generate values close to $73 \text{ km s}^{-1} \text{ Mpc}^{-1}$, while measurements using the tip of the red giant branch (TRGB) [29, 38] produce slightly lower values, closer to $70 \text{ km s}^{-1} \text{ Mpc}^{-1}$. Recent estimates of H_0 from CMB measurements are the most accurate and also the lowest, at around $68 \text{ km s}^{-1} \text{ Mpc}^{-1}$. This inconsistency between the local value of the Hubble constant and the cosmologically modeled value has put the current model of the Universe to test, with the argument that perhaps the cosmological model needs some new physics. Although the acoustic oscillations of the photon-baryon fluid in the early Universe are well understood, it is important to bear in mind that the astrophysics of stellar distance indicators is less predictable and that absolute calibrations of the local distance scale at a comparable level

(of 1%), with the identification and elimination of systematic effects, are much more delicate [39]. Given the current challenges of obtaining accurate measurements of local distances, it may be premature to affirm or refute the need for physics beyond the standard model [40]. These remaining challenges highlight the need for a definitive measure of H_0 locally, which in turn requires a full assessment of its total uncertainties (statistical and systematic) [41].

However, there is of course also work investigating whether models that address new physics are capable of resolving the tension in the Hubble constant. As the nature of dark energy is still unknown, despite the fact that it constitutes 70% of the current energy density of the Universe [8], and within the standard model is responsible for its late time accelerated expansion [30], there is space for various theories to emerge. For example, scalar fields [42, 43] or modified gravity [44, 45, 46, 47] can be invoked as mechanisms to originate the accelerated expansion. New tools and techniques, such as exploring the effects of dark energy without explicitly assuming a specific cosmological model, are also gaining power in this context [48, 49, 50, 51].

Therefore, in this work the problem of the tension in the Hubble constant is investigated from both points of view: data analysis and theoretical modeling. The first line of research is divided into three types of analyses involving hypothetical systematic errors in the cosmic distance ladder method:

- systematic errors associated to the cosmic distance ladder data used in the fit, including ancillary data;
- systematic effects associated to the construction of the data covariance matrix;
- bias introduced via theoretical modeling of the data.

On the other hand, following the second line of research, a hybrid approach combining the Λ CDM model and cosmography, called $f(z)$ CDM, is proposed to describe the background evolution of the Universe. This is done in order to verify if an alternative model would be able to resolve or alleviate the Hubble tension .

In Chapter 2 a brief review of the cosmic microwave background radiation is given, covering the theory of its anisotropies, how some characteristics of the power spectrum of these anisotropies are connected to aspects of the Universe, how the cosmological parameters can interfere with these characteristics and also how it is possible to constrain the cosmological parameters, in particular H_0 , based on information from the power spectrum.

Next, in Chapter 3, an introduction to the magnitude scale in astronomy is given as this is a basic concept to work with the cosmic distance ladder method. Then, the rungs of the ladder are presented and, since the study of the cosmic distance ladder carried out in this

work is based on the work of R22, the data as well as the fit carried out in this reference are described in detail. A reproduction of R22 fit is done, a Monte Carlo Markov Chains (MCMC) analysis is presented and, after, and a new data sample based on R22 and Pantheon+ is built. Finally, another fit considering R22/Pantheon+ data sample is performed.

In Chapter 4, the way in which the synthetic data samples were generated is explained. Then we analyze how the systematic errors added to the synthetic data interfere with the fitted values of the cosmic distance ladder parameters, especially the Hubble constant, through a least-squares method. In addition, two complementary analyses are also presented, one using Monte Carlo Markov Chains and other with an inconsistency between the matrices used on data generation and fit.

In Chapter 5, the mixed data sample is considered, which combines data from SHOES and the Pantheon+ catalog, to obtain data of the apparent magnitude of supernovae without color and stretch corrections. With the real data sample, fits are done considering three models of color correction: standard model, a model with two color correction coefficients and a model with this two coefficients and a color reference. Then, a new synthetic data sample is generated based on R22/Pantheon+ data and considering the last model of color correction. Fits are performed considering this synthetic data and the three models of correction, in order to verify the influence of the errors associated with the modeling of the data and the consideration of different models on the values of the theoretical parameters.

In Chapter 6, theoretical models and techniques that address new physics in the description of the dark component of the Universe energy density are discussed. An approach called $f(z)$ CDM that combines the standard cosmological model and cosmography is proposed as the background evolution of the Universe, in which Padé series are considered as a function $f(z)$ that describes the dark energy component, whereas the other ones follow the standard model. Next, the constraints on the cosmological parameters were performed using COSMOMC and including CMB, BAO, CC and SNeIa data. This chapter is the result of a six months internship at Scuola Superiore Meridionale - Università degli Studi di Napoli, in Italy, which provides a complementary analysis to the present work.

Finally, conclusions are presented on Chapter 7.

2 | Cosmic microwave background

According to the standard cosmological model (Λ CDM), the Universe started at a very dense and hot tiny region that began to expand and cool itself with the Big Bang. The temperature was extremely high in the Universe, therefore atoms could not form. However, about 370,000 years after the Big Bang, the Universe cooled down enough to a temperature at which baryons¹ and photons could decouple and atoms could form. After this, the light began to propagate freely and the relic of this “first light” is called the Cosmic Microwave Background.

The CMB was discovered in 1965 by Arno Penzias and Robert Woodrow Wilson, two American radio astronomers. They registered a signal in their radio telescope that could not be attributed to any precise source in the sky. This signal came from everywhere with the same intensity, then they concluded that it had to come from outside of our Galaxy. Since the baryon-photon decoupling, the Universe has expanded, becoming at the same time cooler. The CMB has been affected by the Universe expansion, its frequency monotonically decreasing with time, and nowadays its maximum spectral density falls in the microwave range. This radiation is the farthest and oldest one that any telescope can detect and, due to this fact, is currently one of the most promising ways to understand the birth and evolution of the Universe.

In their landmark 1965 paper, Penzias and Wilson reported a 3.5 K signal from the sky at 4 GHz that was “isotropic, unpolarized and free of seasonal variations”¹ [52] within the limits of their observations. In a paper published in the same year, Dicke et al. (1965) proposed the explanation that the isotropic signal in the sky seen by Penzias and Wilson indicated the occurrence of a hot Big Bang [53], as suggested in the paper by Alpher et al. (1948), which predicted the existence of a blackbody spectrum of CMB photons with a current temperature of a few Kelvins [54]. This prediction was based on considering the conditions necessary for a successful nucleosynthesis in an expanding Universe, that is, to create an appreciable amount of primordial helium from the free neutrons that are at the same time decaying as the Universe expands.

With the discovery of the CMB, there was an immediate interest in trying to characterize it and one of the questions at the time was to what extent the radiation was isotropic and its spectrum resembled that of a perfect blackbody. Physical processes for generating

¹In cosmology, this term refers both to the usual baryons of particle physics (with three valence quarks) and to electrons.

anisotropies, such as gravitational redshift, were proposed in 1967 [55]. An exhaustive treatment of the evolution of density perturbations was given in 1970 [56], in which the acoustic oscillations of the photon-baryon fluid were discussed. In addition, between 1960 and 1980, several studies were carried out on the thermal history and formation of the structure of the Universe and its consequences on the CMB [57, 58, 59, 60]. In 1984, for the first time, the anisotropies of the CMB in a universe dominated by cold non-baryonic dark matter were estimated [61, 62]. And in 1989 and 1992, the evolution of the CMB density and its temperature fluctuations were calculated, as well as predictions for the observations, respectively [63, 64].

Studies of the cosmic background radiation and its anisotropies were restricted to theory for many years. The biggest obstacle to making observations was the lack of suitable instrumentation. Due to this, the first clear and full-sky detection of the CMB anisotropies had to wait until the early 1990s to be made. The COBE satellite was proposed in 1974 and was one of the most important steps in the investigation of the CMB, although it was necessary to wait until 1989 for its launch. The COBE measurements in 1992 allowed a rigorous constraint of the CMB spectral distribution [32, 34, 65], as well as a precise measurement of the blackbody temperature (2.7260 ± 0.0013) K [32]. However, the greatest achievement made by COBE was the observation of the CMB temperature anisotropies in the sky [33].

From this work, it became clear that more precise measurements of anisotropies with higher sensitivity and better angular resolution than COBE (7°) would lead to a new era in cosmology. Consequently, two other missions emerged: WMAP and Planck. The WMAP satellite, capable of measuring angular scales of $18'$, was launched in 2001 and the first results were announced in 2003 [66, 67]. Among the main results are: proof of the existence of the Sachs-Wolfe effect, detection of acoustic peaks in the CMB anisotropy spectrum and verification that the CMB radiation is polarized. The Planck satellite was launched in 2009. With an angular resolution of $5'$, Planck successfully obtained a map of the CMB over the entire sky and its first results were presented in 2013 [36]. Figure 2.1 shows the difference between the angular resolutions of the CMB anisotropy maps obtained from observations made by each of these satellites.

2.1 Anisotropies

According to the field equations of Einstein's theory of General Relativity, CMB anisotropies are tightly linked to gravitational perturbations. In order to linearize Einstein's equations, we will work in a spatially flat Universe whose metric is the Friedmann-Lemaître-Robertson-

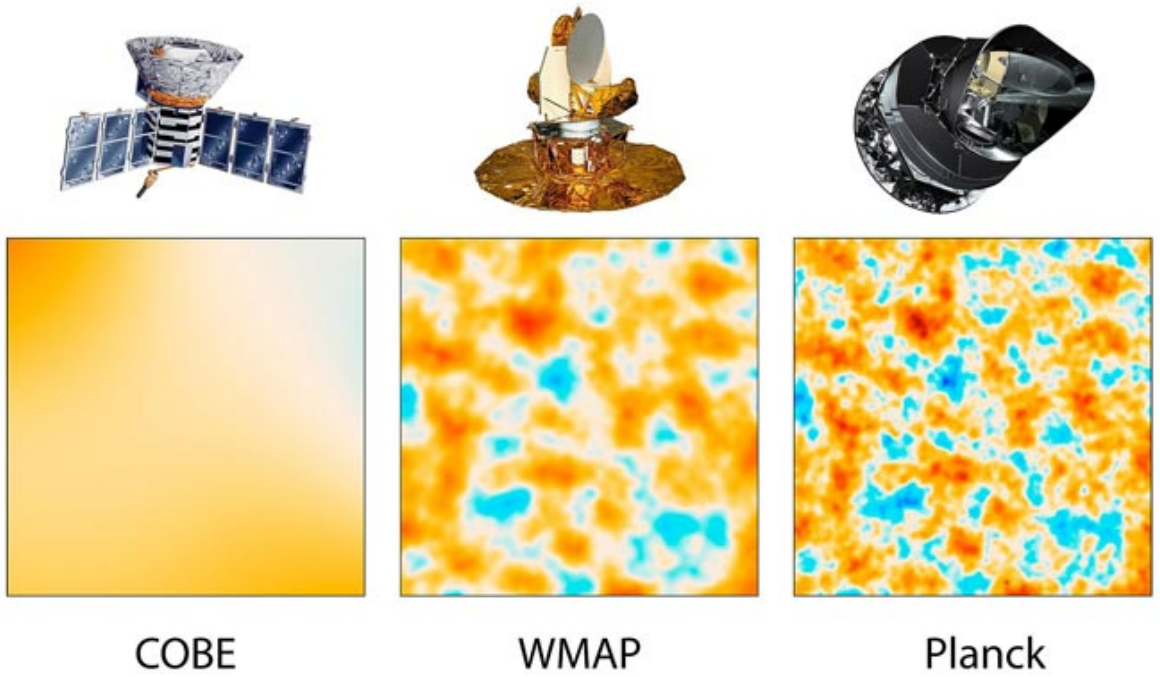


Figure 2.1: Differences between the angular resolution of each satellite: COBE (7°), WMAP (0.3° or $18'$) and Planck ($5'$). The squares represent 10° degrees squares observed of the CMB anisotropies. Extracted from: NASA/JPL-Caltech/ESA.

Walker one [68, 69]. A general line element with small perturbations ($\delta g_{\alpha\beta}$) is written as follows:

$$ds^2 = (g_{\alpha\beta} + \delta g_{\alpha\beta}) dx^\alpha dx^\beta, \quad (2.1)$$

in which ds^2 is an invariant interval, $g_{\alpha\beta}$ is the metric tensor and $dx^{\alpha,\beta}$ are coordinates in the space-time. Using conformal time (ξ), the background metric in a spatially flat Universe is given by:

$$g_{\alpha\beta} dx^\alpha dx^\beta = a^2(\xi)(d\xi^2 - \delta_{ij} dx^i dx^j), \quad (2.2)$$

where a is the scale factor. The perturbations of the metric $\delta g_{\alpha\beta}$ are classified into three types: scalar, vector and tensor. This classification is based on the homogeneity and isotropy properties of the background. The $\delta g_{00} = 2a^2\phi$ component behaves as a scalar, with ϕ being a scalar field. The spatial components $\delta g_{0i} = a^2(B + S_i)$ behave like vectors, with B being a scalar and S_i a vector. And the components $\delta g_{ij} = a^2(2\psi\delta_{ij} + 2E + F_i + h_{ij})$ behave like tensors, where ψ and E are scalars, F_i a vector and h_{ij} a tensor [68].

Scalar perturbations are induced by energy density inhomogeneities and exhibit gravita-

tional instabilities that lead to the formation of structures in the Universe. Vector perturbations associated with vorticity² are responsible for rotations of the cosmic fluid and tensor perturbations in the metric for gravitational waves. The so called decomposition theorem [68] guarantees that these three types of perturbations are uncoupled. For the sake of brevity, we will treat explicitly only scalar ones. Therefore, for scalar perturbations, the invariant interval takes the form:

$$ds^2 = a^2\{(1 + 2\phi)d\xi^2 + 2B_{,i}dx^i d\xi - [(1 - 2\psi)\delta_{ij} - 2E_{,ij}]dx^i dx^j\}, \quad (2.3)$$

in which $B_{,i}$ denotes a covariant derivative of B ($\partial_i B$). By choosing a Newtonian gauge transformation [69, 68], it is possible to write the above equation as follows:

$$ds^2 = a^2[(1 + 2\Phi)d\xi^2 - (1 - 2\Psi)\delta_{ij}dx^i dx^j], \quad (2.4)$$

where Φ and Ψ are the Newtonian potential and the spatial perturbation of the metric, respectively. To derive the perturbation equations, it is necessary to linearize the Einstein equations:

$$G_\beta^\alpha = 8\pi GT_\beta^\alpha, \quad (2.5)$$

in which T_β^α is the energy-momentum tensor. The Einstein tensor can be written as $G_\beta^\alpha = G_\beta^{\alpha,0} + \delta G_\beta^\alpha$, where δG_β^α are perturbations. Thus, the linearized equations for the perturbations are given by:

$$\delta G_\beta^\alpha = 8\pi G\delta T_\beta^\alpha. \quad (2.6)$$

The left-hand side of the above equation is gauge invariant and depends only on the perturbations of the metric [68]. Therefore, it can be expressed entirely in terms of Φ and Ψ . Writing the components of the energy-momentum tensor separately we have [69]:

$$\delta T_0^0 = -\delta\rho, \quad \delta T_i^0 = (\rho + P)v_i, \quad \delta T_j^i = -\delta P\delta_j^i - \Pi_j^i, \quad (2.7)$$

in which $\delta\rho$ and δP are fluctuations in energy density and pressure, respectively, v_i is the bulk velocity of the fluid and Π_j^i is the stress-anisotropy tensor. Using the perturbed metric, see equation (2.3), and the perturbed energy-momentum tensor given by equation (2.7), the

²The specific vector perturbations associated with vorticity are often described by a vector field representing the velocity perturbations in the cosmic fluid. In Fourier space, the vorticity vector (angular velocity) can be related to the velocity vector.

evolution equations for Ψ and Φ are obtained:

$$\nabla^2\Psi - 3H(\Psi' + H\Phi) = -4\pi Ga^2\delta\rho, \quad (2.8)$$

$$\partial_i(\Psi' + H\Phi) = 4\pi Ga^2\delta(\rho + P)v_i, \quad (2.9)$$

$$[\Psi'' + H(2\Psi + \Phi)' + (2H' + H^2)\Phi + \frac{1}{2}\nabla^2(\Phi - \Psi)]\delta_j^i = 4\pi Ga^2\delta P\delta_j^i, \quad (2.10)$$

$$-\frac{1}{2}\partial^i\partial_j(\Phi - \Psi) = 4\pi Ga^2\Pi_j^i. \quad (2.11)$$

These are the equations that describe the dynamics of the primordial Universe [69, 68]. However, for a complete description of the CMB anisotropies, it is also necessary to understand how its probability density distribution evolves. In the context of perturbation theory, we can consider the temperature of the CMB to be [69, 70]:

$$\Theta(\mathbf{x}, \mathbf{p}, \xi) = \Theta_0 + \Theta(\mathbf{x}, |\mathbf{p}|, \xi), \quad (2.12)$$

in which Θ_0 is the blackbody average temperature and $\Theta(\mathbf{x}, |\mathbf{p}|, \xi)$ are the anisotropies of the radiation distribution. At this point, it is important to remember that before and right after the recombination, the CMB photons interacted with free electrons in space. Until the complete decoupling of the photon-baryon fluid, this interaction influenced the photon distribution, inducing a certain degree of polarization in the CMB. This process occurred by means of Thomson scattering, the amplitude of which is given by:

$$|\mathcal{M}|^2 = 6\pi\sigma_T m_e^2 [1 + \cos^2(\hat{\mathbf{p}} \cdot \hat{\mathbf{p}}')], \quad (2.13)$$

where σ_T is the cross section for Thomson scattering, $\hat{\mathbf{p}}$ the incident momentum direction of the photon and $\hat{\mathbf{p}}'$ its momentum direction after the collision with the electron. In Fourier space, the following evolution equation can be found for the temperature of the CMB photons [69]:

$$\dot{\Theta} + ik\mu\Theta = -\dot{\Phi} - ik\mu\Psi - \Gamma[\Theta - \Theta_0 - i\mu v_e], \quad (2.14)$$

in which μ is the cosine of the angle between $\hat{\mathbf{p}}$ and $\hat{\mathbf{p}}'$, v_e is the velocity of the electrons in the comoving frame of reference, k is the wavenumber and Γ is the photon scattering rate by electrons. Thus, Θ can be completely determined in terms of Φ , Ψ and v_e , however, baryons evolve in the perturbed background, and the gravitational potential is a function that depends on the matter density contrast generated by gravitational potential. In other words, we have a coupled set of differential equations to solve. Therefore, a few more equations are needed to describe the anisotropies, derived from the Boltzmann equations for other components that

evolve with the CMB:

$$\dot{\Theta} + ik\mu\Theta = -\dot{\Phi} - ik\mu\Psi - \dot{\tau}[\Theta_0 - \Theta + \mu v_b + \frac{1}{2}\mathcal{P}_2(\mu)(\Theta_2 + \Theta_{P_0} + \Theta_{P_2})], \quad (2.15)$$

$$\dot{\delta} + ikv = -3\dot{\Phi}, \quad (2.16)$$

$$\dot{v} + \frac{\dot{a}}{a}v = -ik\Psi, \quad (2.17)$$

$$\dot{\delta}_b + ikv_b = -3\dot{\Phi}, \quad (2.18)$$

$$\dot{v}_b + \frac{\dot{a}}{a}v_b = -ik\Psi + \frac{\dot{\tau}}{R}[v_b + 3i\Theta_1], \quad (2.19)$$

$$\dot{\mathcal{N}} + ik\mu\mathcal{N} = -\dot{\Phi} - ik\mu\Psi, \quad (2.20)$$

$$\dot{\Theta}_P + ik\mu\Theta_P = -\dot{\tau}[-\Theta_P + \frac{1}{2}(1 - \mathcal{P}_2(\mu))(\Theta_2 + \Theta_{P_0} + \Theta_{P_2})], \quad (2.21)$$

in which δ and δ_b are contrast densities for dark matter and baryons, Θ_1 is the CMB dipole, v and v_b ($v_b = v_e$) are the bulk velocities of the fluids present in the energy-momentum tensor for dark matter and baryons, \mathcal{N} is the perturbation in the neutrino energy density, τ is the optical depth due to Thomson scattering and Θ_P is the polarization field [69, 70]. Equations (2.15)-(2.21) are a system of coupled differential equations responsible for describing the dynamics of perturbations in the density of matter, CMB anisotropies, gravitational potentials and neutrinos. It is possible to solve this system of equations using open source codes like CAMB [71], for example, by providing as input the values of the cosmological parameters.

2.2 The CMB temperature power spectrum

One of the main observables of the CMB is its intensity as a function of frequency and direction on the sky $\hat{\mathbf{n}}$. Since the CMB spectrum is essentially a blackbody with a nearly constant temperature T across the sky, it is possible to describe this observable in terms of its temperature fluctuation:

$$\Theta(\hat{\mathbf{n}}) = \Delta T/T. \quad (2.22)$$

These fluctuations can be decomposed in spherical harmonics. Therefore, the multipole moments of the temperature field are given by [72]:

$$\Theta_{lm} = \int d\hat{\mathbf{n}} Y_{lm}^* \Theta(\hat{\mathbf{n}}), \quad (2.23)$$

which, for a Gaussian field, from the statistical point of view, are fully characterized by their

temperature power spectrum C_l^{TT} :

$$\langle \Theta_{lm}^* \Theta_{l'm'} \rangle = \delta_{ll'} \delta_{mm'} C_l^{TT}. \quad (2.24)$$

Equation (2.24) allows us to write also the cross-correlation function of the temperature fluctuations:

$$\langle \Theta(\hat{\mathbf{n}}) \Theta(\hat{\mathbf{n}}') \rangle = \frac{1}{4\pi} \sum_l (2l+1) C_l^{TT} P_l(\mu), \quad (2.25)$$

in which $P_l(\mu)$ are the Legendre polynomials and μ the cosine of the angle between $\hat{\mathbf{n}}$ and $\hat{\mathbf{n}}'$. If recombination can be considered as instantaneous, temperature fluctuations in the CMB are dominated by three main contributions:

$$\frac{\Delta T}{T} \approx \Psi + \Theta_0 + 2 \int_0^n d\eta (\dot{\Psi} + \dot{\Phi}) - \hat{\mathbf{n}} \cdot (\mathbf{v}_0 - \mathbf{v}_e), \quad (2.26)$$

which are the Sachs-Wolfe (SW) effect due to the additional redshift that photons experience when climbing gravitational potentials; the Integrated Sachs-Wolfe (ISW) effect, which considers all the contributions from time-varying gravitational potential along the line of sight; and the Doppler effect originated from the baryon-photon fluid [69].

In addition to scalar perturbations characterized by Ψ and Φ , the tensor perturbations leave characteristic imprints in the CMB anisotropies, that are used as independent data in addition to the temperature anisotropies. These imprints appear in the form of CMB polarizations. The tensor perturbations are not the only phenomena that cause the polarizations of the CMB, there are also Thomson scattering and the contamination of one of the polarization modes by gravitational weak lensing of the CMB, but this content is outside the scope of this work and it will not be studied in depth.

2.3 Constraints on cosmological parameters

As seen in the previous sections, in order to infer cosmological parameters from the measurements of the cosmic background radiation anisotropies, one needs to assume an underlying cosmological model. In the last decades, the concordance model has emerged, also known as Λ CDM, showing considerable agreement with different types of data (distribution of galaxies on a large scale, anisotropies of the cosmic background radiation, measurements of Supernova (SN), etc). This model is characterized by a series of parameters related to the

2 | Cosmic Microwave Background

dynamics of the Universe, which are presented in Table 2.1 with $\Omega_k = 0$ ³. In this table, there are two types of parameters: (a) those fitted directly to the measurements of the intensity (temperature) and polarization of the CMB, called base parameters, and (b) those inferred from the base ones. The values of the cosmological parameters in Table 2.1 were obtained by a combined fit of intensity, polarization and lensing using data from the Planck satellite [8] measurements.

Parameter	Name	Central value \pm 68% limits
$\omega_b \equiv \Omega_b h^2$	Baryon energy density	0.02237 ± 0.00015
$\omega_c \equiv \Omega_c h^2$	Cold dark matter energy density	0.1200 ± 0.0012
$100\Theta_{MC}$	Acoustic horizon scale	1.04092 ± 0.00031
τ	Optical depth due to reionization	0.0544 ± 0.0073
$\ln(10^{10} A_s)$	Primordial scalar amplitude	3.044 ± 0.014
n_s	Spectral scalar index	0.9649 ± 0.0042
H_0	Hubble constant	$67.36 \pm 0.54 \text{ km s}^{-1} \text{ Mpc}^{-1}$
Ω_m	Matter energy density fraction	0.3153 ± 0.0073
σ_8	Galaxy clustering at $8 h^{-1} \text{ Mpc}$	0.8111 ± 0.0060

Table 2.1: Summary of the base- Λ CDM+ Ω_k parameters and their values obtained from the best fit performed by the Planck collaboration using the so called TT+TE+EE+lowE+lensing combined likelihood [8], an analysis that combines measurements of intensity (TT), polarization of electric-type modes (EE), intensity-polarization cross-correlation (TE) and gravitational lensing. Curvature energy density Ω_k is added, and assumed zero by construction. Derived parameters are in the lower half of the table.

Figure 2.2 shows the dependence of the temperature power spectrum on the parameters of the base Λ CDM model. The spectra in this figure were generated using CAMB [71] and the values of the fixed parameters were considered to be those shown in Table 2.1. At the top of the figure, we have varied the optical depth (τ) and the baryon energy density (ω_b). It can be seen that the optical depth decreases the power of the spectrum, because the greater the optical depth the more intense the scattering between CMB photons and electrons from the reionization process in the Universe as the first stars began to form at the end of the dark age. The baryon energy density changes the speed of sound of the photon-baryon fluid and consequently, the size of the sound horizon, which ends up causing the acoustic peaks to shift.

At the center of Figure 2.2 one can find the power spectra as we vary the acoustic horizon scale (Θ_{MC}) and the cold dark matter energy density (ω_c). It can be seen that the acoustic horizon scale shifts the spectra, due to the relationship between this parameter and the

³According to [8], the joint constraint with BAO measurements on spatial curvature is consistent with a flat universe, $\Omega_k = 0.001 \pm 0.002$.

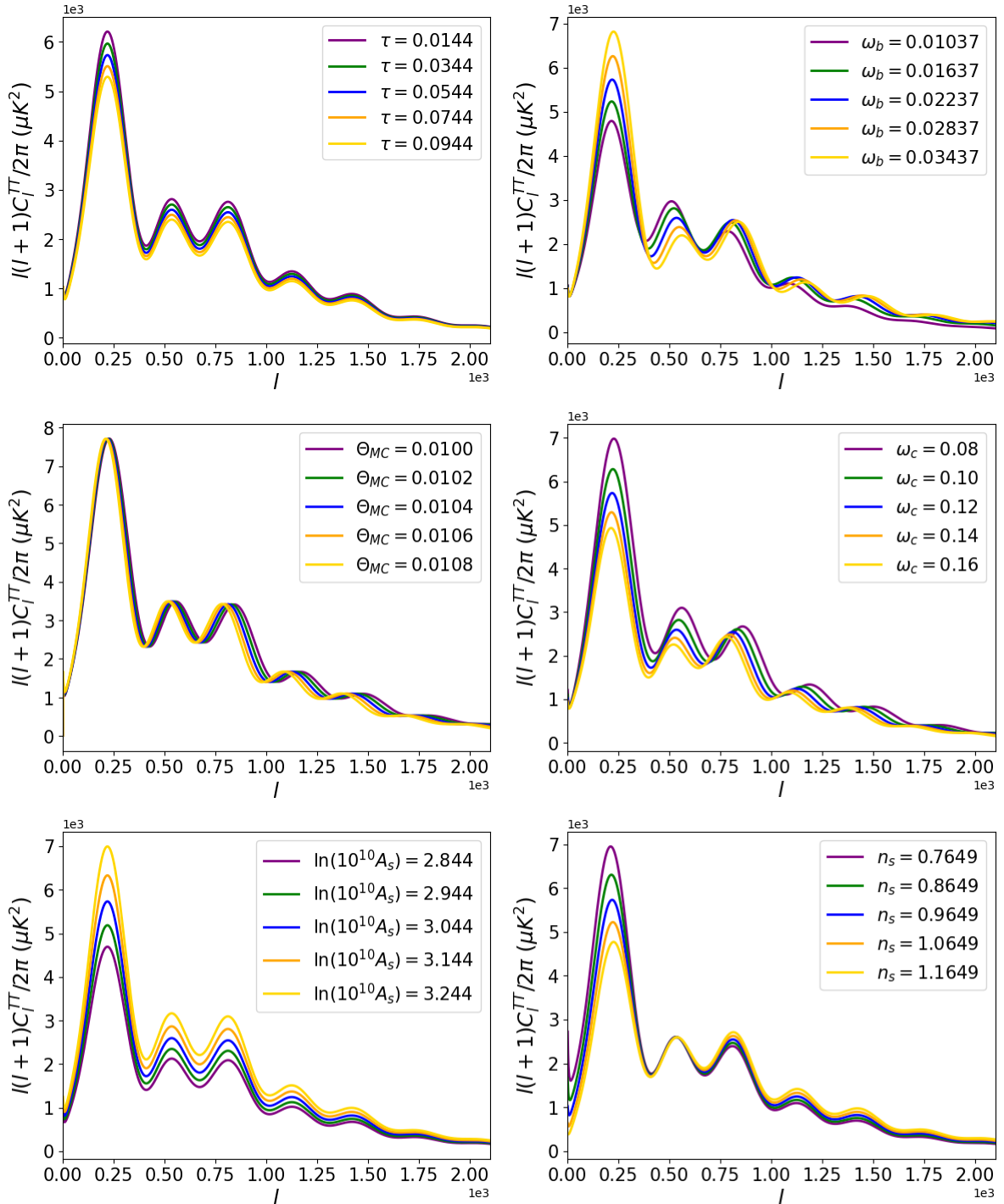


Figure 2.2: Power spectra of the CMB temperature anisotropies varying the optical depth due to reionization (τ), the baryonic energy density (ω_b), the acoustic horizon scale (Θ_{MC}), the cold dark matter energy density (ω_c), the primordial scalar amplitude $[\ln(10^{10}A_s)]$ and the scalar spectral index (n_s), respectively.

acoustic oscillations around the epoch of recombination. The cold dark matter energy density alters the amplitudes of the peaks, because as this quantity varies, the moment at which the matter matches the radiation in terms of energy density can be made closer or farther from the present day, enhancing or decreasing the ISW contribution, respectively.

At the bottom of Figure 2.2 are the spectra as we vary the primordial scalar amplitude $[\ln(10^{10}A_s)]$ and the scalar spectral index (n_s). It can be seen that the primordial scalar amplitude alters the normalization of the initial spectrum and that the scalar spectral index alters its slope, since it dictates how the primordial fluctuations were generated during inflation as a function of the scale k . These two parameters differ from the others because they are related to physics that was in operation during the inflationary period, i.e. long before recombination.

2.3.1 CMB and the Hubble parameter

However, not all parameters that alter the behavior of the power spectra also affect the behavior of the Hubble constant. All the base parameters from Table 2.1 were modified in order to analyze the interference of this variation on H_0 and only three of these parameters cause significant changes in the Hubble constant: ω_b , ω_c and Θ_{MC} . In order to understand this effect, we start by writing the angular scale of the sound horizon at recombination as [73]:

$$\Theta_{MC} = \frac{r_s(z_s)}{d_s(z_s)} \tag{2.27}$$

in which r_s is the size of the sound horizon, that is, the distance sound waves could have traveled during the time elapsed between Big Bang and recombination, d_s is the distance to the surface of last scattering and z_s is the redshift of this surface. The sound horizon can be expressed as an integral over redshift [73]:

$$r_s(z_s) = \int_{z_s}^{\infty} \frac{c_s(z)}{H(z)} dz, \tag{2.28}$$

in which c_s is the redshift-dependent sound speed, given by:

$$c_s(z) = \frac{1}{\sqrt{3 \left[1 + \frac{3\Omega_b(1+z)^3}{4\Omega_r(1+z)^4} \right]}}, \tag{2.29}$$

where Ω_b and Ω_r are baryon and radiation energy density, respectively. $H(z)$ is the Hubble

parameter, which in a flat Universe ($\Omega_k = 0$) can be expressed as [74]:

$$H(z) = H_0 \sqrt{\Omega_m(1+z)^3 + \Omega_r(1+z)^4 + \Omega_\Lambda}, \quad (2.30)$$

in which Ω_m and Ω_Λ are matter and dark energy components of the Universe energy density, respectively. The comoving distance is given by:

$$d(z) = \int_0^z \frac{c}{H(z)} dz, \quad (2.31)$$

in which c is the speed of light. Therefore, the comoving distance to the surface of last scattering can be written like [73]:

$$d_s(z_s) = \int_0^{z_s} \frac{c}{H(z)} dz. \quad (2.32)$$

Replacing equations (2.28), (2.29) and (2.32) into equation (2.27), we have:

$$\Theta_{MC} = \frac{\int_{z_s}^{\infty} \left\{ h(z) \sqrt{3 \left[1 + \frac{3\omega_b(1+z)^3}{4\omega_r(1+z)^4} \right]} \right\}^{-1} dz}{\int_0^{z_s} \frac{c}{h(z)} dz}, \quad (2.33)$$

where $\omega_b \equiv \Omega_b h^2$, $\omega_r \equiv \Omega_r h^2$, $h(z) = H(z)/100 \text{ km s}^{-1} \text{ Mpc}^{-1}$ and we can also define $h = H_0/100 \text{ km s}^{-1} \text{ Mpc}^{-1}$. In this way:

$$h(z) = \sqrt{\omega_m(1+z)^3 + \omega_r(1+z)^4 + \omega_\Lambda} \quad (2.34)$$

in which $\omega_m \equiv \Omega_m h^2$ and $\omega_\Lambda \equiv \Omega_\Lambda h^2$. Recalling that we are dealing with a flat Universe, $\Omega_m + \Omega_r + \Omega_\Lambda = 1$, or:

$$\omega_m + \omega_r + \omega_\Lambda = h^2. \quad (2.35)$$

From the previous equations, it becomes clear why measurements of the CMB anisotropies power spectrum lead to a constraint on h if one assumes a spatially flat Universe in a Λ CDM cosmology. In the last equations, Ω_r is fixed a priori as we know the CMB temperature today and ω_Λ satisfies the constraint equation [2.35]. On the other hand, as we learned from the plots on Figure [2.2], ω_b and ω_c , (or equivalently ω_m), and Θ_{MC} are strongly constrained by the positions and relative heights of the acoustic peaks. Therefore, a fit of the Λ CDM model to the data produces an immediate constraint on h . Another way to say the same thing is

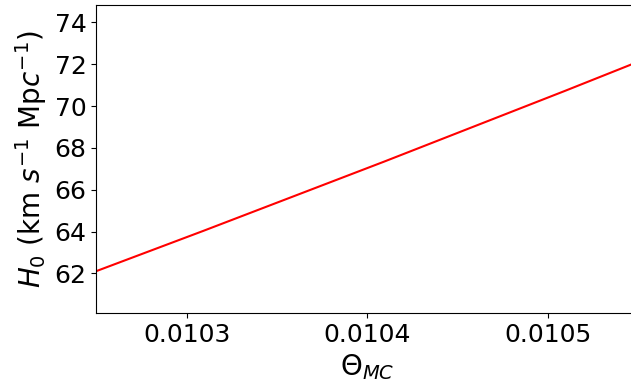


Figure 2.3: H_0 as a function of Θ_{MC} as calculated by CAMB [71], where the other five base parameters of the cosmological model were kept fixed at the values given in Table 2.1.

that in a spatially-flat Λ CDM cosmology, Θ_{MC} , ω_b , ω_c and h are not all independent, one of them can always be written in terms of the other three. The most widespread convention in the literature has been to adopt h as the dependent variable. Figure 2.3, for example, shows the dependence of H_0 with Θ_{MC} , for fixed ω_b and ω_c , as calculated by CAMB.

3 | Cosmic distance ladder

The distances in the Universe are so vast that there is not a single simple method of measuring them. For distances within the Solar System, it is possible to measure them directly, using radar, for example, or some simple trigonometric methods [75]. However, radar becomes inefficient when the light takes minutes or hours to return to the detector and, knowing that the nearest star to the Solar System is four light-years away (1.32×10^{-6} Mpc) [76], radar is not the best method for measuring distances beyond the Solar System.

A more efficient method is trigonometric parallax, which allows to determine the distances of nearby stars by measuring how much they appear to move with respect to the background stars over the course of six months [77, 75]. This is the most direct way of measuring distances to stars, but it is only valid for those within a radius of about a thousand light-years (3.07×10^{-4} Mpc) [76]. Determining parallaxes requires very precise measurements of the stars' positions in the sky. The largest parallax measured from Earth, that of Alpha Centauri, is less than one arc-second, and it is the star closest to us (4.3 light years away). As the size of the parallax decreases as the star moves away, it eventually becomes smaller than it is possible to measure [77].

Therefore, when parallax can no longer be used, measurement methods are no longer based solely on observations, but also on an understanding of astrophysics. For example, open clusters (groups of stars formed at the same time, with the same age, but with different masses, temperatures and luminosities) can be used to make assumptions about the brightnesses and therefore distances of the objects belonging to the cluster [76]. The brightness characteristics of these objects are calibrated using clusters for which it is possible to measure parallaxes and then extended outwards to the region where it is no longer possible to detect changes in the apparent position of its stars along the year [77].

The process that uses information from a closer region to obtain distance measurements of objects in a more distant one is called the Cosmic Distance Ladder, which is based on a series of measurements of different types of objects and phenomena, each based on the previous rung of the ladder. By extending the ladder with different types of measurements, ever greater distances in the Universe can be measured. Several of these rungs depend critically on variable stars, and some of the following sections are brief discussions of these objects and how they can be used to determine distances.

3.1 The magnitude scale

In order to explain how to obtain the distance of objects in the sky, it is necessary to review the most relevant property involved in this process: brightness. The brightness of a star is usually measured in terms of the radiant flux (F). This is the total amount of electromagnetic energy in all wavelengths that passes through a unit area positioned perpendicular to the direction of light propagation per unit time. In a hypothetical static Universe, the flux depends on the luminosity (L) of the observed object (energy per second) and its distance (r) from the observer [78, 79]:

$$F = \frac{L}{4\pi r^2}, \quad (3.1)$$

since the total luminosity through a spherical shell with area $4\pi r^2$ is constant. Generalizing for a Universe in expansion, it is simplest to work in a comoving grid, with the source centered at the origin [72]. Then, the flux observed is:

$$F = \frac{L(\chi)}{4\pi\chi^2(a)}, \quad (3.2)$$

remembering that a is the scale factor and $L(\chi)$ is the luminosity through a spherical shell with radius $\chi(a)$. In a given time span, photons cover a greater distance on the comoving grid during early epochs compared to later times, as the corresponding physical distance is smaller in the early stages. Consequently, the quantity of photons traversing a shell within the fixed time frame is now less than it was at the point of emission, reduced by a factor of a . Likewise, due to the expansion, the energy of these photons is now lower compared to their emission state. Consequently, the energy per unit time passing through a comoving shell at a distance from the source is diminished by a factor a^2 in comparison to the luminosity at the source [69]. Therefore, the flux observed will be:

$$F = \frac{La^2}{4\pi\chi^2(a)}. \quad (3.3)$$

It is important to note that equation (3.3) describes an integrated flux over the entire frequency spectrum, but generally the flux measured is monochromatic, i.e. that measured over a range of frequencies. Knowing that the luminosity distance ($d_L^{\text{[1]}}$) is defined as:

¹From now on, the subindex L will no longer be shown in the expressions, however, all the distances we will be dealing with are luminosity distances.

$$d_L = \frac{\chi(a)}{a}, \quad (3.4)$$

it is possible to keep equation (3.1) in terms of the luminosity distance:

$$F = \frac{L}{4\pi d^2}. \quad (3.5)$$

The apparent magnitudes (m) are defined in such a way as to vary logarithmically with the object's flux. The convention is such that a difference of 5 units in apparent magnitudes between two stars means that the lower magnitude object is 100 times brighter than the higher magnitude one. More precisely, the difference in apparent magnitudes for objects with measured fluxes F_1 and F_2 is given by [78]:

$$m_1 - m_2 = -2.5 \log_{10} \left(\frac{F_1}{F_2} \right), \quad (3.6)$$

or, taking the exponential of both sides, the relationship between their fluxes:

$$\frac{F_2}{F_1} = 10^{2(m_1 - m_2)/5}. \quad (3.7)$$

The connection between the apparent magnitude of a star and its distance is found by combining equations (3.5) and (3.7):

$$\frac{F_{10}}{F} = \left(\frac{d}{10 \text{ pc}} \right)^2 = 10^{2(m-M)/5}, \quad (3.8)$$

in which F_{10} is the flux that would be observed if the star were at a distance of 10 pc, d is its distance and M is defined as the apparent magnitude of the star at a distance of 10 pc. Isolating d in equation (3.8):

$$d = 10^{(m-M+5)/5} \text{ pc}. \quad (3.9)$$

The quantity $m - M$ is therefore a measure of the distance to the star and is called the distance modulus (μ_0):

$$\mu_0 = m - M = 5 \log_{10} \left(\frac{d}{1 \text{ pc}} \right) - 5 = 5 \log_{10} \left(\frac{d}{10 \text{ pc}} \right). \quad (3.10)$$

To be rigorous, the previous discussions should be considered as simplified, because in real life apparent magnitudes are measured by comparing the integrated observed flux of a source in a given frequency range defined by a particular bandpass filter with a reference flux also integrated in a given filter, not necessarily the same as the one used for the source. The expansion of the universe introduces an additional complication by stretching observed

wavelengths with respect to the emitted ones. Therefore, a more rigorous version of equation (3.10), would be $\mu_0 = 5 \log_{10} d + K$, where we have introduced the so called K-correction in order to properly account for the cosmos' expansion effect [80]. Nonetheless, all apparent magnitudes used in this dissertation are already K-corrected, so we should keep using from now on the simplified version of equation (3.10).

3.2 The rungs of the cosmic distance ladder

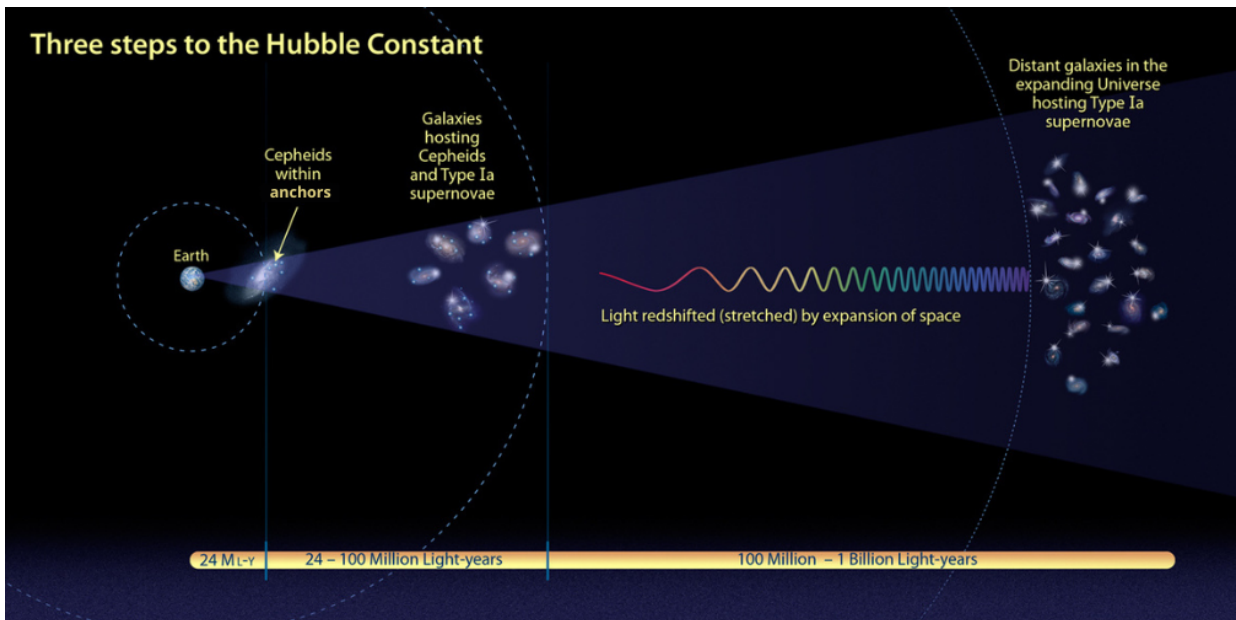


Figure 3.1: The cosmic distance ladder is generally divided into three main parts, i.e., three distance rungs. On the first rung (represented by the first dashed circle around the Earth) are the objects closest to the Solar System, from which distances can be determined directly by geometric parallax, as is the case for cepheids in anchors: M31, SMC, LMC and NGC4258. On the second rung, which is represented by the second dashed circle around the Earth, are the more distant cepheids, for which the period-luminosity relationship is used to determine their distances. In this rung, there are also supernovae and, as these objects follow a well-known light curve pattern, it is possible to determine their distances from their apparent and absolute magnitudes. And finally, on the third rung of cosmic distances, represented by the third dashed circle around the Earth, one can find the supernovae of the Hubble flow. The distances of these objects are determined by using their absolute magnitude obtained in the second rung together with their measured apparent magnitudes. Extracted from: <https://hubblesite.org/contents/media/images/2009/08/2494-Image.html?news=true>.

The cosmic distance ladder is divided into three main regions [77, 31], as presented in Figure 3.1. In the region closest to the Solar System, the first rung of the ladder, are the

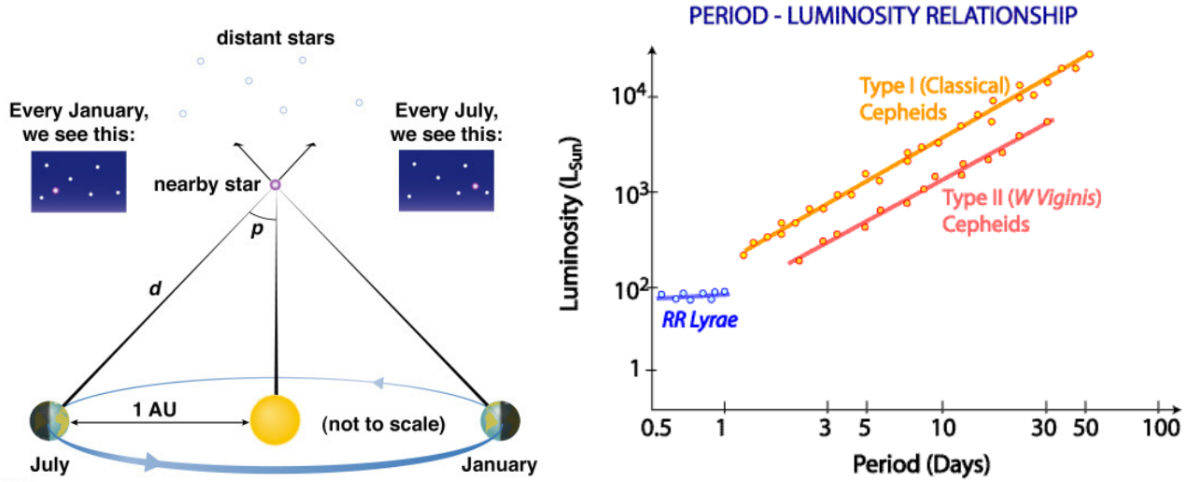


Figure 3.2: On the left, a diagram showing how the apparent position of closer objects varies in relation to more distant stars. By observing the same object at two different times of the year, it is possible to determine the angular separation $2p$ between its apparent positions. Since the distance from the Earth to the Sun is well known, it is possible to determine the distance d to the observed object using trigonometric properties, see equation (3.11) [75]. On the right, is a period-luminosity diagram for different types of cepheids, from which it is possible to see the relationship between the period of these variable stars and their luminosity [77]. Extracted from: <https://www.astro.sunysb.edu/fwalter/AST101/stars.html> & https://www.atnf.csiro.au/outreach/education/senior/astrophysics/variable_cepheids.html

variable cepheids belonging to the Milky Way and objects close to it, such as the Andromeda galaxy, the SMC, the Large Magellanic Cloud and the NGC4258 galaxy. Cepheids are stars with a variable brightness that depends on their pulsation period, which means that the brightness of a cepheid varies over well-determined periods of time [77]. The distances of these cepheids are determined mainly using the geometric parallax method [75]. This method is based on two observations of the same object at two different times of the year, because as the Earth moves along its orbit along the year, an object relatively close to the Earth will show an apparent movement in the sky with respect to the more distant stars, as shown on the left-hand side of Figure 3.2. So, by measuring the angular separation p due to this apparent movement and knowing the distance from the Earth to the Sun, 1 Astronomical Unit (AU), it is possible to determine the distance to the observed object using the following relationship:

$$d = \frac{1 \text{ AU}}{\sin(p)}. \quad (3.11)$$

In addition, first rung cepheids are also used to calibrate the Period-Luminosity (P-L) relationship of this class of objects. There is a correlation between the period and the

luminosity (or absolute magnitude) of the cepheids: the longer the period, the greater their absolute magnitude [77, 28, 81], as can be seen on the right-hand side of Figure 3.2 for different types of variable stars². Therefore, using the P-L diagram and measuring their apparent magnitudes, the distances to the farthest cepheids (for example, those of the second rung of the cosmic distance ladder containing type Ia supernovae) can be determined through equation (3.10) [31].

However, before applying equation (3.10) for cepheids of the second rung, these objects have to be standardized. The data shows that the absolute magnitude of cepheids depend not only on their pulsation periods, but also on their metallicity. Therefore, following the convention adopted in [31], and taking as standard a cepheid with pulsation period of one day and a metallicity equal to that of our Sun, we can replace (3.10) by:

$$\log_{10} \left(\frac{d}{\text{Mpc}} \right) = m_H^W - b_W(\log_{10} P - 1) - Z_W[\text{O}/\text{H}] - M_H^W - 25, \quad (3.12)$$

in which m_H^W and M_H^W are the apparent and absolute magnitudes of the cepheids, the latter determined from data of the first rung, since for these cepheids it is possible to measure the distance from parallax. These magnitudes have index and subindex W and H , respectively, because the magnitudes are dereddened (i.e. their apparent magnitudes are corrected to account for extinction in the Milky Way) according to Wesenheit [31] and their measurements were made in the H band (near infrared). P and $[\text{O}/\text{H}]$ are the period and metallicity data from the cepheids (measured in days and dex, respectively, O is the abundance of oxygen in relation to hydrogen H) and b_W and Z_W are the respective correction coefficients. Therefore, by measuring the apparent magnitude, pulsation period and metallicity of a cepheid on the second rung, one can infer its luminosity distance d .

Eventually, however, cepheids can no longer be used as a distance indicator, as it is not possible to differentiate one star from another in the sky due to their distances from the Solar System [77]. As a result, brighter objects are observed, which can be identified in the sky even at great distances, such as type Ia supernovae. These objects result from the explosive demise of white dwarfs, stellar remnants constrained by their physical characteristics to a mass limit of 1.4 solar masses (the Chandrasekhar limit³). In binary systems, these white dwarfs can undergo mass accretion from their companions, triggering a cataclysmic eruption

²Type I cepheids (classical cepheids) are young, massive and very luminous stars, with higher metallicity and periods of days to months. Type II cepheids (W Viginis cepheids) are older stars than type I, less massive, less luminous, with lower metallicity and periods similar to those of type I. The RR Lyrae stars are also variable stars. However, unlike the cepheids, which are supergiants with masses around 50 times greater than the mass of the Sun, the RR Lyrae are even less massive than the Sun. They are less luminous than the cepheids, much more common and with very short periods (of hours) extremely regular.

³From the physical point of view, the Chandrasekhar limit marks the highest mass whose gravitational pull can still be supported by electron degeneracy pressure.

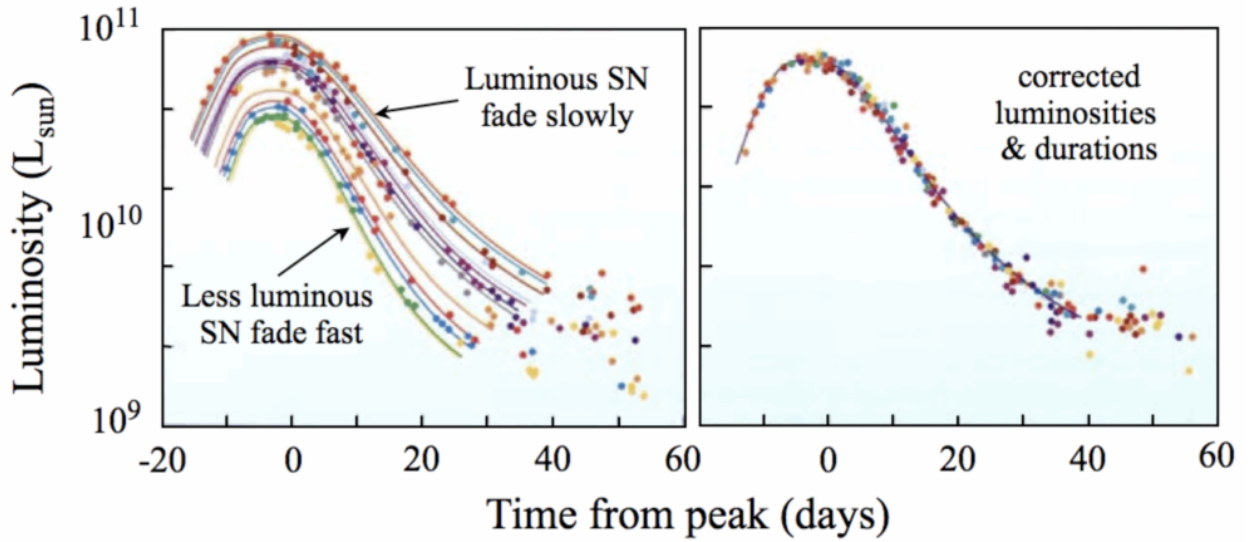


Figure 3.3: On the left, light curves of several supernovae before standardization via stretch and color parameters. On the right, the same light curves after standardization. From the standardized light curve, it is possible to obtain the absolute magnitude of this class of objects, which allows their distances to be determined, once the apparent magnitudes are measured, see equation (3.14). Extracted from: <https://johnlucey.webspace.durham.ac.uk/bridge/n2015m-bridge/>

which originate the SNIa. The luminosity of these supernovae is exceptionally high, and they undergo detonation at a consistent stage in their evolutionary process [42]. Examples of SNIa light curves can be seen in Figure 3.3, where the luminosity, in units of solar luminosity, is plotted as a function of time, in days since the peak luminosity was achieved [82, 83]. It is possible to see that the light curves on the left are slightly different. We see that the longer the light curve tail the brighter the supernova, a feature first identified in [84]. However, they can be standardized in order to obtain a universal luminosity for Type Ia Supernova (SNIa). The corrections considered are stretch (x_1), which is related to how quickly the SNIa decreases in brightness, and color (c), which is essentially the difference between the apparent magnitudes measured in the B and V bands (B-V) at peak brightness.

These two parameters can be obtained, for example, through the SALT2 [85] light curve parameterization, which considers a flux model given by the following equation:

$$F(\text{SN}, p, \lambda) = x_0 \times [M_0(p, \lambda) + x_1 M_1(p, \lambda) + \dots] \times \exp[cCL(\lambda)] \quad (3.13)$$

in which F is the flux measured in W m^{-2} , p is the time and λ the wavelength in the rest-frame of the SN (this parameter is related to the K-correction). x_0 is the overall flux normalization, $M_0(p, \lambda)$ is the average spectral sequence, $M_k(p, \lambda)$, for $k > 0$, are additional

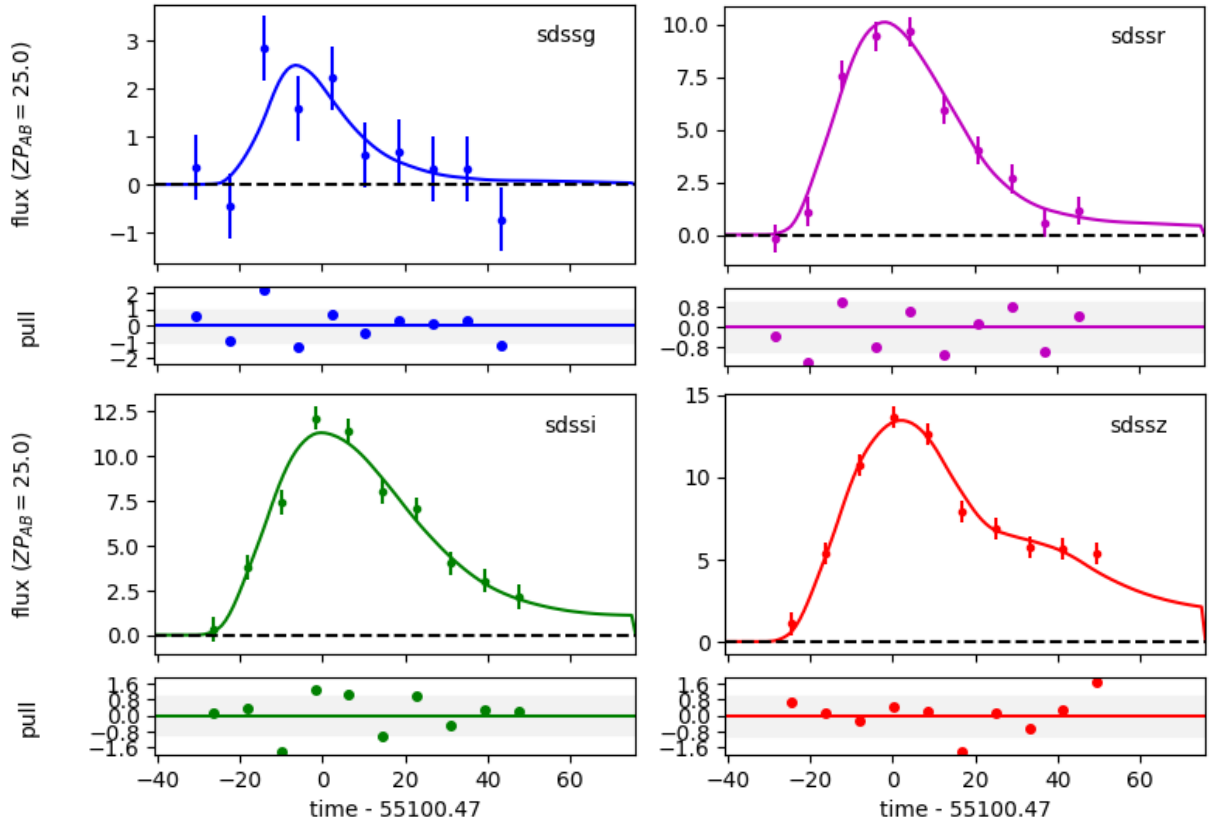


Figure 3.4: Light curves in different bands of the Sloan Digital Sky Survey (SDSS) for the example data set from SNCosmo [1]. This data set is synthetic and was generated based on the real sample of the SDSS.

components that describe the main variability of SNeIa and $CL(\lambda)$ represents the average color correction law. The last three components are determined from the model training process, whereas the free parameters (x_0 , x_1 and c) are fitted by SALT2 [85, 86].

We have used the package SNCosmo [1] in order to perform illustrative fits of SNIa light curves. Figure 3.4 shows light curves (experimental points) in four different Sloan Digital Sky Survey (SDSS) bands (sdssg, sdssr, sdssi, sdssz), as well as the corresponding SALT2 fitted models (solid lines). Fit residuals in units of standard deviations (i.e. pulls) are also shown at the bottom of each light curve. It is possible to see from these plots that the shape of the light curves changes depending on the band that they are observed. In this case, the fitted parameters are: $x_0 = (1.180 \pm 0.038) \times 10^{-5}$, $x_1 = (0.59 \pm 0.36)$ and $c = (0.206 \pm 0.036)$.

Figure 3.5 shows variations of the fitted light curve model of Figure 3.4, where we varied the stretch (right) and color (left) parameters in order to evince their role in shaping the curves. We can clearly see the impact of stretch on the widths and tail decay rates of the curves, as well as the effect of extinction through the color parameter.

Furthermore, some analyses consider another correction related to the stellar mass (M_*)

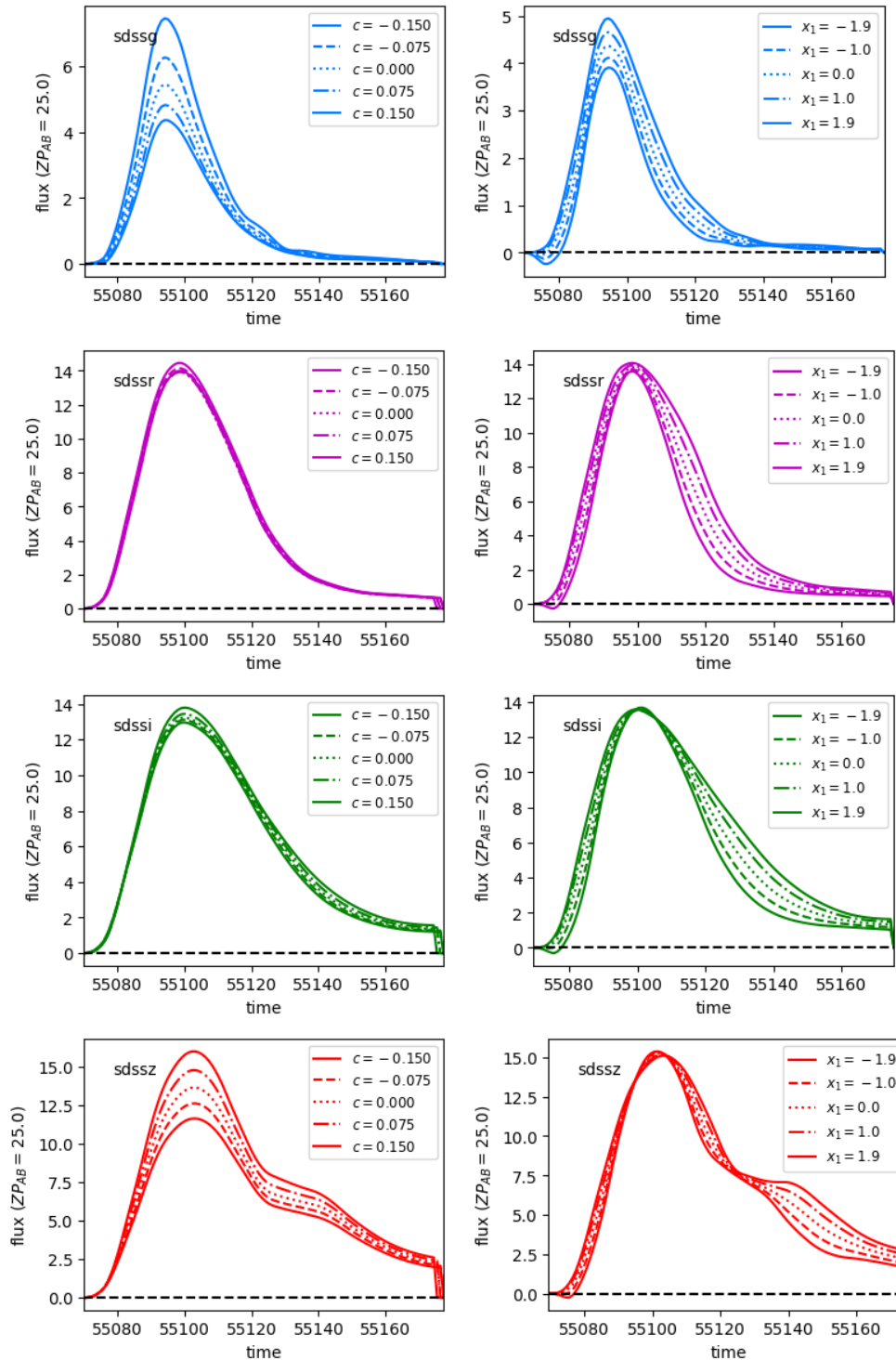


Figure 3.5: Light curves in different bands of the Sloan Digital Sky Survey (SDSS), in which the magnitude is plotted as a function of time (in days). Color (c) and stretch (x_1) were varied on the left and right-hand side of the plots, respectively. It is possible to verify that the main role of the color parameter is to change the amplitude of the curve, whereas the stretch parameter is responsible for varying the width.

of the host galaxy ($\log_{10}(M_*/M_\odot)$, in which M_\odot is the solar mass), due to the apparent correlations between supernova luminosity and its host stellar mass [87, 88]. In this way, it is possible to determine the absolute magnitude (M_B) of a given supernova from its light curve [89], using a sample of supernovae in hosts that also have cepheids with well-determined distances. Therefore, by measuring the apparent uncorrected magnitude $m_{B,unc}$, stretch, color and host mass, it is possible to determine the distance (in Mpc) of the supernova [31]:

$$5 \log_{10}(d) = m_{B,unc} + \alpha x_1 - \beta c + \gamma \left[1 + \exp \left(\frac{\log_{10}(M_*/M_\odot) - 10}{0.01} \right) - \frac{1}{2} \right] - M_B - 25, \quad (3.14)$$

in which α , β and γ are parameters that can be fitted to the data.

And finally, in the third distance rung, one can find the supernovae present in the Hubble flow. The luminosity distance to these objects is determined using equation (3.14), but there is another important piece of information associated to these objects for determining the Hubble constant: the redshift (z). The distance modulus μ_0 of a SNIa in the Hubble flow can be written in terms of its cosmological redshift, for smallish z :

$$\mu_0 = 5 \log_{10} \left\{ cz \left[1 + \frac{1}{2}(1 - q_0)z - \frac{1}{6}(1 - q_0 - 3q_0^2 + j_0)z^2 + O(z^3) \right] \right\} - 5 \log_{10}(H_0) + 25, \quad (3.15)$$

in which q_0 and j_0 are the deceleration and jerk parameters, respectively. Recalling that μ_0 can be expressed also in terms of the apparent and absolute magnitudes of an object, as in equation (3.10), it is possible to write H_0 (in $\text{km s}^{-1} \text{Mpc}^{-1}$) as:

$$5 \log_{10}(H_0) = 5 \log_{10} \left\{ cz \left[1 + \frac{1}{2}(1 - q_0)z - \frac{1}{6}(1 - q_0 - 3q_0^2 + j_0)z^2 + O(z^3) \right] \right\} + 25 + M_B - m_B. \quad (3.16)$$

In other words, from measurements of the apparent magnitudes and redshifts of SNIa and input values for their absolute magnitude and the universe deceleration and jerk parameters, it is possible to infer H_0 [31].

It is important to emphasize that there are other distance indicators like Tip of the Red-Giant Branch [90, 91], Surface Brightness Fluctuation [92], Bright Standard Sirens [93, 94], Eclipsing Binaries [95, 96] and Interstellar Masers [97], of which the last two were used in Riess et al. (2022) [31] to obtain complementary constraints to those provided by cepheids in SMC-LMC and NGC4258, respectively. These three objects (SMC, LMC and NGC4258) are known as anchors because their distances can be determined independently, without the need to measure the apparent magnitude of their cepheids.

3.3 Combined fit of all ladder rungs

The cosmic distance ladder data can be organized into vectors and matrices, so that it is possible to estimate its theoretical parameters using the least squares method or MCMC, for example, as was done in Riess et al. (2022) [31]. The data and theoretical parameters can be written in terms of vectors, theoretical equations and covariance data can be expressed as matrices. With these components, we are able to fit the data minimizing a χ^2 or sampling the data.

In this work, \mathbf{y} represents the data vector for all the objects used in the fit:

$$\mathbf{y} = \left(\begin{array}{c} m_{H,1}^W \\ \dots \\ m_{H,nh}^W \\ \hline m_{H,N4258}^W - \mu_{0,N4258} \\ m_{H,M31}^W \\ m_{H,LMC}^W - \mu_{0,LMC} \\ m_{H,SMC}^W - \mu_{0,SMC} \\ \hline m_{B,1} \\ \dots \\ m_{B,ncc} \\ \hline M_{H,HST}^W \\ M_{H,Gaia}^W \\ 0 \\ 0 \\ 0 \\ \hline m_{B,1} - 5 \log_{10}\{cz_1[\dots]\} - 25 \\ \dots \\ m_{B,nhf} - 5 \log_{10}\{cz_{nhf}[\dots]\} - 25 \end{array} \right) \begin{array}{l} \text{Cepheids in SNeIa hosts} \\ \\ \text{Cepheids in anchors} \\ \\ \text{SNeIa in cepheid hosts} \\ \\ \text{External constraints} \\ \\ \text{SNeIa in the Hubble flow} \end{array} \quad (3.17)$$

This vector contains data from the three rungs of the cosmic distance ladder. From top to bottom, the first block contains data on the apparent magnitude of cepheids (m_H^W) in the SNeIa hosts (nh is the total number of cepheids in hosts of cepheids - SNeIa), i.e., data referring to the second rung. In the second block, there are both data on the apparent magnitude of cepheids and combinations of these magnitudes with the distance moduli (μ_0) of the anchors that contain these objects, NGC4258, LMC and M31, located in the first

distance rung. Then, in the third block, there are data in the form of the apparent magnitude of supernovae (m_B) in hosts that also have cepheids (ncc is the total number of supernovae in the hosts of cepheids - SNeIa), which belong to the second rung. In the fourth block, there is a set of five (5) external parameters: two (2) independent determinations of the absolute magnitude of the cepheids (Hubble Space Telescope [23] and Gaia [30]) and three (3) constraints to possible systematic differences in the determination of the distance moduli of the anchors NGC4258 and LMC and between terrestrial and space photometry (Δzp) for LMC cepheids (the photometric measurements of these cepheids were obtained from ground-based observations and by HST, respectively. Cosmic distances were calibrated with 1% precision with these measurements). Finally, the fifth block contains data in the form of quantities involving the apparent magnitude and redshift of supernovae in the Hubble flow (nhf is the total number of these supernovae), which correspond to third rung data.

The theoretical equations providing the predictions for the elements of the data vector \mathbf{y} can be obtained in the form of a matrix-vector product $\mathbf{y}_{\text{th}} = \mathbf{L}\mathbf{q}$, where \mathbf{q} is the vector of theoretical parameters and \mathbf{L} is given by:

$$\mathbf{L} = \begin{pmatrix}
 1 & \dots & 0 & 1 & 0 & 0 & \log_{10} P_1 - 1 & 0 & [\text{O}/\text{H}]_1 & 0 & 0 \\
 \dots & \dots & \dots & \dots & \dots & \dots & \dots & \dots & \dots & \dots & \dots \\
 0 & \dots & 1 & 1 & 0 & 0 & \log_{10} P_{\text{nh}} - 1 & 0 & [\text{O}/\text{H}]_{\text{nh}} & 0 & 0 \\
 \hline
 0 & \dots & 1 & 1 & 0 & 0 & \log_{10} P_{\text{N4258}} - 1 & 0 & [\text{O}/\text{H}]_{\text{N4258}} & 0 & 0 \\
 0 & \dots & 0 & 1 & 0 & 1 & \log_{10} P_{\text{M31}} - 1 & 0 & [\text{O}/\text{H}]_{\text{M31}} & 0 & 0 \\
 0 & \dots & 0 & 1 & 1 & 0 & \log_{10} P_{\text{LMC}} - 1 & 0 & [\text{O}/\text{H}]_{\text{LMC}} & 0 & 0 \\
 0 & \dots & 0 & 1 & 1 & 0 & \log_{10} P_{\text{SMC}} - 1 & 0 & [\text{O}/\text{H}]_{\text{SMC}} & 0 & 0 \\
 \hline
 1 & \dots & 0 & 0 & 0 & 0 & 0 & 1 & 0 & 0 & 0 \\
 \dots & \dots & \dots & \dots & \dots & \dots & \dots & \dots & \dots & \dots & \dots \\
 0 & \dots & 1 & 0 & 0 & 0 & 0 & 1 & 0 & 0 & 0 \\
 \hline
 0 & \dots & 0 & 1 & 0 & 0 & 0 & 0 & 0 & 0 & 0 \\
 0 & \dots & 0 & 1 & 0 & 0 & 0 & 0 & 0 & 0 & 0 \\
 0 & \dots & 0 & 0 & 0 & 0 & 0 & 0 & 0 & 1 & 0 \\
 0 & \dots & 1 & 0 & 0 & 0 & 0 & 0 & 0 & 0 & 0 \\
 0 & \dots & 0 & 0 & 1 & 0 & 0 & 0 & 0 & 0 & 0 \\
 \hline
 0 & \dots & 0 & 0 & 0 & 0 & 0 & 1 & 0 & 0 & -1 \\
 \dots & \dots & \dots & \dots & \dots & \dots & \dots & \dots & \dots & \dots & \dots \\
 0 & \dots & 0 & 0 & 0 & 0 & 0 & 1 & 0 & 0 & -1
 \end{pmatrix}$$

Cepheids-SNeIa

NG4258 anchor

M31 anchor

LMC anchor

SMC anchor

SNeIa-cepheids

External constraints

SNeIa in the Hubble flow

(3.18)

which has a dimension of (number of data) \times (number of theoretical parameters). This matrix

follows the same order as the data presented in the vector \mathbf{y} . And the model parameters to be adjusted are given by:

$$\mathbf{q} = \begin{pmatrix} \mu_{0,1} \\ \dots \\ \mu_{0,k} \\ \Delta\mu_{\text{N4258}} \\ M_H^W \\ \Delta\mu_{\text{LMC}} \\ \mu_{\text{M31}} \\ b_W \\ M_B \\ Z_W \\ \Delta z_p \\ 5 \log_{10}(H_0) \end{pmatrix} \quad (3.19)$$

in which $\mu_{0,k}$ is the distance modulus of the k -th cepheid hosts on the second rung, M_H^W the absolute magnitude of the cepheids, μ_{M31} the distance modulus of the anchor M31, b_W the standardization coefficient for the periods of the cepheids, M_B the absolute magnitude of the supernovae and Z_W the standardization coefficient for the metallicities of the cepheids. By multiplying the matrix \mathbf{L} by the vector of parameters \mathbf{q} , the theoretical parameters $\mathbf{y}_{\text{th}} = \mathbf{L}\mathbf{q}$ are obtained. For example, for the cepheids of the second rung (first part of the vector \mathbf{y}):

$$m_H^W = \mu_0 + M_H^W + b_W(\log_{10} P - 1) + Z_W[\text{O}/\text{H}]. \quad (3.20)$$

This equation is also valid for the first rung cepheids present in M31 (the second part of \mathbf{y}). For the other first rung cepheids (also in the second part of \mathbf{y}), belonging to the LMC, SMC and NGC4258, the following equation is obtained from $\mathbf{y} = \mathbf{L}\mathbf{q}$:

$$m_H^W - \mu_0 = M_H^W + b_W(\log_{10} P - 1) + Z_W[\text{O}/\text{H}] + \Delta\mu_0. \quad (3.21)$$

where $\Delta\mu_0$ is the difference between the fitted value for the distance modulus and the value of the independent measurement of that quantity. For supernovae in cepheid hosts (the third part of \mathbf{y}) the following equation is valid:

$$m_B = \mu_0 + M_B, \quad (3.22)$$

and this expression is different from equation (3.14) because the apparent magnitudes of

these supernovae are already standardized by color, stretch and mass step. For the external constraints, the fourth part of \mathbf{y} , we have:

$$M_{H,\text{HST}}^W = M_H^W, \quad (3.23)$$

$$M_{H,\text{Gaia}}^W = M_H^W, \quad (3.24)$$

$$0 = \Delta z p, \quad (3.25)$$

$$0 = \Delta \mu_{\text{NGC4258}}, \quad (3.26)$$

$$0 = \Delta \mu_{\text{LMC}}, \quad (3.27)$$

because, in theory, the absolute magnitudes for cepheids estimated by the HST and Gaia must be equal to the fitted value M_H^W . The differences between the fitted values of distance moduli for the anchors NGC4258 and LMC and their independent estimates for these quantities must be also zero. Furthermore, there should be no difference between the photometry measurements obtained from the HST and the ground-based equipment. And finally, for the SNeIa in the Hubble flow, the last part of \mathbf{y} , the following equation is obtained:

$$m_B - 5 \log_{10} \left\{ cz \left[1 + \frac{z}{2}(1 - q_0) + O(z^2) \right] \right\} - 25 = M_B - 5 \log_{10}(H_0). \quad (3.28)$$

Thus, from the vectors \mathbf{y} , \mathbf{q} , the matrix \mathbf{L} and the data covariance matrix \mathbf{C} (see Appendix [A](#) for more information), as well as an assumption of gaussianity for the measurement uncertainties, it is possible to assemble a χ^2 .

$$\chi^2 = (\mathbf{y} - \mathbf{L}\mathbf{q})^T \mathbf{C}^{-1} (\mathbf{y} - \mathbf{L}\mathbf{q}). \quad (3.29)$$

Since the model is fully linear in all the parameters, the least squares solution gives the vector of best-fit parameters \mathbf{q}_{best} :

$$\mathbf{q}_{\text{best}} = (\mathbf{L}^T \mathbf{C}^{-1} \mathbf{L})^{-1} \mathbf{L}^T \mathbf{C}^{-1} \mathbf{y}. \quad (3.30)$$

The covariances of the parameters that compose the vector of best-fit are given by the following matrix:

$$\mathbf{C}\mathbf{q}_{\text{best}} = (\mathbf{L}^T \mathbf{C}^{-1} \mathbf{L})^{-1}. \quad (3.31)$$

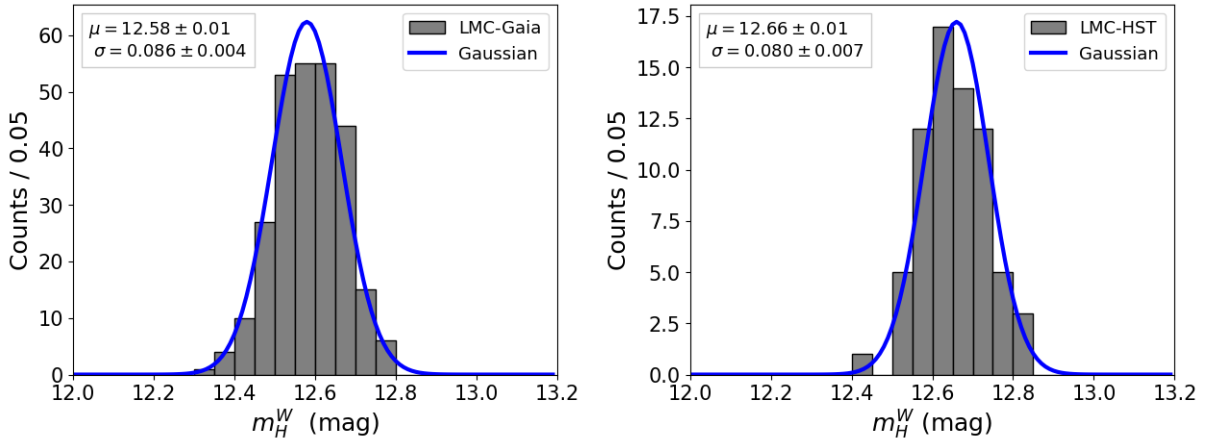


Figure 3.6: Distributions of apparent magnitudes of SH0ES cepheids in the LMC, separated by telescopes: Gaia and Hubble Space Telescope (HST). The blue curves represent Gaussian fits, whose mean and standard deviations are shown as insets in the plots.

3.4 Cosmic distance ladder data from R22

All the data from the cosmic distance ladder were taken from Riess et al. (2022), which was made available through GitHub⁴, with the cepheid data obtained through the SH0ES [24] program and the supernova data taken from the Pantheon+ catalog [98]. Cepheid data, specifically from the LMC, were collected by different telescopes: Gaia and HST. Figure 3.6 shows the distributions of apparent magnitudes for LMC cepheids collected by each instrument separately. We can see that the dispersion and average values of both distributions are similar. Despite these similarities, a possible difference in the zero point of the two photometries around 0.1 mag would not be easy to identify by visual inspection of the distributions. Therefore, as discussed before, a hypothetical zero point difference between ground- and space-based photometries (Δzp) is included in the model to be fitted to the data.

Figure 3.7 shows the scatter plots apparent magnitude \times log-period for SH0ES first rung cepheids. Black points represent data as they are available directly from SH0ES provided FITS files, showing that pulsation period standardization was already performed. This implies that the expected value for the b_W coefficient of equation (3.12) is zero. On the other hand, the red dots show the expected dependence on $\log_{10}(P/\text{days})$ when the period standardization is reverted. However, for the sake of consistency with the literature, from now on, we should work with pre-standardization cepheid magnitudes.

⁴<https://github.com/PantheonPlusSH0ES/DataRelease>

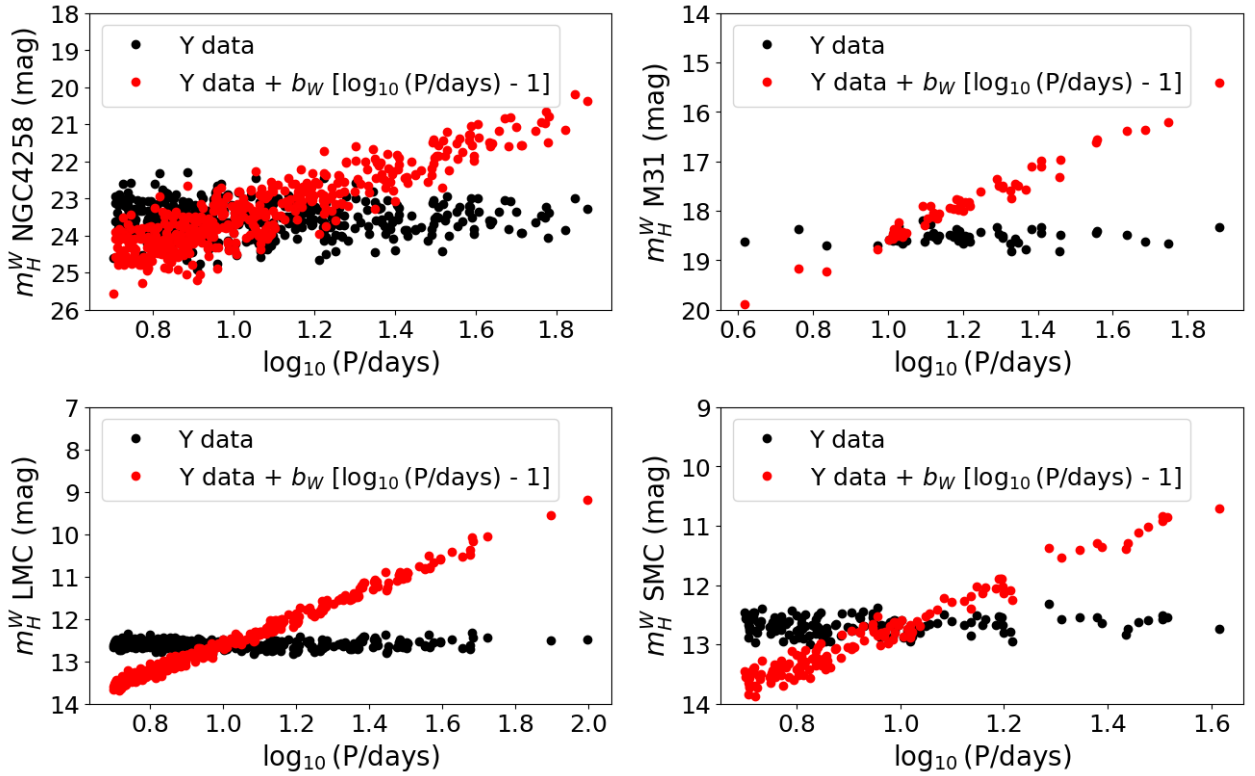


Figure 3.7: Apparent magnitudes of SH0ES first rung cepheids versus the period in logarithmic scale. The data is shown after (black) and before (red) pulsation period standardization. As the apparent magnitude data for cepheids provided by R22 were corrected by period, we needed to reconsider these data into the fit to obtain the same results as this reference.

Figure 3.8 shows the sky maps for the cepheids on the first and second rungs of the cosmic distance ladder. It can be seen from the first map that there are four regions of the sky where the cepheids accumulate, which correspond to the anchors of the first rung: M31, LMC, SMC and NGC4258. In the second map, there are 37 regions where Cepheids accumulate, which correspond to the cepheid and supernova hosts of the second rung. Although the regions of some hosts appear as point-like sources, they actually contain each a population of objects.

Figure 3.9 shows the sky maps for supernovae on the second and third rungs of the cosmic distance ladder. Since the first map refers to supernovae on the second rung, 37 regions are expected where these objects accumulate, since the galaxies hosting supernovae on the second rung are the same as those hosting the cepheids on this rung. The second sky map should contain 277 dots, which represent the supernovae of the third rung; the accumulation of these objects in the bottom-left part of the map identifies the SDSS Stripe 82, a 270 deg² region of the equatorial plane. The boundaries of the stripe are: $-50 < \text{RA} < 59$ and $-1.25 < \text{DEC} < 1.25$ (J2000). In these maps, the color of the dots follows a scale that quantifies the peculiar velocity along the line-of-sight of the SNeIa (v).

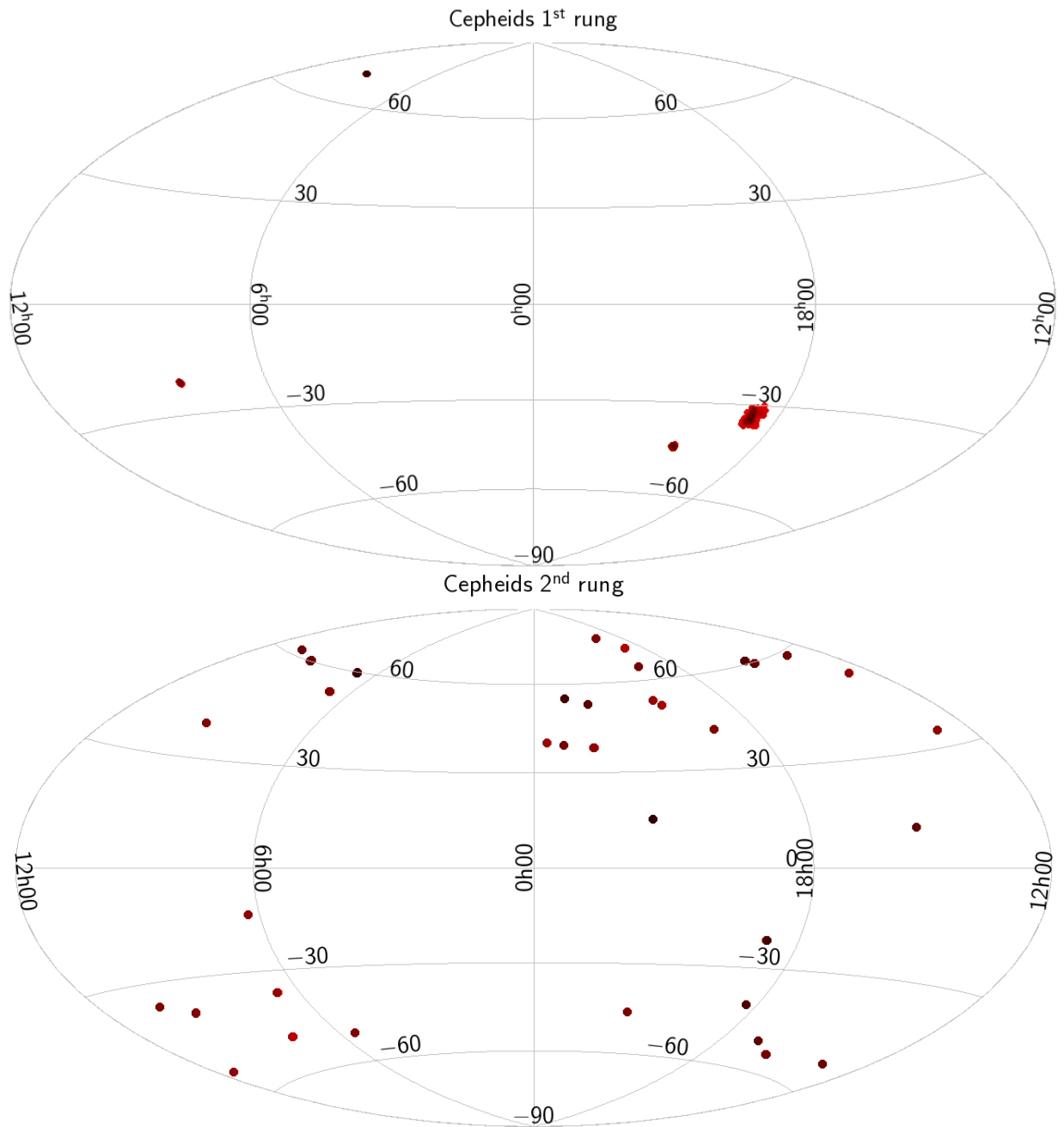


Figure 3.8: Top: sky map (Aitoff projection) in galactic coordinates showing SH0ES cepheids belonging to the first rung of the distance ladder. It is possible to verify that there are four regions on the map, on the upper part the cepheids belonging to NGC4258, at the bottom left the cepheids from M31 and on the right the cepheids belonging to SMC and LMC. Bottom: sky map for the cepheids from the second rung. There are 37 regions associated to the cepheid hosts and in each region the cepheids belonging to the host.

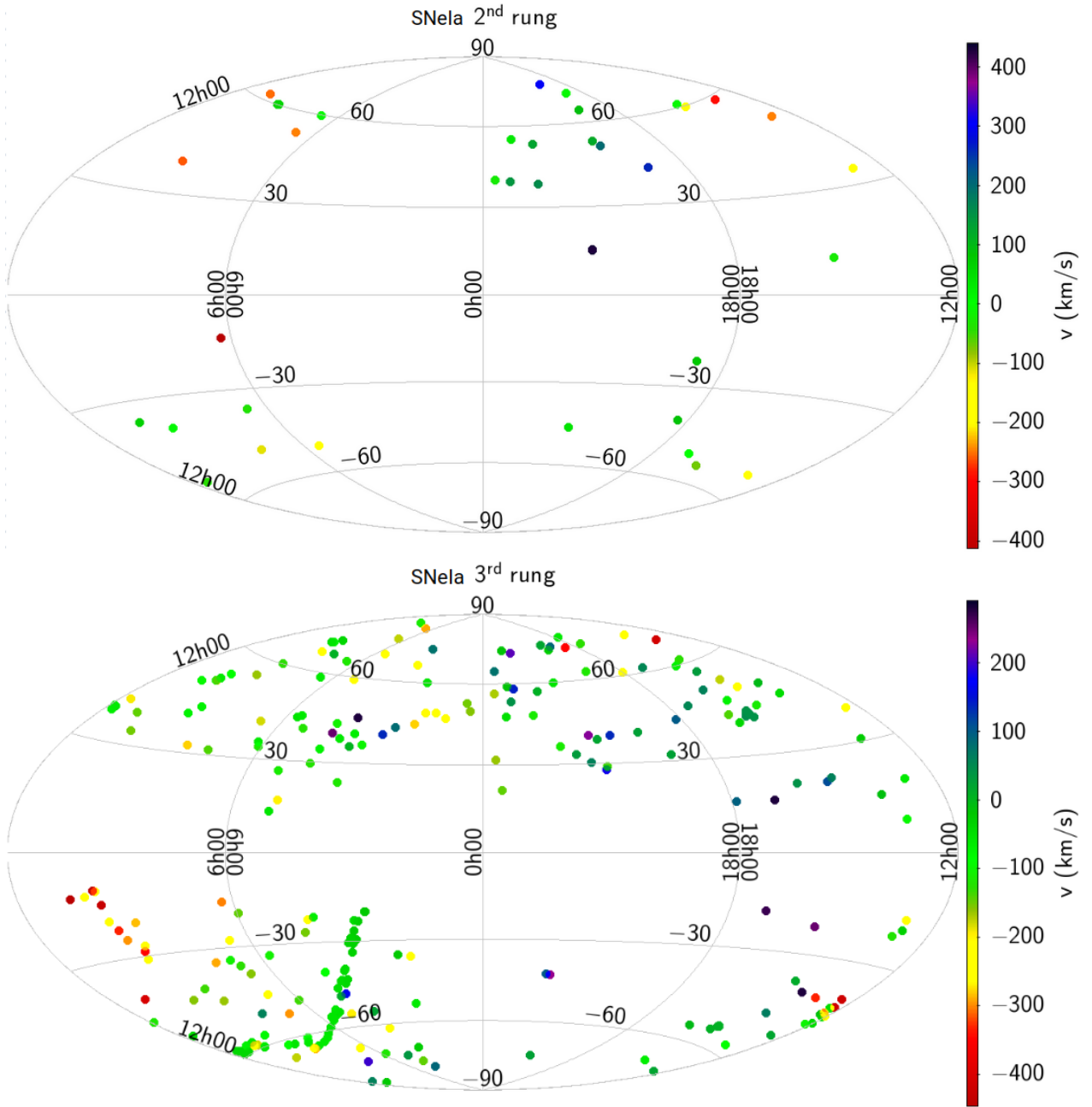


Figure 3.9: Top: sky map (Aitoff projection) in galactic coordinates of SH0ES/Pantheon+ SNeIa of the second rung. Again, there are 37 regions that are the same hosts of the cepheids and SNeIa. Bottom: supernovae of the third rung (277 in total). An accumulation of objects along the Earth’s equatorial plane can be seen at the bottom left part of the map and is associated to SDSS stripe 82. In both graphs, the points change color according to the peculiar velocity along the line-of-sight (v , the Hubble flow has been subtracted) of the objects.

	Original R22 [31]		This work (R22)	
	χ^2	MCMC	χ^2	MCMC
$\Delta\mu_{N4258} \pm \sigma_{\Delta\mu_{N4258}}$	-0.015 ± 0.022	-0.013 ± 0.022	-0.013 ± 0.022	-0.012 ± 0.022
$M_H^W \pm \sigma_{M_H^W}$	-5.897 ± 0.018	-5.894 ± 0.018	-5.894 ± 0.018	-5.893 ± 0.018
$\Delta\mu_{LMC} \pm \sigma_{\Delta\mu_{LMC}}$	0.009 ± 0.019	0.010 ± 0.019	0.010 ± 0.019	0.010 ± 0.019
$\mu_{M31} \pm \sigma_{\mu_{M31}}$	24.372 ± 0.069	24.371 ± 0.069	24.371 ± 0.069	24.370 ± 0.069
$b_W \pm \sigma_{b_W}$	-3.299 ± 0.015	-3.298 ± 0.015	-3.313 ± 0.015	-3.312 ± 0.015
$M_B \pm \sigma_{M_B}$	-19.238 ± 0.027	-19.253 ± 0.029	-19.253 ± 0.029	$-19.253_{-0.029}^{+0.030}$
$Z_W \pm \sigma_{Z_W}$	-0.206 ± 0.044	$-0.217_{-0.046}^{+0.045}$	-0.217 ± 0.045	$-0.218_{-0.044}^{+0.046}$
$\Delta zp \pm \sigma_{\Delta zp}$	-0.065 ± 0.010	-0.074 ± 0.011	-0.074 ± 0.011	-0.074 ± 0.011
$5 \log_{10}(H_0) \pm \sigma_{5 \log_{10}(H_0)}$	9.318 ± 0.030	9.318 ± 0.030	9.318 ± 0.030	$9.318_{-0.031}^{+0.030}$
$H_0 \pm \sigma_{H_0}$	73.04 ± 1.01	73.04 ± 1.01	73.04 ± 1.01	$73.04_{-1.04}^{+1.01}$
χ^2/ndof	3548/3446	-	3548/3446	-

Table 3.1: Best fit values for 9 of the total 46 distance ladder parameters (see equation (3.19)) obtained through the least squares solution (equation (3.30)) and as the median values of the posterior distributions sampled by an MCMC. Left: values taken from R22. Right: Corresponding values obtained in this work. The small differences between the mean values of the two studies may be due to the addition of cepheid period data by hand in the fit carried out in the present work.

3.4.1 Best fit solution for R22 data

Based on the R22 data set, and considering the procedure presented in section 3.3, it was possible to minimize the χ^2 given by equation (3.29) and obtain the \mathbf{q}_{best} solution, which provided the parameters shown in the third column of Table 3.1. This table also shows the values obtained originally by R22 [31], showing that our results are fully consistent with them. The overall quality of the fits seems to be very good based on the χ^2 . It is worth mentioning that the total number of degrees of freedom in this fit is given by⁵

$$\text{ndof} = \underbrace{3492}_{\text{all data}} - \underbrace{37}_{\mu_0 \text{ of SN-cepheid hosts}} - \underbrace{9}_{\Delta\mu_{N4258}, \dots, 5\log_{10}(H_0)} = 3446. \quad (3.32)$$

Additional quality tests have been performed by analyzing both the distributions of residuals and pulls, defined for the i -th element of the data vector as:

$$\text{Residual}_i \equiv [\mathbf{y} - \mathbf{L}\mathbf{q}_{\text{best}}]_i, \quad \text{Pull}_i \equiv \frac{[\mathbf{y} - \mathbf{L}\mathbf{q}_{\text{best}}]_i}{\mathbf{C}_{ii}^{1/2}}, \quad (3.33)$$

⁵Bear in mind also that a given object in the ladder can have multiple independent measurements.

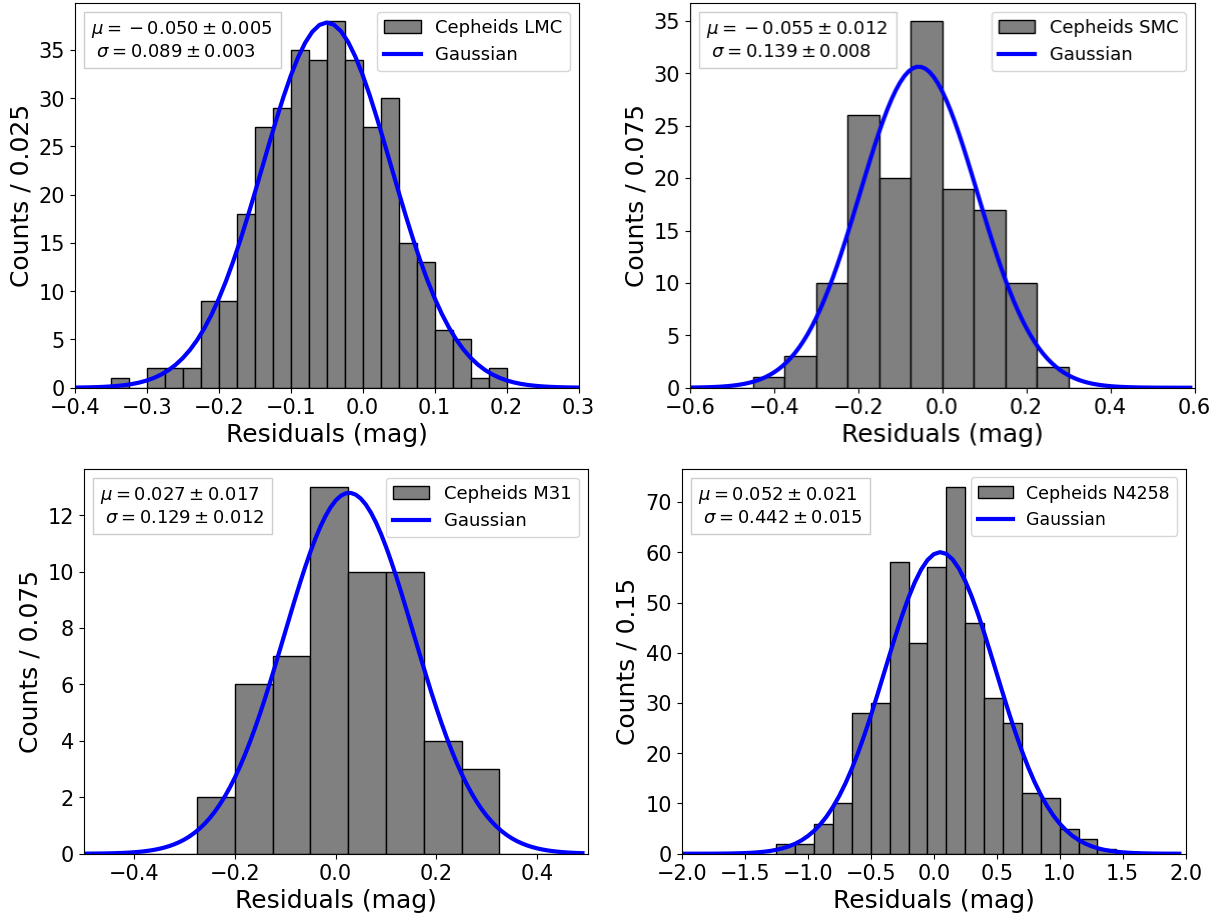


Figure 3.10: Histograms of residuals for the real data of the first rung cepheids in the distance ladder, separated into anchors. Here residuals mean (data-theory), furthermore, the mean value (μ) and the variance (σ) of these histograms were obtained by maximum likelihood estimation.

pull is a kind of normalization of residuals made with the uncertainties of the data. When the measures of residuals come from different sources, this normalization is necessary to compare the data from different types. See from equation (3.33) that we are neglecting the contribution to the pull coming from off-diagonal elements of the covariance matrix. Therefore, if correlations between data points are non-negligible, there might appear distortions in the histograms with respect to the zero-mean, unit variance Gaussian characteristic of independent random variables.

The histograms of residuals for the cepheids on the first rung are separated by anchors in Figure 3.10. These histograms show the mean values (μ) and standard deviations (σ) of the Gaussians fitted to the real data. It can be seen that the average values are very close to zero, which means that the real data is in agreement with the theoretical equations and the fitted values from \mathbf{q}_{best} .

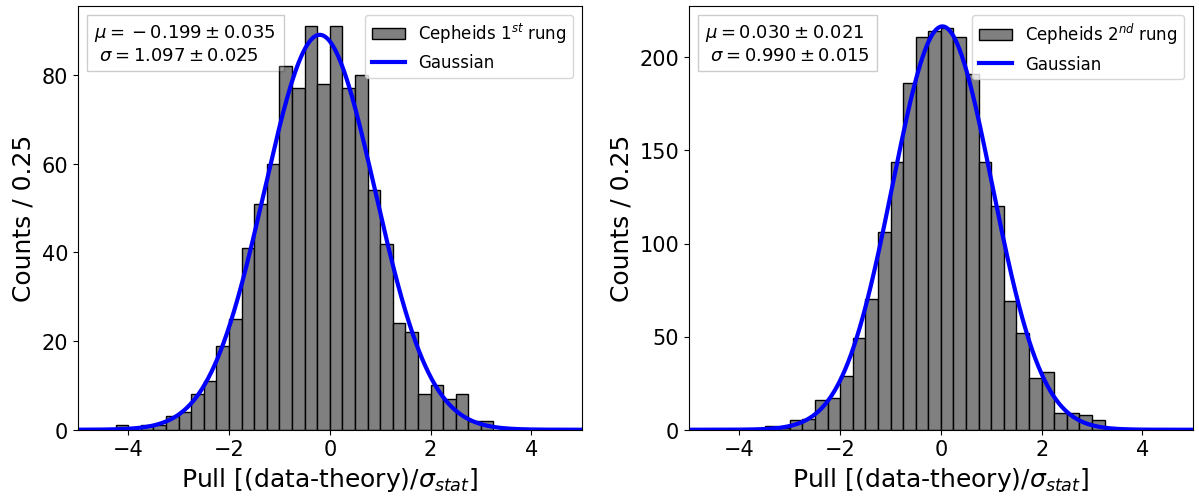


Figure 3.11: Histograms of the real data of the first and second rung cepheids in the distance ladder. Here, pulls $[(\text{data-theory})/\sigma_{\text{stat}}]$ are presented instead of residuals because there are data from different anchors in each plot. The mean value (μ) and the variance (σ) of these histograms were obtained by maximum likelihood estimation.

Figure 3.11 shows the pull histograms for the cepheid data from the first (left) and second (right) rung of the distance ladder. The plot on the left is the union of the data shown in Figure 3.10. Figure 3.12 shows the residual histograms of the real data of supernovae from the second and third rungs. On the left, one can find the residuals for apparent magnitude data from second rung supernovae, and on the right, from third rung supernovae. Again, the Gaussian fit performed on the histograms shows that the data is centered on approximately

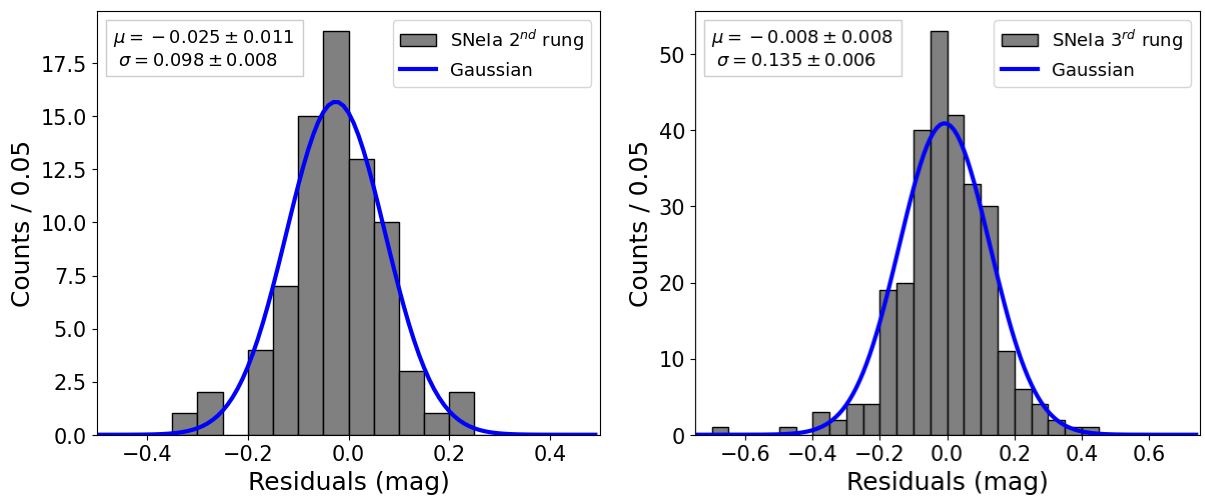


Figure 3.12: Histograms of the real data of the second and third rung SNeIa in the distance ladder. Here residuals means (data-theory) , furthermore, the mean value (μ) and the variance (σ) of these histograms were obtained by maximum likelihood estimation.

Rung	Anchor/host	N	$\mu \pm \sigma_\mu$	$\sigma \pm \sigma_\sigma$
1 st	LMC (R)	339	-0.050 ± 0.005	0.089 ± 0.003
	SMC (R)	143	-0.055 ± 0.012	0.139 ± 0.008
	M31 (R)	55	0.027 ± 0.017	0.129 ± 0.012
	N4258 (R)	443	0.052 ± 0.021	0.442 ± 0.015
	all cepheids (P)	980	-0.199 ± 0.035	1.097 ± 0.025
2 nd	all cepheids (P)	2150	0.030 ± 0.021	0.990 ± 0.015
	all SNeIa (R)	77	-0.025 ± 0.011	0.098 ± 0.008
3 rd	all SNeIa (R)	277	-0.008 ± 0.008	0.135 ± 0.006

Table 3.2: Average values and standard deviations of the histogram of residuals (R) and pulls (P) for different objects in the cosmic distance ladder. N is the number of objects in each part of the ladder, σ_μ and σ_σ are the uncertainties related to the average value and standard deviation of the histograms.

zero and that the standard deviations of each rung are comparable, but more fluctuation is seen on the magnitudes of the third rung.

Table 3.2 summarizes the average values and standard deviations fitted to different objects of the cosmic distance ladder. The standard deviations shown in this table represent the typical scale of the statistical fluctuations of the data around the theoretical model. They will be extremely useful in this work, because we shall use them in the next chapter to set a reference scale with respect to which we will measure systematic uncertainties to be introduced into synthetic data in a controlled situation.

Monte Carlo Markov Chains: real data

In addition to the fits made using the least squares method (χ^2), we sampled the χ^2 statistic using MCMC in order to reconstruct the posterior distributions of the model parameters. The emcee package [2], a sampler for MCMC proposed by Goodman and Weare based on the Metropolis-Hastings algorithm was used to generate the MCMC samples. The parameters of interest to be sampled here are the same as those constrained using the least squares method. Nine parameters were sampled using a sampling code provided by the Pantheon+SH0ES collaboration (run_mcmc.py⁶). Table 3.3 gives some information on how the sampling for all the chains presented below was carried out.

Table 3.3 shows the final configuration under which the MCMC chains were generated.

⁶Avaiable at: <https://github.com/PantheonPlusSH0ES/DataRelease/tree/main>

Parameter	Value/Type	Description
Walkers	1000	Total number of steps in each chain
Chains	10000	Total number of chains in each simulation
Burn-in	6000	Total number of initial chains discarded
Priors	Flat	No prior information was used in the chains

Table 3.3: Sampling configurations used on run_mcmc.py code. It were generated 10000 chains each one with 1000 walkers and, for the total number of chains, the first 6000 chains were eliminated. The convergence was monitored using emcee’s recommended method to estimate the autocorrelation time τ and the burn-in time was set to be 5τ to allow chains to fully converge [2].

The conditions were such that each chain produced a total of 4×10^6 effective samples, that is, after removal of the burn-in phase. The run_mcmc.py script requires only four data files as input: the data vector \mathbf{y} given by the equation (3.17), the matrix \mathbf{L} given by equation (3.18), the data covariance matrix \mathbf{C} (equation (A.1)) and initial values for the vector of fitted parameters given in equation (3.19).

The results of this sampling are presented in Table 3.1, together with the results from the χ^2 analysis and the ones from R22. We can see that the values obtained via MCMC are completely consistent with the results from the χ^2 analysis and the values shown in R22. Posteriors distributions for this real data sample are presented in Figure 3.13. From this figure, it is possible to see that there are no major correlations between the fitted parameters, except in the case $H_0 \times M_B$, which means if the value of M_B changes, the value of H_0 will probably also change.

3.5 Cosmic distance ladder data from R22/Pantheon+

In this section, we deal with a slightly different dataset than the one used in the previous sections. The motivation for introducing these new data comes from the fact that we will test non-standard SNeIa color correction schemes in Chapter 5. This, in turn, requires us to have access to both color and stretch data for these objects, quantities not available in the preformatted SH0ES FITS files used so far. Therefore, we will have to start with the larger Pantheon+ supernova sample and perform some initial selection matching the one done in R22. The new data will consist of a mixture of data from R22 (cepheids and anchors) and Pantheon+ (second and third rung SNe). We shall refer to it from now on as R22/Pantheon+. The following selection criteria had to be applied to the supernovae in the Pantheon+ catalog:

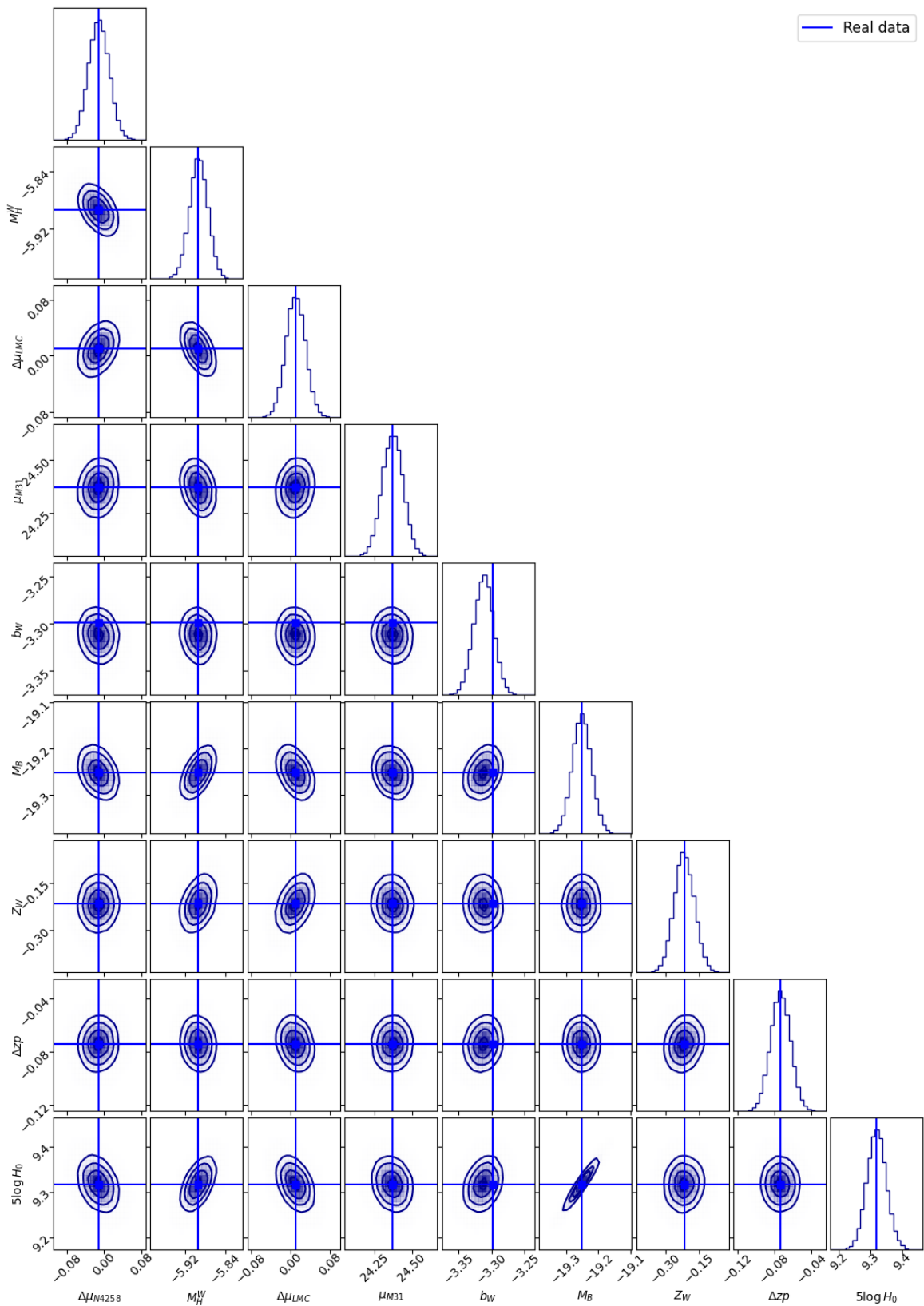


Figure 3.13: Posterior distributions of the model parameters using real data from R22 [31]. The solid lines represent the least squares solution (Table 3.1).

	Original R22 [31]	This work (R22/Pantheon+)
$\Delta\mu_{N4258} \pm \sigma_{\Delta\mu_{N4258}}$	-0.015 ± 0.022	-0.013 ± 0.022
$M_H^W \pm \sigma_{M_H^W}$	-5.897 ± 0.018	-5.894 ± 0.018
$\Delta\mu_{LMC} \pm \sigma_{\Delta\mu_{LMC}}$	0.009 ± 0.019	0.010 ± 0.019
$\mu_{M31} \pm \sigma_{\mu_{M31}}$	24.372 ± 0.069	24.371 ± 0.069
$b_W \pm \sigma_{b_W}$	-3.299 ± 0.015	-3.310 ± 0.015
$M_B \pm \sigma_{M_B}$	-19.238 ± 0.027	-19.248 ± 0.038
$Z_W \pm \sigma_{Z_W}$	-0.206 ± 0.044	-0.217 ± 0.046
$\Delta zp \pm \sigma_{\Delta zp}$	-0.065 ± 0.010	-0.074 ± 0.011
$5 \log_{10}(H_0) \pm \sigma_{5 \log_{10}(H_0)}$	9.318 ± 0.030	9.336 ± 0.039
$H_0 \pm \sigma_{H_0}$	73.04 ± 1.01	73.67 ± 1.31
χ^2/ndof	3548/3446	3548/3446

Table 3.4: Best fit values for 9 of the total 46 distance ladder parameters (see equation (3.19)) obtained through the least squares solution (equation (3.30)). Left: values taken from R22. Right: this work with R22/Pantheon+ data. The average values do not vary much from one analysis to the next, however there is an increase of around 30% in the uncertainties of M_B and H_0 in the R22/Pantheon+ analysis. This is because the Pantheon+ data fluctuates more than the R22 data. It is not yet known why there is this difference in data fluctuations, but in any case, the increase in uncertainties does not interfere with the analysis, since it does not affect the Hubble tension.

- $0.0233 < z < 0.15$;
- $|c| \leq 0.15$;
- $|x_1| < 2$;
- $\sigma_{\mu_0} \leq 0.21$;

where σ_{μ_0} is the uncertainty in the distance modulus of the supernovae. These cuts are adopted here in order to re-obtain the 277 Hubble flow SNe, but they were originally made to have a sample of the Hubble flow SNe with properties similar to those of the calibration sample (i.e. second rung) [31]. The 77 supernovae data from the calibration sample were obtained more directly, since their identifiers are listed in R22 allowing a direct match with the corresponding Pantheon+ objects.

3.5.1 Best fit solution for R22/Pantheon+ data

In order to check whether the selection of supernovae was carried out correctly, a fit was made using their standardized apparent magnitudes (the analysis with uncorrected apparent

magnitudes will only be performed in Chapter 5). In other words, the new data vector consists of apparent magnitudes of cepheids and external parameters from R22 and standardized apparent magnitudes and redshifts of of $77+277=354$ supernovae selected from Pantheon+ according to the cuts described before. In addition, the covariance matrix \mathbf{C} was modified to match the covariances of the supernovae taken from Pantheon+.

The least squares solution for R22/Pantheon+ can be seen in Table 3.4, where a comparison with the original R22 results are also presented. It can be seen that all the fitted parameters are in agreement with the values from the other analyses within the uncertainties. The values of the parameters that do not directly involve supernova data are practically identical to the ones obtained in the reproduction of the R22 fit, as was to be expected, since the cepheid data and external parameters were not altered from one analysis to the next. In addition, small variations are observed in the parameters related to supernova data, such as the absolute magnitude of supernovae and the Hubble constant, which not only had their average values increased but also their uncertainties.

The histograms of residual of the new supernova data from the second and third rungs are shown in Figure 3.14. It can be seen that both are centered approximately at zero and that their widths do not vary so much with respect to those based on R22 data (Figure 3.12), which indicates that the selection of supernova data made in the Pantheon+ catalog can be trusted.

Distance modulus versus redshift diagrams for the selected Pantheon+ third rung supernovae are presented in Figure 3.15, together with two theoretical curves, both following equa-

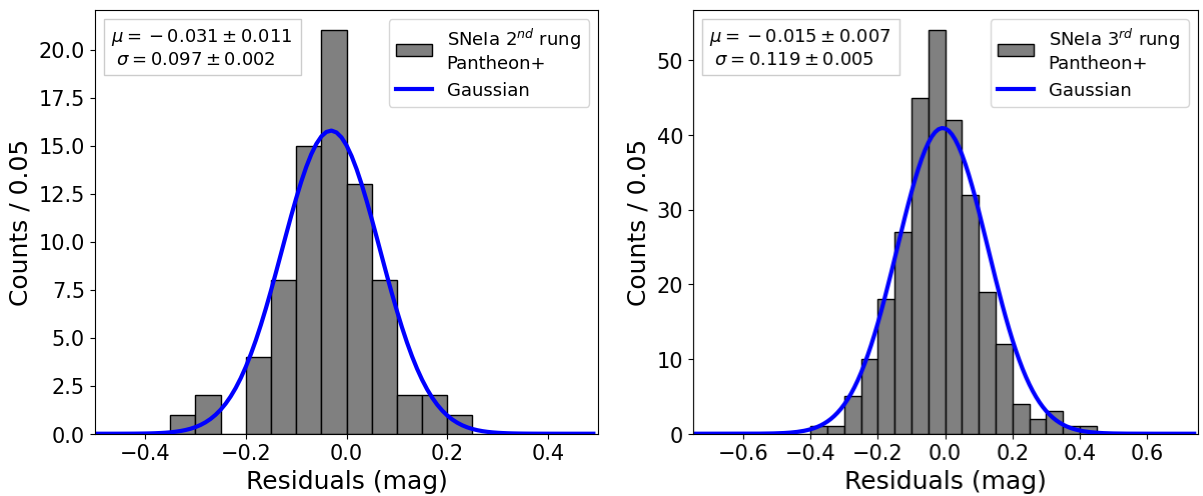


Figure 3.14: Histograms of the real data of the second and third rung SNIa obtained from Pantheon+. Here residuals means (data-theory), furthermore, the mean value (μ) and the variance (σ) of these histograms were obtained by maximum likelihood estimation.

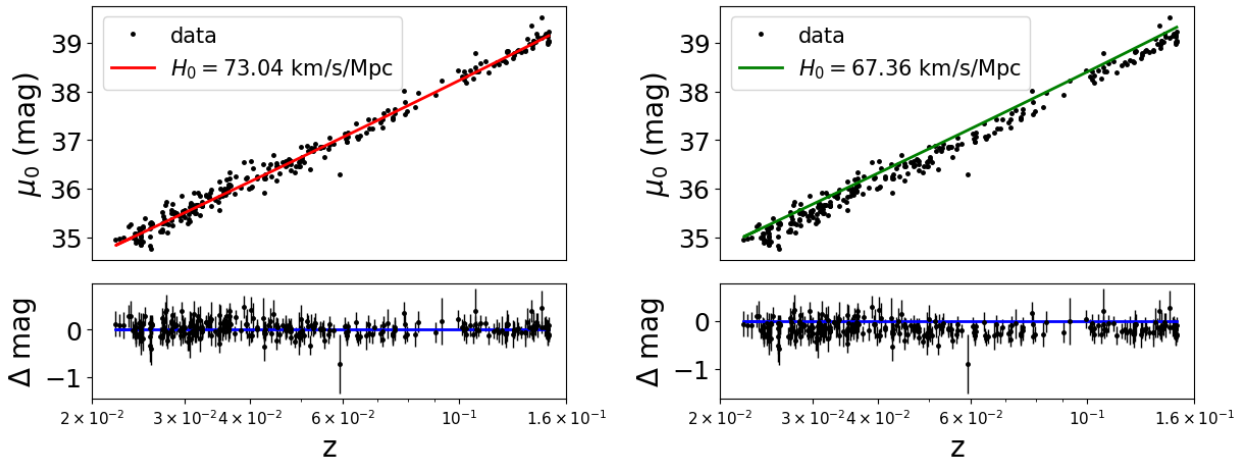


Figure 3.15: The plots on the top represent the distance modulus data μ_0 as a function of the redshift z of the supernovae and two theoretical predictions of $\mu_0(z)$, one considering $H_0 = 67.36$ km s⁻¹ Mpc⁻¹ (in green) and another considering $H_0 = 73.04$ km s⁻¹ Mpc⁻¹ (in red). Residuals (Δmag) are shown below each $\mu_0 \times z$ plot, on the left considering the value of H_0 obtained from supernova measurements and, on the right, considering the value of the Hubble constant obtained via CMB.

tion (3.15) with $q_0 = -0.55$, $j_0 = 1$ and the other parameters of the model fixed at the values given in Table 3.4. The red curve was calculated using $H_0 = 73.04$ km s⁻¹ Mpc⁻¹, which is the value obtained via SNeIa and, the green curve was calculated with $H_0 = 67.36$ km s⁻¹ Mpc⁻¹, estimate from CMB measurements. Residuals between the data points and the theoretical curves are shown at the bottom of both $\mu_0 \times z$ diagrams. Residuals on the left are calculated

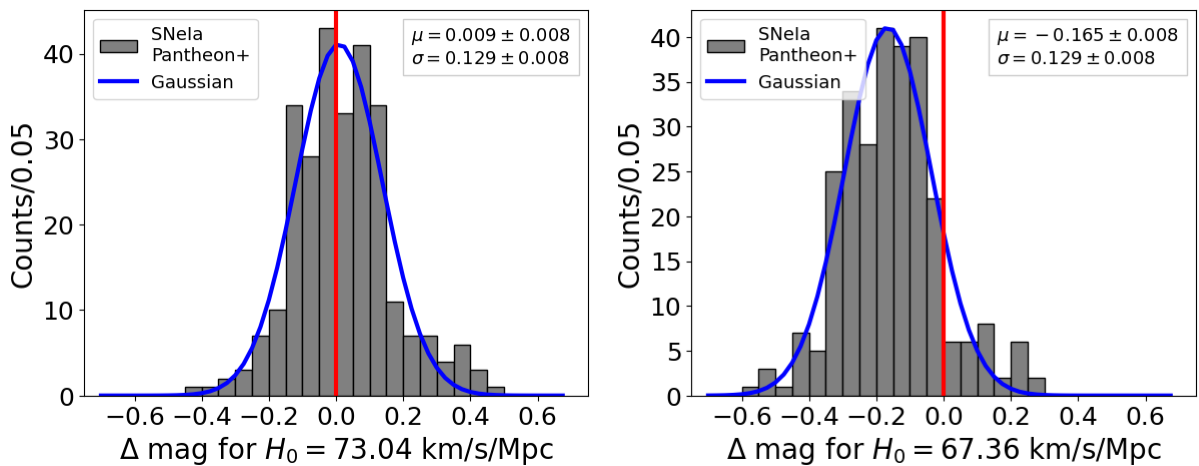


Figure 3.16: Histograms of Δmag considering $H_0 = 73.04$ km s⁻¹ Mpc⁻¹ (left graph) and $H_0 = 67.36$ km s⁻¹ Mpc⁻¹ (right graph). Gaussian fits were performed to the histograms (blue curves) and their mean and standard deviations are also shown in the plots.

with respect to a SN-compatible Hubble constant model (solid red curve), whereas the one on the right is given with respect to a CMB-compatible Hubble constant model (solid green curve). By construction, the values of Δmag in the left plot fluctuate around 0, while the values of Δmag on the right plot scatter around a value below 0. The peculiar velocity of the selected supernovae were estimated (1) replacing SN-host redshifts with their host-galaxy group redshift (when available), and (2) using local density maps to account for motions induced by local gravity [31, 99].

Figure 3.16 shows the histograms of Δmag considering $H_0 = 73.04 \text{ km s}^{-1} \text{ Mpc}^{-1}$ (on the left) and $H_0 = 67.36 \text{ km s}^{-1} \text{ Mpc}^{-1}$ (on the right). Two Gaussians were fitted to these histograms, the one on the left centered approximately at 0 mag and the one on the right centered at -0.165 mag, both with a width of 0.129 mag. This means that if the distance modulus values of all the supernovae used for the H_0 estimate are increased by 0.165 mag, it is possible to obtain an estimate of the Hubble constant with supernova that matches the value estimated using the CMB data.

Under the hypothesis that the correct estimate of H_0 is coming from the CMB measurements, the misplacement of the residuals seen in Figures 3.15 and 3.16 could be explained, for example, by a systematic error on the apparent magnitudes of SNeIa of the third rung. This is one of the hypotheses to be further explored in Chapters 4 and 5. As will be seen in these chapters, a systematic error inserted in the data of the third rung does not impact the other rungs of the distance ladder, which makes the analysis even more interesting, since parameters not directly related to supernovae in the Hubble flow are protected against these biases.

4 | Response of the distance ladder to systematic errors

In this chapter, different analyses with systematic deviations are performed in order to understand and quantify their propagation through the cosmic distance ladder to the fitted model parameters. The study will be performed using synthetic data samples generated and stored in a FITS format identical to real data. Moreover, their covariance will match perfectly that of the real data (full covariance matrix case), but at the end of the chapter, we will also investigate the impact of neglecting correlations present in the input data.

4.1 Full covariance matrix

We present here analyses similar to that of section [3.4.1](#), using synthetic samples affected by different biases. As mentioned before, the statistical uncertainties in the parameters of interest will be taken as the reference scale to measure the magnitude of the systematic errors to be introduced in the simulated sample.

The unbiased synthetic data vector \mathbf{y}_{syn} was generated according to:

$$\mathbf{y}_{\text{syn}} = \mathbf{L}\mathbf{q}_{\text{best}} + \mathbf{x}, \quad (4.1)$$

where \mathbf{L} is given by equation [\(3.18\)](#) and \mathbf{q}_{best} contains the true model parameters forced to be equal to the central values of the parameters on the third column of Table [3.1](#), except the distance moduli of SNeIa - cepheid hosts, which are not present in this table but can be found on GitHub¹. \mathbf{x} is a vector of N (zero mean and covariance \mathbf{C} , given by equation [\(A.1\)](#)) Gaussian random variables with probability distribution functions given by:

$$p(\mathbf{x}) = \frac{1}{(2\pi)^{N/2}(\det \mathbf{C})^{1/2}} \exp \left[-\frac{1}{2} \mathbf{x}^T \mathbf{C}^{-1} \mathbf{x} \right]. \quad (4.2)$$

The standard deviations shown in Table [3.2](#) are considered to be the reference scale for the systematic shifts (Δ_{sys}) to be added to the analysis from now on. We start by studying

¹https://github.com/PantheonPlusSH0ES/DataRelease/tree/main/SH0ES_Data

$\Delta_{\text{sys}}/\sigma_{\text{stat}}$	$H_0 \pm \sigma_{H_0}$ (km s ⁻¹ Mpc ⁻¹)	$M_B \pm \sigma_{M_B}$ (mag)
-5	57.48 ± 0.79	-19.758 ± 0.029
-4	61.55 ± 0.85	-19.636 ± 0.029
-3	63.85 ± 0.88	-19.535 ± 0.029
-2	66.05 ± 0.91	-19.463 ± 0.029
-1	68.13 ± 0.94	-19.398 ± 0.029
0	73.37 ± 1.01	-19.242 ± 0.029
1	76.62 ± 1.06	-19.147 ± 0.029
2	80.87 ± 1.12	-19.024 ± 0.029
3	83.90 ± 1.16	-18.930 ± 0.029
4	88.83 ± 1.22	-18.829 ± 0.029
5	92.32 ± 1.27	-18.734 ± 0.029

Table 4.1: Least squares solutions for the Hubble constant and SNIa absolute magnitude using synthetic data affected by systematic shifts on the apparent magnitudes of second rung SNIa with different magnitudes Δ_{sys} , in units of $\sigma_{\text{stat}} = 0.098$ mag.

the response of the distance ladder to biases on the synthetic apparent magnitudes of second rung supernovae:

$$m_B \rightarrow m_B + \Delta_{\text{sys}}. \quad (4.3)$$

According to Table 3.2, the reference scale in this case is $\sigma_{\text{stat}} = 0.098$ mag. Table 4.1 and Figure 4.1 show the values of H_0 and M_B as a function of $\Delta_{\text{sys}}/\sigma_{\text{stat}}$. It can be seen that both H_0 and M_B increase with $\Delta_{\text{sys}}/\sigma_{\text{stat}}$.

As can be seen from equation (3.22), the data in the third block of \mathbf{y} (i.e., second rung

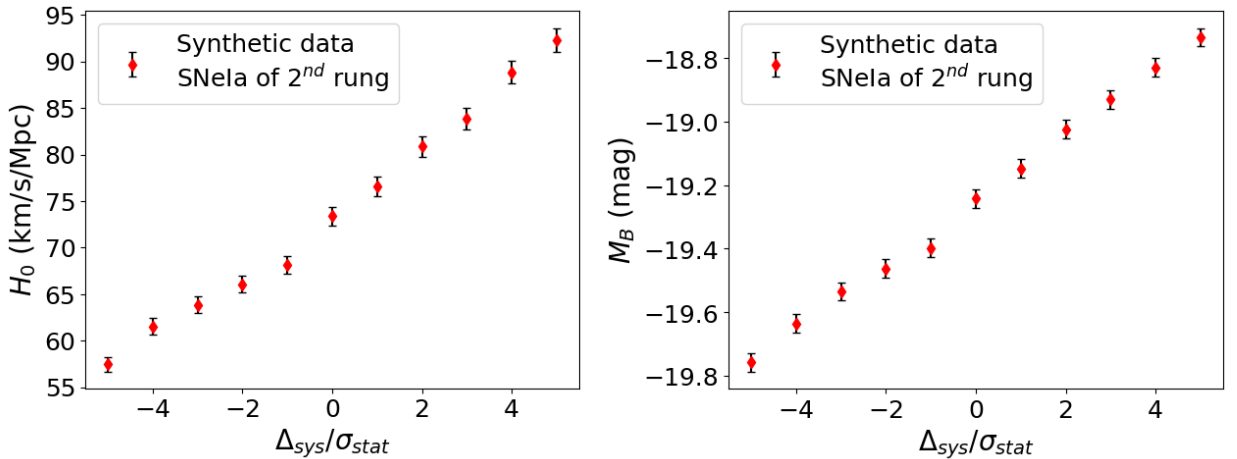


Figure 4.1: H_0 and M_B as a function of the magnitude of a hypothetical bias on the apparent magnitudes of 2nd rung synthetic SNIa. The systematic errors are given in units of the statistical fluctuation $\sigma_{\text{stat}} = 0.098$ mag.

$\Delta_{\text{sys}}/\sigma_{\text{stat}}$	$H_0 \pm \sigma_{H_0}$ (km s ⁻¹ Mpc ⁻¹)	$M_B \pm \sigma_{M_B}$ (mag)
-5	101.83 ± 1.40	-19.198 ± 0.029
-4	94.50 ± 1.30	-19.238 ± 0.029
-3	88.65 ± 1.22	-19.232 ± 0.029
-2	83.11 ± 1.15	-19.236 ± 0.029
-1	78.73 ± 1.09	-19.215 ± 0.029
0	72.15 ± 0.99	-19.290 ± 0.029
1	68.03 ± 0.94	-19.272 ± 0.029
2	64.52 ± 0.89	-19.246 ± 0.029
3	60.75 ± 0.84	-19.236 ± 0.029
4	57.49 ± 0.79	-19.232 ± 0.029
5	54.43 ± 0.75	-19.202 ± 0.029

Table 4.2: Least squares solutions for the Hubble constant and SNIa absolute magnitude using synthetic data affected by systematic shifts on data of third rung SNIa with different magnitudes Δ_{sys} , in units of $\sigma_{\text{stat}} = 0.135$ mag.

SNIa) depends on M_B and μ_0 . Therefore, a uniform (i.e., host independent) systematic shift on the apparent magnitudes of second rung SNIa, immediately bias the fitted absolute magnitude M_B of these objects. On the other hand, since the third rung (the Hubble flow SNIa) data is still unbiased, equation (3.28) shows that the M_B bias should be compensated by a corresponding shift on H_0 . Table B.1 and Figure B.1 in Appendix B show the values of all the fitted parameters as a function of $\Delta_{\text{sys}}/\sigma_{\text{stat}}$ and the respective posterior distributions for the case where $\Delta_{\text{sys}} = \sigma_{\text{stat}}$ are presented in Figure 4.6.

Once the systematic deviations had been inserted into the synthetic apparent magnitude

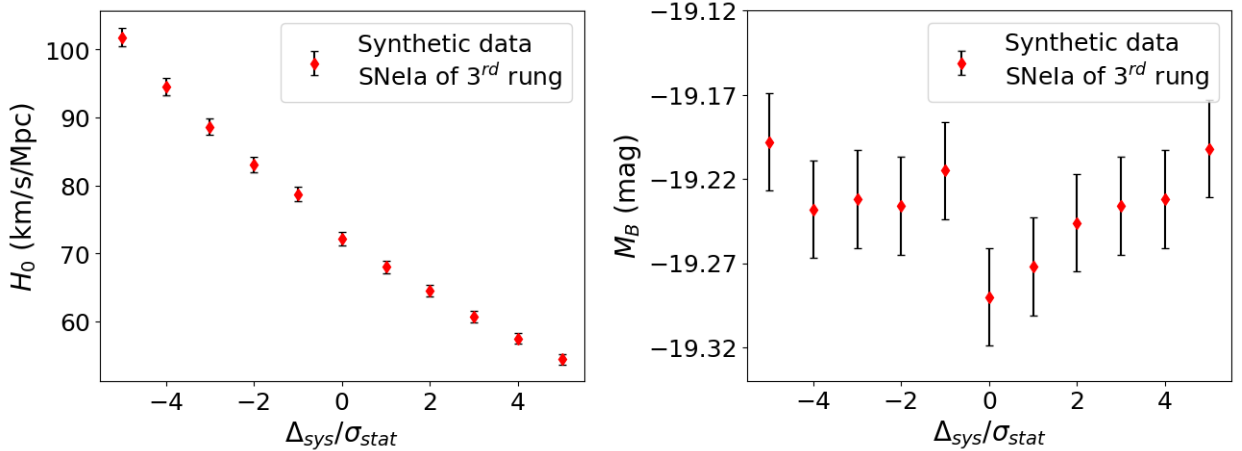


Figure 4.2: H_0 and M_B as a function of the magnitude of a hypothetical bias on the apparent magnitudes of 3rd rung synthetic SNIa. The systematic errors are given in units of the statistical fluctuation $\sigma_{\text{stat}} = 0.135$ mag.

$\Delta_{\text{sys}}/\sigma_{\text{stat}}$	$H_0 \pm \sigma_{H_0}$ (km s ⁻¹ Mpc ⁻¹)	$M_B \pm \sigma_{M_B}$ (mag)
-5	79.82 ± 1.10	-19.722 ± 0.029
-4	78.12 ± 1.08	-19.646 ± 0.029
-3	77.15 ± 1.06	-19.523 ± 0.029
-2	76.28 ± 1.05	-19.419 ± 0.029
-1	75.06 ± 1.03	-19.326 ± 0.029
0	73.03 ± 1.01	-19.253 ± 0.029
1	72.52 ± 1.00	-19.120 ± 0.029
2	71.29 ± 0.98	-19.025 ± 0.029
3	69.19 ± 0.95	-18.968 ± 0.029
4	68.54 ± 0.95	-18.844 ± 0.029
5	66.86 ± 0.92	-18.769 ± 0.029

Table 4.3: Least squares solutions for the Hubble constant and SNIa absolute magnitude using synthetic data affected by systematic shifts on data of the second and third rung SNeIa with different magnitudes Δ_{sys} , in units of $\sigma_{\text{stat}} = 0.098$ mag and $\sigma_{\text{stat}} = 0.135$ mag, respectively.

data of the SNeIa of the second rung, the same procedure was carried out with the synthetic data of the third rung supernovae. These data are not exactly apparent magnitudes, but rather a combination of apparent magnitude and redshift (see equation (3.28)):

$$m_B - 5 \log_{10}\{\dots\} - 25 \rightarrow m_B - 5 \log_{10}\{\dots\} - 25 + \Delta_{\text{sys}}. \quad (4.4)$$

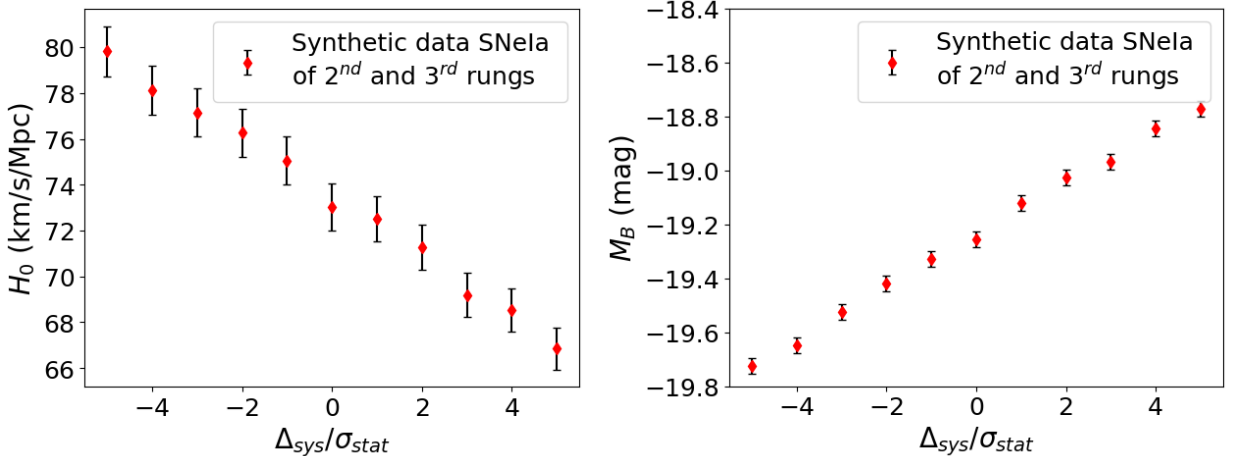


Figure 4.3: H_0 and M_B as a function of the magnitude of a hypothetical bias affecting the apparent magnitudes of 2nd and 3rd rung synthetic SNeIa, simultaneously. The systematic errors are given in units of the statistical fluctuations $\sigma_{\text{stat}} = 0.098$ mag and $\sigma_{\text{stat}} = 0.135$, respectively.

According to Table 3.2, the reference scale is now $\sigma_{\text{stat}} = 0.135$ mag and the values of the

$\Delta_{\text{sys}}/\sigma_{\text{stat}}$	$H_0 \pm \sigma_{H_0}$ (km s ⁻¹ Mpc ⁻¹)	$M_B \pm \sigma_{M_B}$ (mag)
-5	73.77 ± 1.02	-19.962 ± 0.029
-4	73.56 ± 1.01	-19.833 ± 0.029
-3	72.76 ± 1.00	-19.697 ± 0.029
-2	73.25 ± 1.01	-19.545 ± 0.029
-1	73.13 ± 1.01	-19.390 ± 0.029
0	72.98 ± 1.01	-19.252 ± 0.029
1	73.81 ± 1.02	-19.072 ± 0.029
2	73.15 ± 1.01	-18.955 ± 0.029
3	73.18 ± 1.01	-18.787 ± 0.029
4	73.36 ± 1.01	-18.636 ± 0.029
5	73.93 ± 1.02	-18.485 ± 0.029

Table 4.4: Least squares solutions for the Hubble constant and SNIa absolute magnitude using synthetic data affected by systematic shifts on data of the second and third rung SNIa with different magnitudes Δ_{sys} , in units of $\sigma_{\text{stat}} = 0.15$ mag.

analyzed parameters as a function of $\Delta_{\text{sys}}/\sigma_{\text{stat}}$ are shown in Table 4.2 and Figure 4.2. This figure shows that H_0 decreases as $\Delta_{\text{sys}}/\sigma_{\text{stat}}$ rises whereas M_B remains stable with respect to this particular bias. The behavior of these two variables can be understood by noticing that the unbiased second rung data is responsible for constraining M_B around its true value, leaving H_0 alone to absorb the uniform (i.e., redshift independent) bias of the third rung data. Table B.2 and Figure B.2 in Appendix B show the values of all the fitted parameters as a function of $\Delta_{\text{sys}}/\sigma_{\text{stat}}$ and the respective posterior distributions for $\Delta_{\text{sys}} = \sigma_{\text{stat}}$ are presented in Figure 4.7.

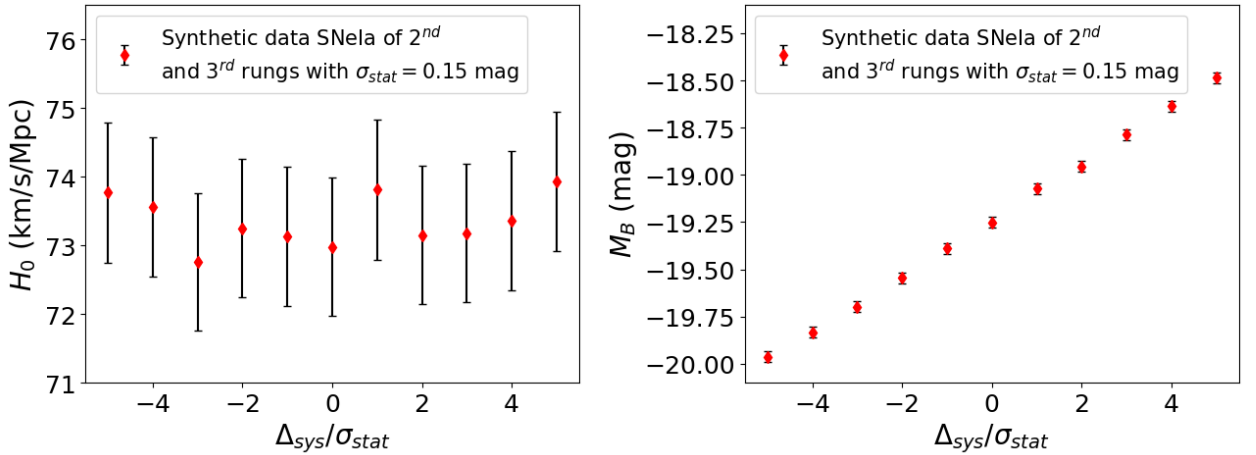


Figure 4.4: H_0 and M_B as a function of the magnitude of a hypothetical uniform bias affecting the apparent magnitudes of 2nd and 3rd rung synthetic SNIa, simultaneously. The systematic errors are given in units of the statistical fluctuation $\sigma_{\text{stat}} = 0.15$ mag.

$\Delta_{\text{sys}}/\sigma_{\text{stat}}$	$H_0 \pm \sigma_{H_0}$ ($\text{km s}^{-1} \text{Mpc}^{-1}$)	$M_H^W \pm \sigma_{M_H^W}$ (mag)	$b_W \pm \sigma_{b_W}$ (mag/dex)	$Z_W \pm \sigma_{Z_W}$ (mag/dex)
-10^4	73.64 ± 1.15	-5.872 ± 0.024	-3.307 ± 0.015	$-(2.3 \pm 6.7) \times 10^{-5}$
-10^3	72.63 ± 1.13	-5.923 ± 0.024	-3.293 ± 0.015	$-(7.4 \pm 6.6) \times 10^{-4}$
-10^2	73.64 ± 1.13	-5.885 ± 0.024	-3.306 ± 0.015	-0.013 ± 0.006
-10	73.65 ± 1.04	-5.919 ± 0.021	-3.297 ± 0.015	-0.157 ± 0.032
0	73.46 ± 1.01	-5.901 ± 0.018	-3.306 ± 0.015	-0.245 ± 0.045
10	72.32 ± 1.07	-5.857 ± 0.018	-3.288 ± 0.015	-0.138 ± 0.047
10^2	73.44 ± 1.16	-5.905 ± 0.024	-3.317 ± 0.015	0.008 ± 0.007
10^3	73.59 ± 1.15	-5.889 ± 0.024	-3.288 ± 0.015	$(4.9 \pm 6.8) \times 10^{-4}$
10^4	73.52 ± 1.15	-5.881 ± 0.024	-3.308 ± 0.015	$(7.2 \pm 6.7) \times 10^{-5}$

Table 4.5: Least squares solutions for the Hubble constant, the absolute magnitude for cepheids, the coefficient related to the period correction and the coefficient related to the metallicity correction using the metallicity data affected by systematic shifts with different magnitudes Δ_{sys} , in units of $\sigma_{\text{stat}} = 0.05$ dex.

Next, systematic shifts were inserted into the synthetic data of the second and third rung supernovae, simultaneously, using the reference scales previously discussed, that is, $\sigma_{\text{stat}} = 0.098$ mag and $\sigma_{\text{stat}} = 0.135$ mag, respectively. The least squares best-fit results for H_0 and M_B can be seen in Table 4.3 and Figure 4.3. We can see from Figure 4.3 that both the Hubble constant and the SNIa absolute magnitude are affected now. The bias on M_B comes mainly from the corresponding bias on the second rung data as before. However, now the third rung data is also biased, but since the magnitudes of the biases are different in the two rungs, M_B is not able to absorb completely the systematic shift of the data. Therefore, the bias ends up leaking partially to H_0 . In order to prove that the bias on H_0 is residual in this case and due to the mismatch between the systematic reference scales of the second and third rungs, we have forced a uniform scale on both rungs ($\sigma_{\text{stat}} = 0.15$ mag) and verified that H_0 stays protected against the bias, with M_B fully absorbing the systematic shift, as can be seen in Figure 4.4 and Table 4.4. Tables B.3 and B.4 and Figures B.3 and B.4 in Appendix B show the values and dependencies on $\Delta_{\text{sys}}/\sigma_{\text{stat}}$ of all fitted parameters, respectively, whereas Figures 4.8 and 4.9 show the respective posterior distributions, again for the $\Delta_{\text{sys}} = \sigma_{\text{stat}}$ case.

So far, we have explored the impact of systematic effects on variables of the second and third rungs intrinsically related to the SNIa. Given the structure of the ladder and the $M_B \times H_0$ correlations that can be clearly seen in all the posterior distributions shown so far, these were the most natural places along the ladder to start with. Next, we investigated the stability of the distance ladder to biases on the metallicities of cepheids (which for the R22

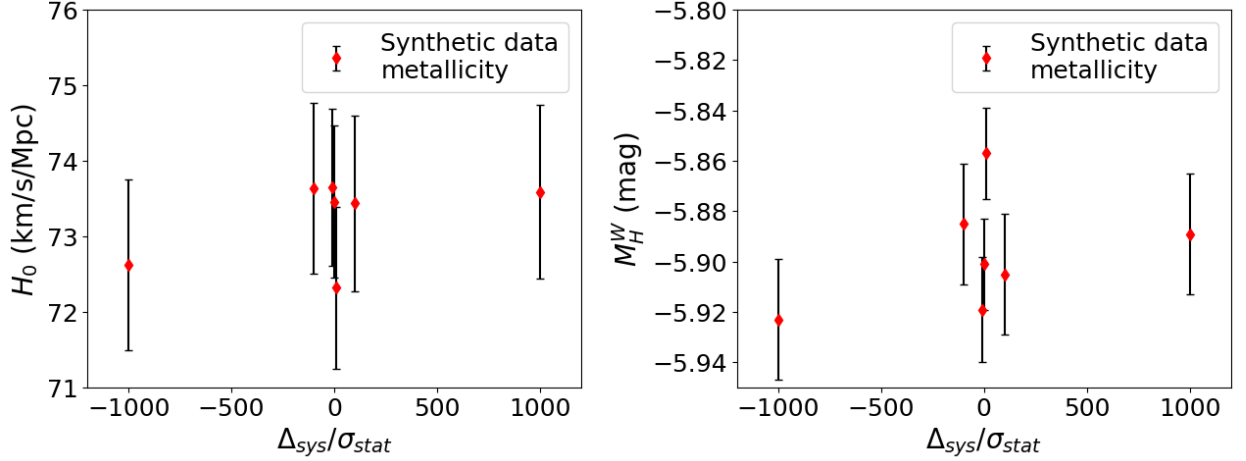


Figure 4.5: H_0 and M_H^W as a function of the magnitude of a hypothetical uniform bias affecting the metallicities of synthetic cepheids. The systematic errors are given in units of the statistical fluctuation $\sigma_{\text{stat}} = 0.05$ dex.

distance ladder, represent external parameters used to build the matrix \mathbf{L}):

$$[\text{O}/\text{H}] \rightarrow [\text{O}/\text{H}] + \Delta_{\text{sys}}. \quad (4.5)$$

For metallicities, the reference scale for the systematic shift was taken as $\sigma_{\text{stat}} = 0.05$ dex, the typical statistical uncertainty on cepheid metallicities in R22 [31]. The results of the fits for each Δ_{sys} are given in Table 4.5 and Figure 4.5. As can be seen from Table 4.5, we have scanned the systematic shift Δ_{sys} over eight orders of magnitude, which should certainly exceed any physically motivated bias on this quantity. Figure B.5 shows the behavior of H_0 and M_H^W as a function of $\Delta_{\text{sys}}/\sigma_{\text{stat}}$. From Table 4.5 it is possible to see that no parameter other than Z_W is affected by the variation in $\Delta_{\text{sys}}/\sigma_{\text{stat}}$. As Z_W is the parameter responsible for the metallicity correction in the apparent magnitude of the cepheids, see equation (3.12), it was expected that this parameter would be affected by changes in the synthetic apparent magnitudes. The stability of the Hubble constant and of the absolute magnitude of cepheids M_H^W under metallicity biases is, in any case, impressive. This is a very nice feature of the R22 ladder structure, that is: Hubble flow-related (H_0), SNIa- (M_B) and cepheid-intrinsic parameters (M_H^W , b_W and μ_0 's) are strongly protected against cepheid metallicity biases. Table B.5 and Figure B.5 in Appendix B show the values of all the fitted parameters and their behavior as a function of $\Delta_{\text{sys}}/\sigma_{\text{stat}}$, in addition, the respective posterior distributions are presented in Figure 4.10, now for the case $\Delta_{\text{sys}} = 5\sigma_{\text{stat}}$.

4.2 The role of data correlations

	True values	Analysis with a complete matrix	Analysis with a diagonal matrix
$\Delta\mu_{N4258} \pm \sigma_{\Delta\mu_{N4258}}$	-0.015	-0.025 ± 0.022	0.005 ± 0.020
$M_H^W \pm \sigma_{M_H^W}$	-5.897	-5.864 ± 0.018	-5.902 ± 0.017
$\Delta\mu_{LMC} \pm \sigma_{\Delta\mu_{LMC}}$	0.009	0.005 ± 0.019	0.010 ± 0.017
$\mu_{M31} \pm \sigma_{\mu_{M31}}$	24.372	24.280 ± 0.069	24.379 ± 0.024
$b_W \pm \sigma_{b_W}$	-3.299	-3.324 ± 0.015	-3.384 ± 0.015
$M_B \pm \sigma_{M_B}$	-19.238	-19.238 ± 0.029	-19.248 ± 0.025
$Z_W \pm \sigma_{Z_W}$	-0.206	-0.148 ± 0.045	-0.201 ± 0.028
$\Delta zp \pm \sigma_{\Delta zp}$	-0.074	-0.010 ± 0.011	-0.005 ± 0.011
$5 \log_{10}(H_0) \pm \sigma_{5 \log_{10}(H_0)}$	9.318	9.319 ± 0.030	9.312 ± 0.026
$H_0 \pm \sigma_{H_0}$	73.04	73.08 ± 1.01	72.84 ± 0.88
χ^2/ndof	-	3720/3446	3376/3446

Table 4.6: Least squares best-fit values for the R22 cosmic ladder parameters using synthetic data. The table shows the true values of the parameters, that is, those used during the generation of the sample. Fits using the full covariance of the synthetic data and a simplified diagonal covariance matrix are also shown.

In this section we study the impact of neglecting correlations we know are present in the real dataset. These correlations are explicit in the form of the covariance matrix (see Appendix A). More precisely, we perform, in a controlled situation, fits to synthetic data where a mismatch between data generation and data fit covariance matrices is introduced. Here, data generation will always be performed using the full (non-diagonal) covariance matrix, whereas the fit will be performed either with the full or with a simplified (diagonal) version of the covariance matrix.

Comparing the values of the fitted parameters for the two cases in Table 4.6, it can be seen that there is no significant bias introduced when the simplified version of the covariance matrix is used. Nonetheless, the uncertainties on some parameters become underestimated in this case and that is an important point for anyone looking for solutions to the Hubble tension.

A recent paper, Riess et al. (2023) [100], investigated the impact of systematic errors associated with cepheid measurements obtained with the HST using measurements from the James Webb Space Telescope (JWST). The high-resolution JWST observations can test the HST observations to detect a photometric bias that could affect extragalactic cepheids and the determination of the Hubble constant. The JWST provides a much better separation of

the observed objects than the HST in the near infrared, so that it largely cancels out the clutter noise at these wavelengths, where extinction is minimal. Through this work it was possible to verify that the P-L diagram and the H_0 determined with this new calibration are in agreement with the HST data and the main conclusion is that the systematic errors in the photometry of the HST cepheids do not play a significant role in the current Hubble tension. Forthcoming JWST observations of SNeIa hosts should further refine the local measurement of the Hubble constant.

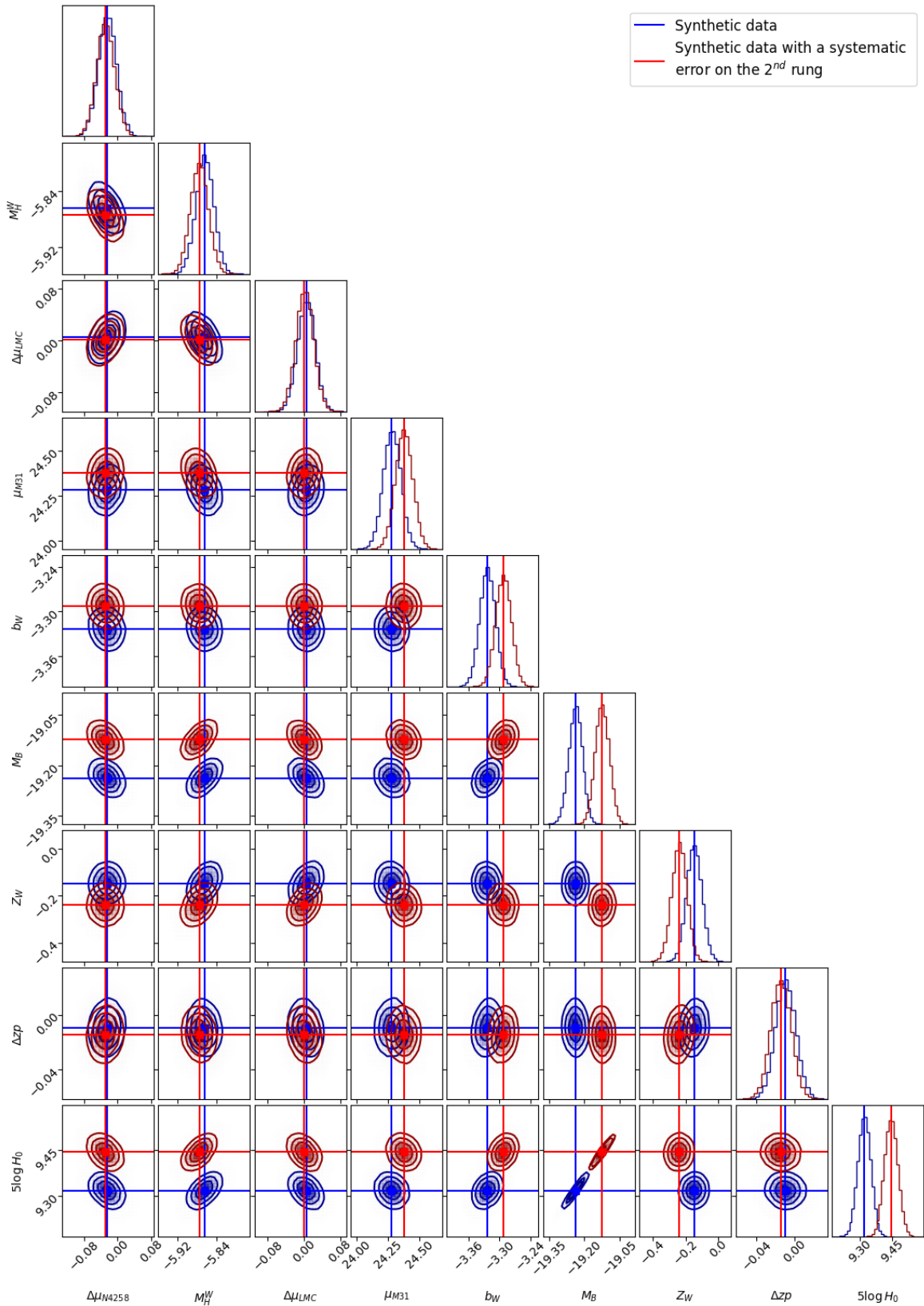


Figure 4.6: Corner plots showing the posterior distributions of nine parameters of the cosmic distance ladder for synthetic data samples. Blue: synthetic sample not affected by systematic errors. Red: apparent magnitudes of the 2nd rung supernovae were biased by $\Delta_{\text{sys}} = 0.098$ mag. For comparison, the corresponding least-squares best-fit solutions are shown as solid red and blue lines.

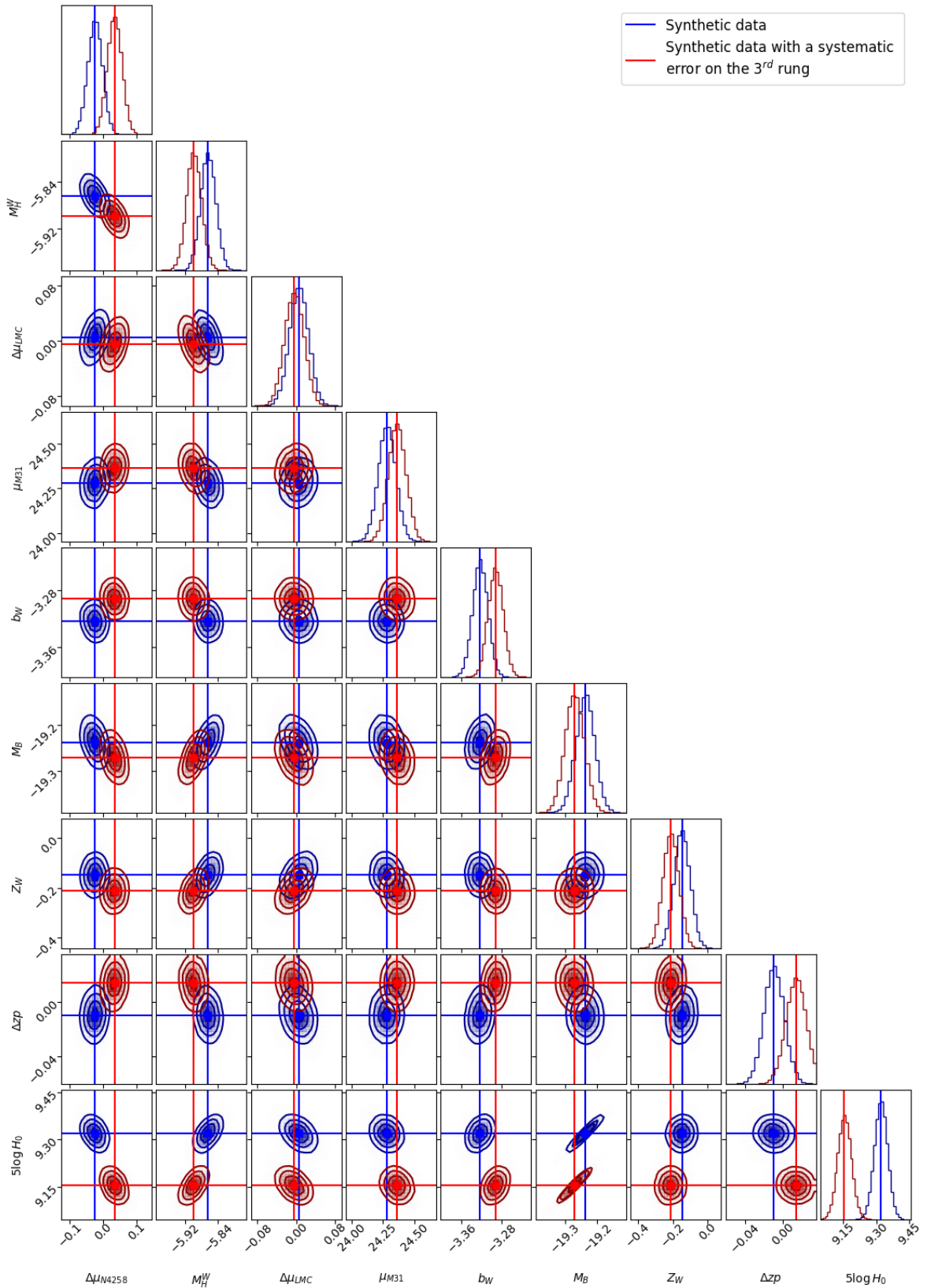


Figure 4.7: Corner plots showing the posterior distributions of nine parameters of the cosmic distance ladder for synthetic data samples. Blue: synthetic sample not affected by systematic errors. Red: apparent magnitudes of the 3rd rung supernovae were biased by $\Delta_{\text{sys}} = 0.135$ mag. For comparison, the corresponding least-squares best-fit solutions are shown as solid red and blue lines.

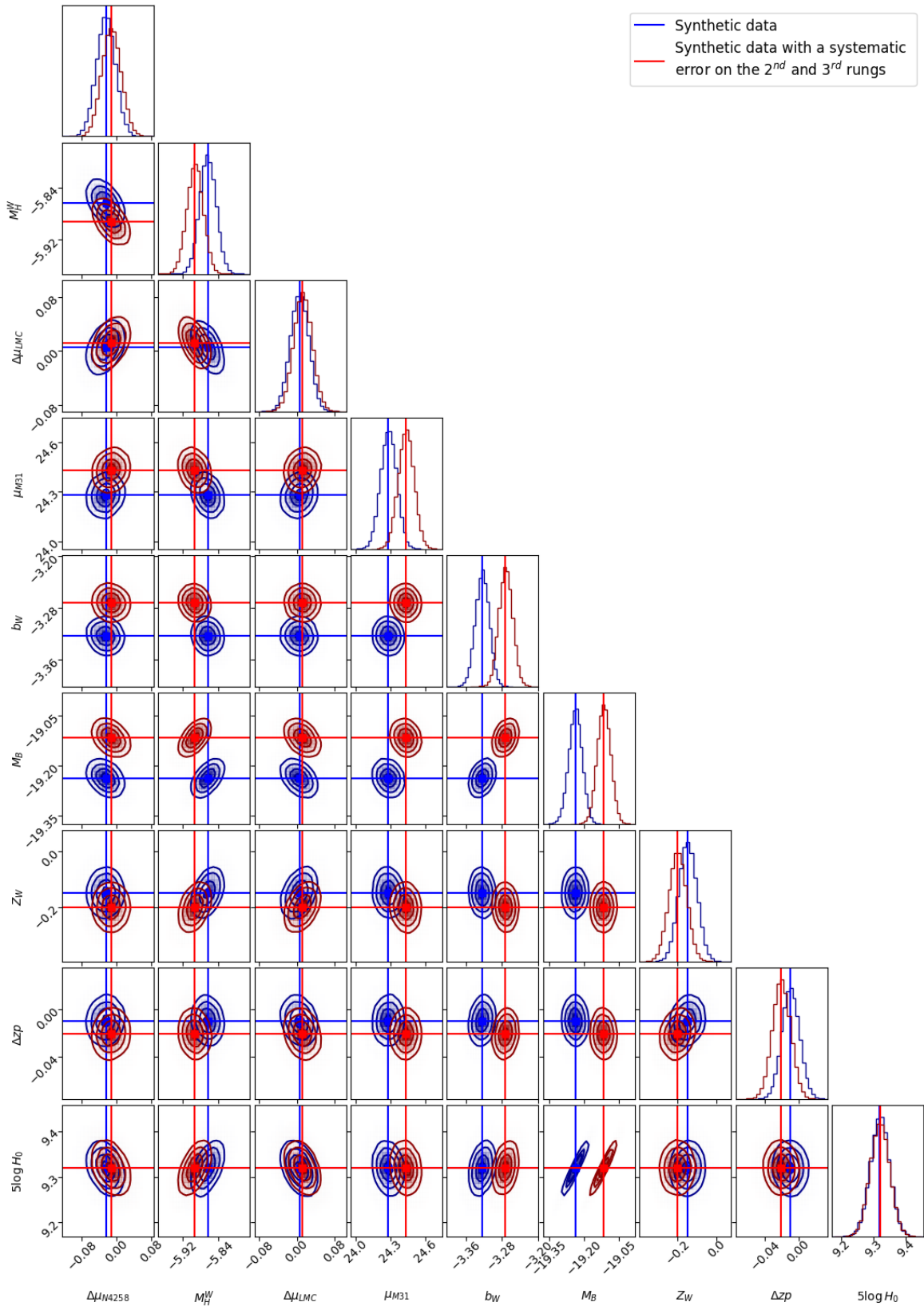


Figure 4.8: Corner plots showing the posterior distributions of nine parameters of the cosmic distance ladder for synthetic data samples. Blue: synthetic sample not affected by systematic errors. Red: apparent magnitudes of the 2nd and 3rd rung supernovae were biased by $\Delta_{\text{sys}} = 0.098$ mag and $\Delta_{\text{sys}} = 0.135$ mag, respectively. For comparison, the corresponding least-squares best-fit solutions are shown as solid red and blue lines.

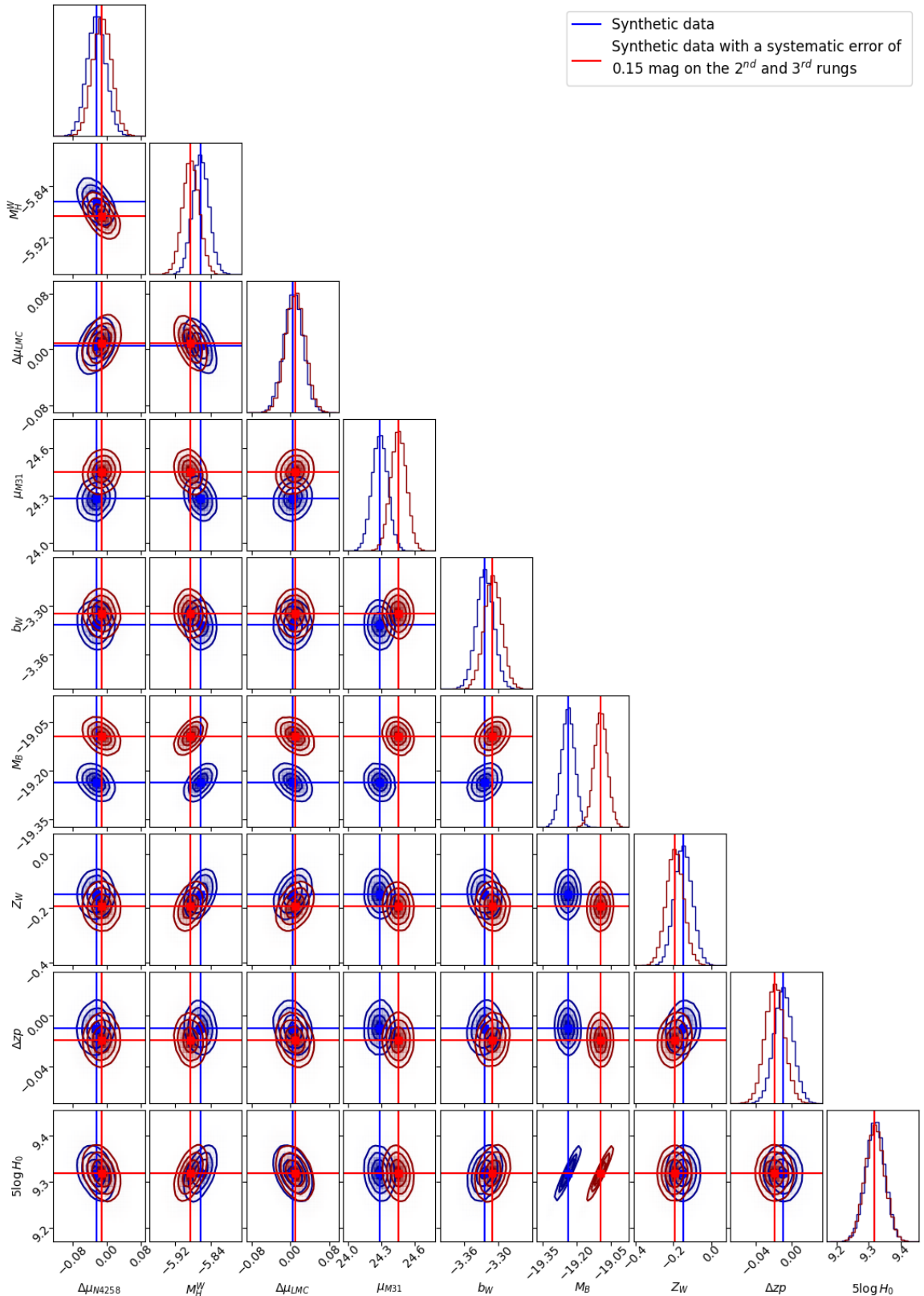


Figure 4.9: Corner plots showing the posterior distributions of nine parameters of the cosmic distance ladder for synthetic data samples. Blue: synthetic sample not affected by systematic errors. Red: apparent magnitudes of the 2nd and 3rd rung supernovae were biased by $\Delta_{\text{sys}} = 0.15$ mag. For comparison, the corresponding least-squares best-fit solutions are shown as solid red and blue lines.

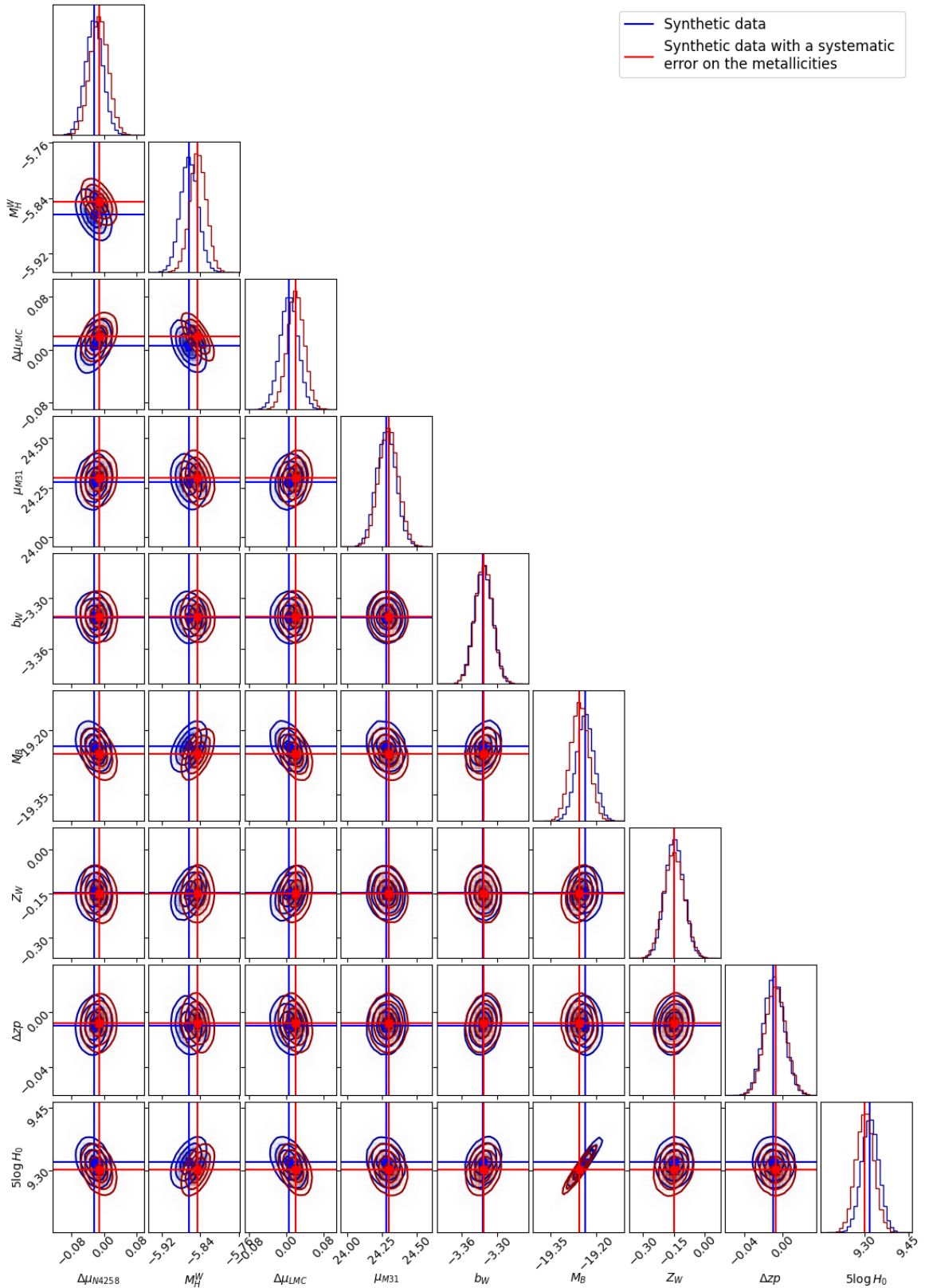


Figure 4.10: Corner plots showing the posterior distributions of nine parameters of the cosmic distance ladder for synthetic data samples. Blue: synthetic sample not affected by systematic errors. Red: metallicity data of cepheids were biased by $\Delta_{\text{sys}} = 0.25$ dex. For comparison, the corresponding least-squares best-fit solutions are shown as solid red and blue lines.

5 | Cosmic distance ladder with different models of color correction

In this chapter, we will deal with the problem of quantifying the impact on the cosmic distance ladder fit of assumptions made during the process of standardization of SNeIa regarding color and stretch data. We follow indications presented in [101], suggesting that the inclusion of a reference color on the SNeIa data when calibration (second rung) and Hubble flow (third rung) objects have different color slopes, can have a significant impact on the Hubble constant.

As discussed in Chapter 3, in order to test alternative color correction models, we had to extract color values directly from the Pantheon+ GitHub repository. Therefore, throughout this chapter, the dataset will be a mixture of the previously used SH0ES FITS files containing cepheids, anchors, and external constraints data with a custom-made selection (based on cuts from Riess et al. (2002), presented and validated in section 3.5.1) of SNeIa data from Pantheon+.

The data for the selected supernovae (red) are presented in Figure 5.1 along with those for all supernovae in Pantheon+ (black) in the form of a distance modulus versus redshift diagram. Also in Figure 5.1, the color of the selected supernovae are plotted as a function of their redshifts. For the color data, black represents supernovae in the calibration sample (second rung), whereas red is associated to supernovae in the Hubble flow (third rung). The average value of the color for both samples is also shown as dotted horizontal lines in the plot. We can see a color step $\Delta c = c^{3rd} - c^{2nd} = -0.034 \pm 0.010$ between them, that is, on average, the selected SNIa Hubble flow sample is slightly redder, but we also mention that this is likely to be a selection effect (due to the selection criteria applied to supernovae in the Hubble flow, presented in section 3.5) rather than a genuine physical property of the objects.

In addition, Figure 5.2 shows uncorrected apparent magnitude as a function of color for all the selected supernovae. The blue dots represent the calibration sample and the black and red dots the Hubble flow sample, for $z \leq 0.09$ and $z > 0.09$, respectively, together with the fitted straight lines for each sample (in green for all the Hubble flow supernovae). From these fitted curves, we can see the differences between the slopes of each rung. These facts have prompted studies into the apparent existence of a color slope step between the calibration and Hubble flow samples.

For this reason, different color correction models for the supernovae of the cosmic distance

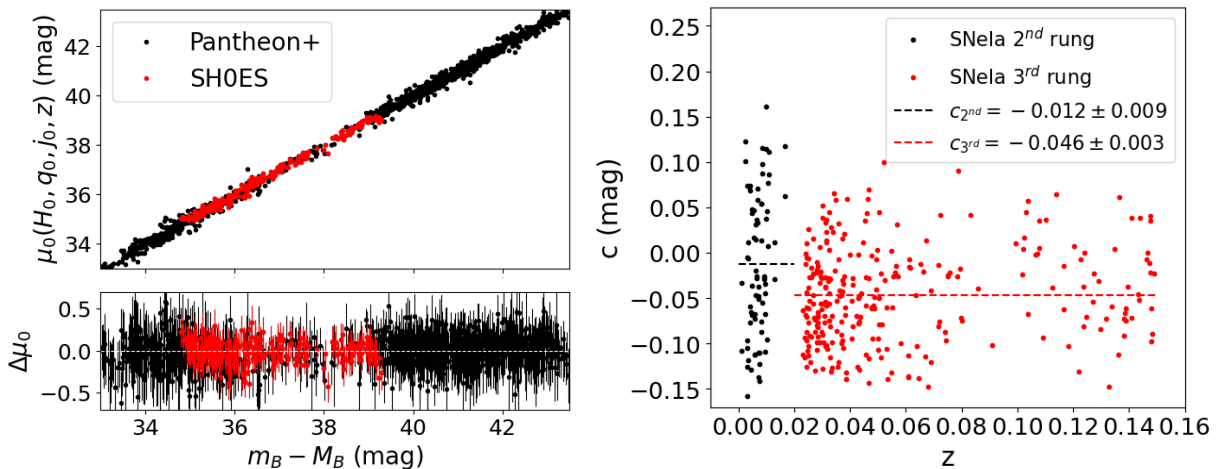


Figure 5.1: On the left, the theoretical distance modulus of supernovae $\mu_0(H_0, q_0, j_0, z)$, given by the equation (3.15), versus experimental distance modulus $\mu_0 = m_B - M_B$, after color and stretch standardization of the apparent magnitudes. The residuals $\Delta\mu_0$ between measured and theoretical values are shown at the bottom of the plot. On the right, a graph of the color for the supernovae selected by the SH0ES team as a function of their redshifts, divided into the calibration sample (black dots) and the Hubble flow sample (red dots). The average color of each sample is represented by the dotted horizontal lines.

ladder have been proposed [89, 101]. Some models will be studied in this work.

From now on, we should refer to the SNIa apparent magnitudes before color and stretch standardization as *uncorrected apparent magnitudes* or simply *uncorrected magnitudes*. The data vectors \mathbf{y} (real or synthetic) in this chapter will be built using exclusively these uncorrected magnitudes. In order to account for this change in \mathbf{y} , a correspondent modification in the theoretical model is required. Therefore, both the matrix \mathbf{L} and the vector of fitted parameters \mathbf{q} will have to be modified to account for the additional dependence of the SNIa data on color and stretch. Furthermore, changes on the covariance matrix \mathbf{C} are required because now we are dealing with a partially new data set. The form that these vectors and matrices take depends on which color correction model is being considered during the fit and this will be explained as each analysis is presented. We shall deal in this chapter with three different color correction models. Model I is the standard color correction model, which will be analyzed in section 5.1 and contains a single color correction coefficient (i.e., color slope) for all SNIa. Model II considers two color correction coefficients, one for the calibration SNe and another for the Hubble flow sample, as described in section 5.2. Model III considers two color correction coefficients and a color reference, proposed in Wojtak et al. 2022 (hereafter W22) [101], which is presented in section 5.3. All three previous models will be studied using real data. Finally, in section 5.4, a synthetic sample based on the W22 model is generated and fits considering the three color models are performed.

5.1 Standard color correction model

The formula for the apparent magnitude of a supernova, considering the standard color correction model, is given by [102, 85]:

$$m_B = \mu + M_B - \alpha x_1 + \beta c, \quad (5.1)$$

recalling that α and β are parameters related to stretch and color corrections, respectively. Then, the matrix of theoretical equations for the data should be modified to take into account the color and stretch data of the supernovae:

$$\mathbf{L}_I = \begin{pmatrix} 1 & \dots & 0 & 1 & 0 & 0 & \log_{10} P_1 - 1 & 0 & [\text{O}/\text{H}]_1 & 0 & 0 & 0 & 0 \\ \dots & \dots & \dots & \dots & \dots & \dots & \dots & \dots & \dots & \dots & \dots & \dots & \dots \\ 0 & \dots & 1 & 1 & 0 & 0 & \log_{10} P_{\text{nh}} - 1 & 0 & [\text{O}/\text{H}]_{\text{nh}} & 0 & 0 & 0 & 0 \\ \hline 0 & \dots & 1 & 1 & 0 & 0 & \log_{10} P_{\text{N4258}} - 1 & 0 & [\text{O}/\text{H}]_{\text{N4258}} & 0 & 0 & 0 & 0 \\ 0 & \dots & 0 & 1 & 0 & 1 & \log_{10} P_{\text{M31}} - 1 & 0 & [\text{O}/\text{H}]_{\text{M31}} & 0 & 0 & 0 & 0 \\ 0 & \dots & 0 & 1 & 1 & 0 & \log_{10} P_{\text{LMC}} - 1 & 0 & [\text{O}/\text{H}]_{\text{LMC}} & 0 & 0 & 0 & 0 \\ 0 & \dots & 0 & 1 & 1 & 0 & \log_{10} P_{\text{SMC}} - 1 & 0 & [\text{O}/\text{H}]_{\text{SMC}} & 0 & 0 & 0 & 0 \\ \hline 1 & \dots & 0 & 0 & 0 & 0 & 0 & 1 & 0 & 0 & 0 & c_{\text{cal},1} & x_{1,\text{cal},1} \\ \dots & \dots & \dots & \dots & \dots & \dots & \dots & \dots & \dots & \dots & \dots & \dots & \dots \\ 0 & \dots & 1 & 0 & 0 & 0 & 0 & 1 & 0 & 0 & 0 & c_{\text{cal},\text{ncc}} & x_{1,\text{cal},\text{ncc}} \\ \hline 0 & \dots & 0 & 1 & 0 & 0 & 0 & 0 & 0 & 0 & 0 & 0 & 0 \\ 0 & \dots & 0 & 1 & 0 & 0 & 0 & 0 & 0 & 0 & 0 & 0 & 0 \\ 0 & \dots & 0 & 0 & 0 & 0 & 0 & 0 & 0 & 1 & 0 & 0 & 0 \\ 0 & \dots & 1 & 0 & 0 & 0 & 0 & 0 & 0 & 0 & 0 & 0 & 0 \\ 0 & \dots & 0 & 0 & 1 & 0 & 0 & 0 & 0 & 0 & 0 & 0 & 0 \\ \hline 0 & \dots & 0 & 0 & 0 & 0 & 0 & 1 & 0 & 0 & -1 & c_{\text{HF},1} & x_{1,\text{HF},1} \\ \dots & \dots & \dots & \dots & \dots & \dots & \dots & \dots & \dots & \dots & \dots & \dots & \dots \\ 0 & \dots & 0 & 0 & 0 & 0 & 0 & 1 & 0 & 0 & -1 & c_{\text{HF},\text{nhf}} & x_{1,\text{HF},\text{nhf}} \end{pmatrix} \quad (5.2)$$

in which c_{cal} , $x_{1,\text{cal}}$ and c_{HF} , $x_{1,\text{HF}}$ are the color and stretch data from the calibration and the Hubble flow sample, respectively. The covariance matrix will be considered to be diagonal, i.e. the covariances between the cepheid metallicities (\mathbf{Z}_{cov} , given by equation (A.4) of Appendix A) and the covariances between the supernovae (\mathbf{SN}_{cov} , which are present in the covariance matrix file provided by Pantheon+) are disregarded. This is certainly a simplification, and we are aware of it. The decision to adopt a diagonal covariance matrix was taken after several attempts to build a full covariance matrix \mathbf{C}_{unc} for a data vector containing uncorrected SNIa

apparent magnitudes. In principle, the relationship between \mathbf{C}_{unc} and the full covariance matrix of corrected magnitudes \mathbf{C} is given by:

$$\mathbf{C}_{\text{unc}} = \begin{cases} \mathbf{C}, & \text{for non-SN data} \\ \mathbf{C} + \mathbf{\Delta}, & \text{for SN data} \end{cases} \quad (5.3)$$

where $\mathbf{\Delta}$ is a diagonal matrix whose elements are given by:

$$\Delta_{ij} = [\alpha^2 \sigma_{x_1}^2 + \beta_i^2 \sigma_{c_i}^2 - 2\alpha \text{cov}(m_B, x_1) + 2\beta_i \text{cov}(m_B, c) - 2\alpha\beta_i \text{cov}(x_1, c)] \delta_{ij}, \quad (5.4)$$

in which $\text{cov}(x, y)$ is the covariance between x and y , δ_{ij} is the Kronecker delta, and $\beta_i = \beta_{\text{cal}}$ for second rung SNeIa, and $\beta_i = \beta$ for Hubble flow objects. For the case under discussion in this section, $\beta_{\text{cal}} = \beta$. The use of this covariance matrix lead to least squares solutions where the uncertainty on H_0 was increased by a factor ~ 4 . Moreover, equations (5.3) and (5.4) were the ones used by our reference model in the literature, i.e., W22.

Finally, we adopted a slightly different approach as compared to W22, where we merged two diagonal matrices, one for non-SN and another for SN data. The covariances of the supernova data considering this procedure are underestimated, so it was necessary to insert a normalization factor into this data. Rescaling the SN part by a uniform factor g^2 ($g = 2.732$) in order to keep the pull distribution properly normalized (a unit variance distribution in the Gaussian limit):

$$\mathbf{C}_{\text{unc}_{ij}} = \begin{cases} C_{ii} \delta_{ij}, & \text{for non-SN data} \\ g^2 \sigma_i^2 \delta_{ij}, & \text{for SN data} \end{cases} \quad (5.5)$$

where σ_i^2 is the variance of the SN uncorrected magnitudes. On the other hand, the vector of theoretical parameters is now given by:

$$\mathbf{q}_1 = \begin{pmatrix} \mu_{0,1} \\ \dots \\ \mu_{0,\text{nh}} \\ \Delta\mu_{\text{N4258}} \\ M_H^W \\ \Delta\mu_{\text{LMC}} \\ \mu_{\text{M31}} \\ b_W \\ M_B \\ Z_W \\ \Delta zp \\ 5 \log_{10}(H_0) \\ \beta \\ \alpha \end{pmatrix} \quad (5.6)$$

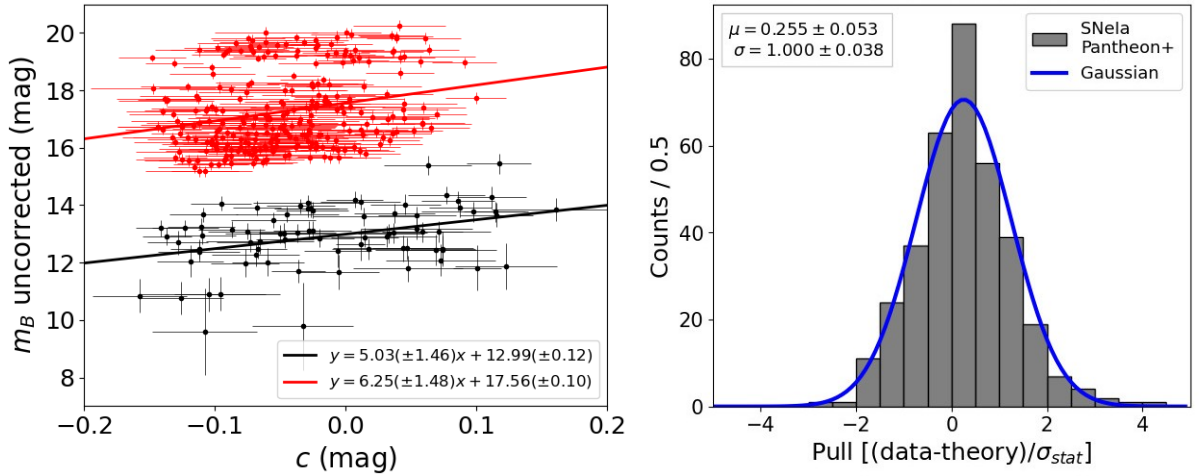


Figure 5.2: On the left: plot of uncorrected apparent magnitudes as a function of color for the second (black dots) and third rung supernovae (red dots), together with the fitted lines for each sample. On the right: histogram of pulls of real data from second and third rung supernovae selected on Pantheon+. The pulls were calculated considering a standard color correction model, furthermore, the mean value (μ) and the variance (σ) of the histogram were obtained by maximum likelihood estimation.

which includes two new entries, β and α . The only modification on the data vector is the change of standardized apparent magnitudes to uncorrected apparent magnitudes (\mathbf{y}_{unc}). Therefore, the histogram of pulls for the new supernovae data, considering the standard color correction model, is presented in Figure 5.2.

The values of the theoretical parameters resulting from the least squares solution ($\mathbf{q}_I, \text{best} = (\mathbf{L}_I^T \mathbf{C}_{unc}^{-1} \mathbf{L}_I)^{-1} \mathbf{L}_I^T \mathbf{C}_{unc}^{-1} \mathbf{y}_{unc}$) are shown in the column identified as “Model I” in Table 5.1. We can see that the parameters in this table unrelated to color and stretch standardization are consistent with those previously obtained when standardized magnitudes were used (see Chapter 3). Our stretch coefficient α is in good agreement with W22 [101] and Pantheon+ [98]. On the other hand, our color coefficient ($\beta = 2.66 \pm 0.11$) is more than 3σ away from the Pantheon+ value ($\beta = 3.09 \pm 0.04$) [98] and between 2σ to 3σ from W22 baseline model ($\beta = 3.109 \pm 0.112$) [101]. The difference between our color coefficient β and W22 baseline value could be due to: 1. the differences between the two SNeIa samples, given that W22 uses other SNeIa sample; 2. the difference in the covariance matrices. Even though, both are assumed to be diagonal, W22 incorporates information on the covariance between magnitude, color and stretch in their matrix; 3. the procedure to obtain the best-fit solution, our work relying on the least squares method, whereas W22 samples the posterior distributions where the color and stretch coefficients are sampled at every chain step, meaning that their covariance matrix changes along the MCMC chain, see equations (5.3) and (5.4).

Figure 5.3 shows the histograms of residuals for second (left) and third (right) rung

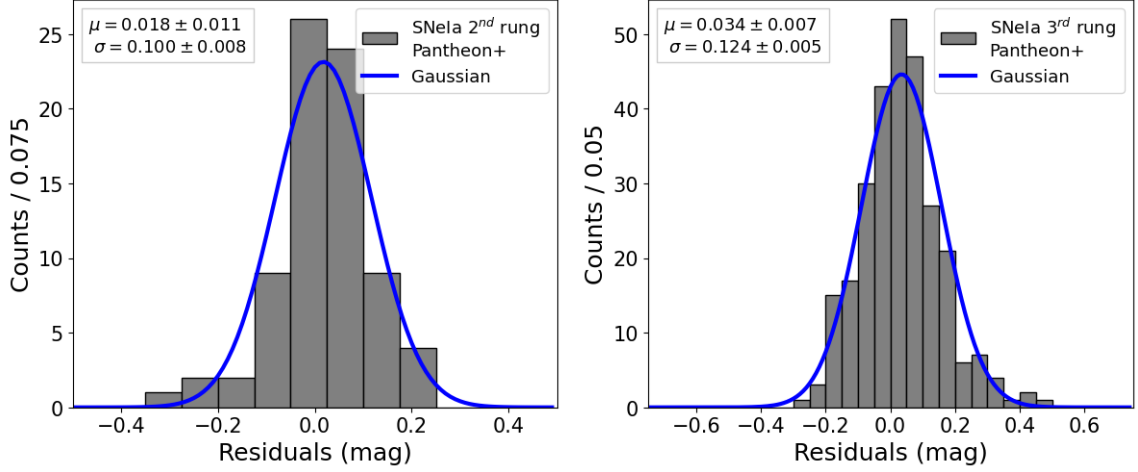


Figure 5.3: Histograms of residuals from second (left) and third rung (right) supernovae real data, considering a standard color correction model. The mean value (μ) and the variance (σ) of these histograms were obtained by maximum likelihood estimation.

supernovae data. The residuals of both histograms were calculated considering the standard color correction, Model I.

Real data			
	Model I	Model II	Model III
$\Delta\mu_{N4258} \pm \sigma_{\Delta\mu_{N4258}}$	0.005 ± 0.020	0.005 ± 0.020	0.005 ± 0.020
$M_H^W \pm \sigma_{M_H^W}$	-5.886 ± 0.017	-5.886 ± 0.017	-5.886 ± 0.017
$\Delta\mu_{LMC} \pm \sigma_{\Delta\mu_{LMC}}$	0.007 ± 0.017	0.007 ± 0.017	0.007 ± 0.017
$\mu_{M31} \pm \sigma_{\mu_{M31}}$	24.406 ± 0.024	24.406 ± 0.024	24.406 ± 0.024
$b_W \pm \sigma_{b_W}$	-3.318 ± 0.015	-3.318 ± 0.015	-3.318 ± 0.015
$M_B \pm \sigma_{M_B}$	-19.225 ± 0.025	-19.227 ± 0.025	-19.564 ± 0.032
$Z_W \pm \sigma_{Z_W}$	-0.206 ± 0.028	-0.206 ± 0.028	-0.206 ± 0.028
$\Delta zp \pm \sigma_{\Delta zp}$	-0.074 ± 0.011	-0.074 ± 0.011	-0.074 ± 0.011
$\alpha \pm \sigma_\alpha$	0.137 ± 0.007	0.137 ± 0.007	0.137 ± 0.007
$\beta \pm \sigma_\beta$	2.66 ± 0.11	2.68 ± 0.13	2.68 ± 0.13
$\beta_{\text{cal}} \pm \sigma_{\beta_{\text{cal}}}$	-	2.59 ± 0.22	2.59 ± 0.22
$5 \log_{10}(H_0) \pm \sigma_{5 \log_{10}(H_0)}$	9.328 ± 0.025	9.325 ± 0.027	9.337 ± 0.035
$H_0 \pm \sigma_{H_0}$	73.38 ± 0.86	73.28 ± 0.90	73.68 ± 1.18
χ^2/ndof	3452/3444	3452/3443	3452/3443

Table 5.1: Least squares solutions for all parameters using real data. From the left to the right: standard color correction (Model I), two different color corrections (β and β_{cal} , Model II) and β , β_{cal} and $c_{\text{ref}} = -0.13$ mag (Model III).

5.2 Model with two color correction coefficients

In this analysis, we will consider a color correction model in which there are two coefficients related to the color correction, one for the calibration sample, β_{cal} , and another for the Hubble flow supernovae, β . Therefore, for the calibration supernovae, we have:

$$m_B = \mu_0 + M_B - \alpha x_1 + \beta_{\text{cal}} c, \quad (5.7)$$

and for the Hubble flow supernovae:

$$m_B = 5 \log_{10} \left\{ \frac{cz}{H_0} [1 + 0.5(1 - q_0)z + \dots] \right\} + 25 + M_B - \alpha x_1 + \beta c. \quad (5.8)$$

To cope with this new model, we had to introduce a modified matrix \mathbf{L} to account for the difference in color standardization between the second and third rungs of the cosmic distance ladder:

$$\mathbf{L}_{\text{II}} = \begin{pmatrix} 1 & \dots & 0 & 1 & 0 & 0 & \log_{10} P_1 - 1 & 0 & [\text{O}/\text{H}]_1 & 0 & 0 & 0 & 0 & 0 \\ \dots & \dots & \dots & \dots & \dots & \dots & \dots & \dots & \dots & \dots & \dots & \dots & \dots & \dots \\ 0 & \dots & 1 & 1 & 0 & 0 & \log_{10} P_{\text{nh}} - 1 & 0 & [\text{O}/\text{H}]_{\text{nh}} & 0 & 0 & 0 & 0 & 0 \\ \hline 0 & \dots & 1 & 1 & 0 & 0 & \log_{10} P_{\text{N4258}} - 1 & 0 & [\text{O}/\text{H}]_{\text{N4258}} & 0 & 0 & 0 & 0 & 0 \\ 0 & \dots & 0 & 1 & 0 & 1 & \log_{10} P_{\text{M31}} - 1 & 0 & [\text{O}/\text{H}]_{\text{M31}} & 0 & 0 & 0 & 0 & 0 \\ 0 & \dots & 0 & 1 & 1 & 0 & \log_{10} P_{\text{LMC}} - 1 & 0 & [\text{O}/\text{H}]_{\text{LMC}} & 0 & 0 & 0 & 0 & 0 \\ 0 & \dots & 0 & 1 & 1 & 0 & \log_{10} P_{\text{SMC}} - 1 & 0 & [\text{O}/\text{H}]_{\text{SMC}} & 0 & 0 & 0 & 0 & 0 \\ \hline 1 & \dots & 0 & 0 & 0 & 0 & 0 & 1 & 0 & 0 & 0 & c_{\text{cal},1} & 0 & x_{1,\text{cal},1} \\ \dots & \dots & \dots & \dots & \dots & \dots & \dots & \dots & \dots & \dots & \dots & \dots & \dots & \dots \\ 0 & \dots & 1 & 0 & 0 & 0 & 0 & 1 & 0 & 0 & 0 & c_{\text{cal},\text{ncc}} & 0 & x_{1,\text{cal},\text{ncc}} \\ \hline 0 & \dots & 0 & 1 & 0 & 0 & 0 & 0 & 0 & 0 & 0 & 0 & 0 & 0 \\ 0 & \dots & 0 & 1 & 0 & 0 & 0 & 0 & 0 & 0 & 0 & 0 & 0 & 0 \\ 0 & \dots & 0 & 0 & 0 & 0 & 0 & 0 & 0 & 1 & 0 & 0 & 0 & 0 \\ 0 & \dots & 1 & 0 & 0 & 0 & 0 & 0 & 0 & 0 & 0 & 0 & 0 & 0 \\ 0 & \dots & 0 & 0 & 1 & 0 & 0 & 0 & 0 & 0 & 0 & 0 & 0 & 0 \\ \hline 0 & \dots & 0 & 0 & 0 & 0 & 0 & 1 & 0 & 0 & -1 & 0 & c_{\text{HF},1} & x_{1,\text{HF},1} \\ \dots & \dots & \dots & \dots & \dots & \dots & \dots & \dots & \dots & \dots & \dots & \dots & \dots & \dots \\ 0 & \dots & 0 & 0 & 0 & 0 & 0 & 1 & 0 & 0 & -1 & 0 & c_{\text{HF},\text{nhf}} & x_{1,\text{HF},\text{nhf}} \end{pmatrix} \quad (5.9)$$

The covariance matrix remains the same as before and, the vector of theoretical parameters is now given by:

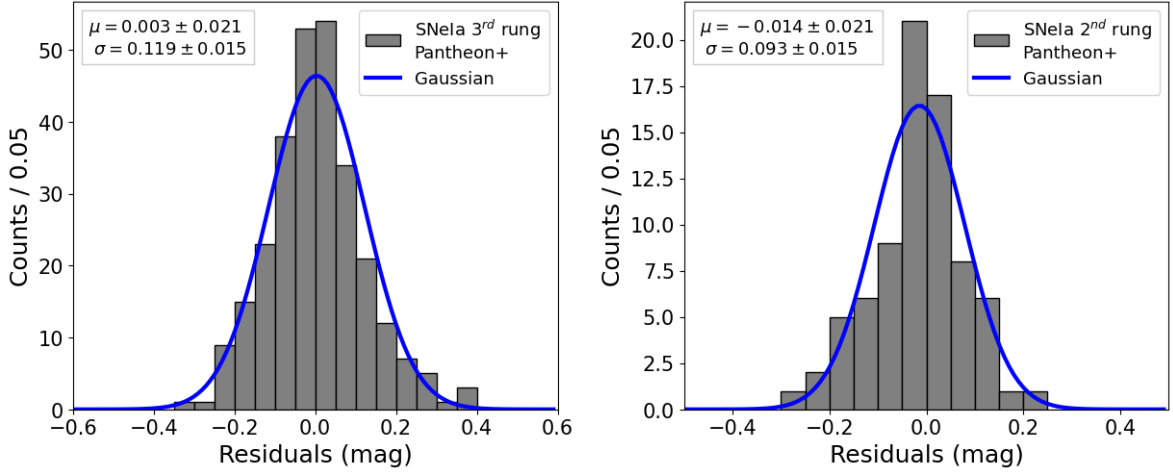


Figure 5.4: Histograms of residuals from the second (left) and third rung (right) supernovae real data, considering a model with two color correction coefficients (β_{cal} and β). The mean value (μ) and the variance (σ) of these histograms were obtained by maximum likelihood estimation.

$$\mathbf{q}_{\text{II}} = \begin{pmatrix} \mu_{0,1} \\ \dots \\ \mu_{0,\text{nh}} \\ \Delta\mu_{\text{N4258}} \\ M_H^W \\ \Delta\mu_{\text{LMC}} \\ \mu_{\text{M31}} \\ b_W \\ M_B \\ Z_W \\ \Delta zp \\ 5 \log_{10}(H_0) \\ \beta_{\text{cal}} \\ \beta \\ \alpha \end{pmatrix} \quad (5.10)$$

The least squares solution ($\mathbf{q}_{\text{II, best}} = (\mathbf{L}_{\text{II}}^T \mathbf{C}_{\text{unc}}^{-1} \mathbf{L}_{\text{II}})^{-1} \mathbf{L}_{\text{II}}^T \mathbf{C}_{\text{unc}}^{-1} \mathbf{y}_{\text{unc}}$) for the new set of parameters can be found in the column labeled as “Model II” in Table 5.1. Again, our stretch coefficient for Model II agrees with, for example, W22 baseline model ($\alpha = 0.129^{+0.008}_{-0.009}$) [101] and Pantheon+ ($\alpha = 0.148 \pm 0.04$) [98]. A difference beyond the statistical uncertainties is seen, once again, between the two color coefficients and may be due to the differences already discussed in section 5.1.

The corresponding histogram of fit residuals can be seen in Figure 5.4, for second and

third rung supernovae.

5.3 Model with two color correction coefficients and a reference color

This fit is done considering a new model of color correction, very similar to the previous one, but with the insertion of a reference color c_{ref} on the color data.

Therefore, the apparent magnitudes of the calibration supernovae are given by:

$$m_B = \mu + M_B - \alpha x_1 + \beta_{\text{cal}}(c - c_{\text{ref}}), \quad (5.11)$$

and, for the Hubble flow supernovae, the apparent magnitude can be expressed as:

$$m_B = 5 \log_{10} \left\{ \frac{cz}{H_0} [1 + 0.5(1 - q_0)z + \dots] \right\} + 25 + M_B - \alpha x_1 + \beta(c - c_{\text{ref}}). \quad (5.12)$$

Again, due to the change of the model, the matrix of equations will be modified to take into account c_{ref} in the color data:

$$\mathbf{L}_{\text{III}} = \begin{pmatrix} 1 & \dots & 0 & 1 & 0 & 0 & \log_{10} P_1 - 1 & 0 & [\text{O}/\text{H}]_1 & 0 & 0 & 0 & 0 & 0 \\ \dots & \dots & \dots & \dots & \dots & \dots & \dots & \dots & \dots & \dots & \dots & \dots & \dots & \dots \\ 0 & \dots & 1 & 1 & 0 & 0 & \log_{10} P_{\text{nh}} - 1 & 0 & [\text{O}/\text{H}]_{\text{nh}} & 0 & 0 & 0 & 0 & 0 \\ \hline 0 & \dots & 1 & 1 & 0 & 0 & \log_{10} P_{\text{N4258}} - 1 & 0 & [\text{O}/\text{H}]_{\text{N4258}} & 0 & 0 & 0 & 0 & 0 \\ 0 & \dots & 0 & 1 & 0 & 1 & \log_{10} P_{\text{M31}} - 1 & 0 & [\text{O}/\text{H}]_{\text{M31}} & 0 & 0 & 0 & 0 & 0 \\ 0 & \dots & 0 & 1 & 1 & 0 & \log_{10} P_{\text{LMC}} - 1 & 0 & [\text{O}/\text{H}]_{\text{LMC}} & 0 & 0 & 0 & 0 & 0 \\ 0 & \dots & 0 & 1 & 1 & 0 & \log_{10} P_{\text{SMC}} - 1 & 0 & [\text{O}/\text{H}]_{\text{SMC}} & 0 & 0 & 0 & 0 & 0 \\ \hline 1 & \dots & 0 & 0 & 0 & 0 & 0 & 1 & 0 & 0 & 0 & c_{\text{cal},1} - c_{\text{ref}} & 0 & x_{1,\text{cal},1} \\ \dots & \dots & \dots & \dots & \dots & \dots & \dots & \dots & \dots & \dots & \dots & \dots & \dots & \dots \\ 0 & \dots & 1 & 0 & 0 & 0 & 0 & 1 & 0 & 0 & 0 & c_{\text{cal},\text{ncc}} - c_{\text{ref}} & 0 & x_{1,\text{cal},\text{ncc}} \\ \hline 0 & \dots & 0 & 1 & 0 & 0 & 0 & 0 & 0 & 0 & 0 & 0 & 0 & 0 \\ 0 & \dots & 0 & 1 & 0 & 0 & 0 & 0 & 0 & 0 & 0 & 0 & 0 & 0 \\ 0 & \dots & 0 & 0 & 0 & 0 & 0 & 0 & 0 & 1 & 0 & 0 & 0 & 0 \\ 0 & \dots & 1 & 0 & 0 & 0 & 0 & 0 & 0 & 0 & 0 & 0 & 0 & 0 \\ 0 & \dots & 0 & 0 & 1 & 0 & 0 & 0 & 0 & 0 & 0 & 0 & 0 & 0 \\ \hline 0 & \dots & 0 & 0 & 0 & 0 & 0 & 1 & 0 & 0 & -1 & 0 & c_{\text{HF},1} - c_{\text{ref}} & x_{1,\text{HF},1} \\ \dots & \dots & \dots & \dots & \dots & \dots & \dots & \dots & \dots & \dots & \dots & \dots & \dots & \dots \\ 0 & \dots & 0 & 0 & 0 & 0 & 0 & 1 & 0 & 0 & -1 & 0 & c_{\text{HF},\text{nhf}} - c_{\text{ref}} & x_{1,\text{HF},\text{nhf}} \end{pmatrix} \quad (5.13)$$

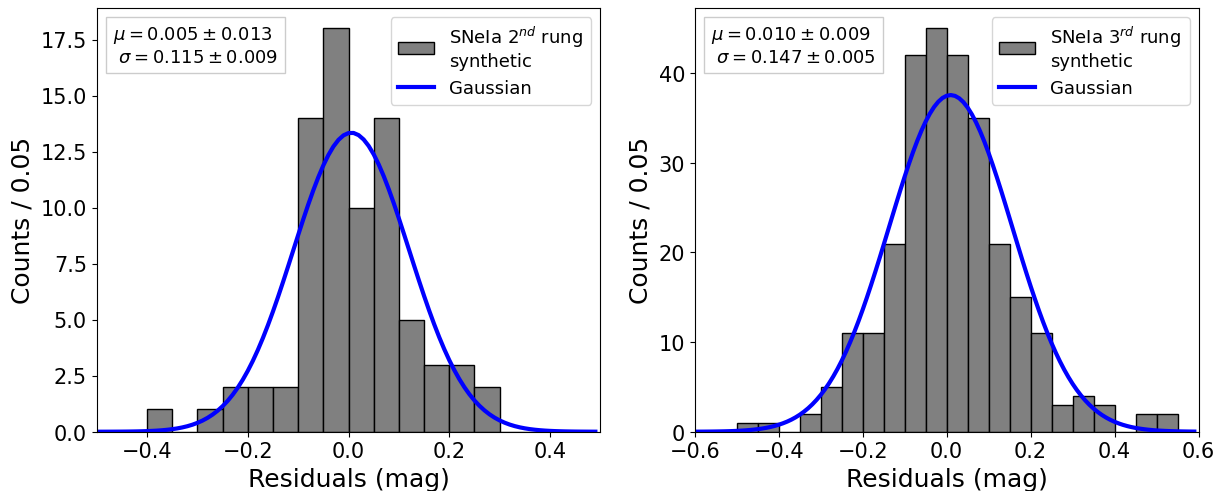


Figure 5.5: Histograms of residuals from the synthetic data of the second (left) and third (right) rung supernovae, residuals were calculated considering a model with two color correction coefficients and a reference color. Furthermore, the mean value (μ) and the variance (σ) of these histograms were obtained by maximum likelihood estimation.

As the color reference is not a fitted but a fixed parameter (here $c_{\text{ref}} = -0.13$ mag), the vector of theoretical parameters will be the same q_{II} of section 5.2.

The study of this model was also motivated by W22. As the authors argue, for the standard color correction (i.e., our Model I for which $\beta_{\text{cal}} = \beta$), changes in the reference color c_{ref} are fully absorbed by the absolute magnitude M_B of SNe Ia in both rungs of the ladder, with all the other parameters remaining protected against redefinitions of c_{ref} . In that sense, the choice a particular value of c_{ref} is an arbitrary one. However, when the calibration and SNe Ia samples show different color slopes ($\beta_{\text{cal}} \neq \beta$), this is no longer true. Now, changes in the reference color affect differently the magnitudes on the second and third rung, so that M_B can no longer absorb the changes and H_0 has also to respond.

The least squares best-fit solution ($q_{\text{III, best}} = (\mathbf{L}_{\text{III}}^T \mathbf{C}_{\text{unc}}^{-1} \mathbf{L}_{\text{III}})^{-1} \mathbf{L}_{\text{III}}^T \mathbf{C}_{\text{unc}}^{-1} \mathbf{y}_{\text{unc}}$) in this case is also presented in Table 5.1. All fitted values, except β_{cal} and β , are in agreement with those of references values.

5.4 Crosschecks with synthetic data

As we saw in the last two previous sections, models in which calibration and Hubble flow SNe Ia have magnitudes with different color slopes β_{cal} and β , respectively, do describe the data well. However, we were unable to reach one of the main conclusions of W22, i.e., that the combined SH0ES/Pantheon+ sample has enough resolution to show a statistically

	Synthetic data			
	True Values	Model III	Model II	Model I
$\Delta\mu_{N4258} \pm \sigma_{\Delta\mu_{N4258}}$	-0.015	0.012 \pm 0.020	-0.019 \pm 0.020	-0.047 \pm 0.020
$M_H^W \pm \sigma_{M_H^W}$	-5.897	-5.903 \pm 0.017	-5.901 \pm 0.017	-5.893 \pm 0.017
$\Delta\mu_{LMC} \pm \sigma_{\Delta\mu_{LMC}}$	0.009	0.006 \pm 0.017	0.015 \pm 0.017	-0.010 \pm 0.017
$\mu_{M31} \pm \sigma_{\mu_{M31}}$	24.372	24.381 \pm 0.024	24.406 \pm 0.024	24.334 \pm 0.024
$b_W \pm \sigma_{b_W}$	-3.299	-3.312 \pm 0.015	-3.289 \pm 0.015	-3.282 \pm 0.015
$M_B \pm \sigma_{M_B}$	-19.238	-19.261 \pm 0.032	-18.654 \pm 0.025	-18.658 \pm 0.025
$Z_W \pm \sigma_{Z_W}$	-0.206	-0.246 \pm 0.028	-0.231 \pm 0.028	-0.277 \pm 0.028
$\Delta zp \pm \sigma_{\Delta zp}$	-0.065	-0.020 \pm 0.011	0.015 \pm 0.011	-0.021 \pm 0.011
$\alpha \pm \sigma_\alpha$	0.148	0.147 \pm 0.007	0.144 \pm 0.007	0.149 \pm 0.007
$\beta \pm \sigma_\beta$	3.09	3.12 \pm 0.12	2.93 \pm 0.13	3.35 \pm 0.11
$\beta_{\text{cal}} \pm \sigma_{\beta_{\text{cal}}}$	4.57	4.59 \pm 0.22	4.57 \pm 0.22	-
$5 \log_{10}(H_0) \pm \sigma_{5 \log_{10}(H_0)}$	9.318	9.136 \pm 0.035	9.331 \pm 0.028	9.297 \pm 0.025
$H_0 \pm \sigma_{H_0}$	67.36	67.16 \pm 1.08	73.50 \pm 0.91	73.34 \pm 0.84
χ^2/ndof	-	3512/3443	3408/3443	3339/3444

Table 5.2: Least squares solutions for all parameters using synthetic data. From the left to the right: True values used in the data generation, fit considering the model with β , β_{cal} and $c_{\text{ref}} = -0.13$ mag, fit with β and β_{cal} , and fit considering the standard color correction model. The reference values of α and β are extracted from [98], β_{cal} from [101] and others from [31].

significant difference between the best-fit values of β_{cal} and β . Moreover, they conclude that a choice of $c_{\text{ref}} = -0.13$ solves the Hubble tension, with their best fit value pulling H_0 down to the vicinity of the CMB value. For all our fits, however, we have obtained least squares best-fit values of calibration and Hubble flow color slopes that are compatible with each other within statistical uncertainties and we were unable to find a choice of reference color that could significantly shift H_0 . Due to this, we decided to make an additional test in a controlled environment, i.e., using synthetic samples having a covariance similar to real data, to check if resolution was the real explanation behind the mentioned compatibility.

Therefore, a synthetic data sample was generated, following the model proposed by W22 [101] (with β , β_{cal} and c_{ref}), so the data vector $\mathbf{y}_{\text{syn}}^{\text{III}}$ was given by:

$$\mathbf{y}_{\text{syn}}^{\text{III}} = \mathbf{L}_{\text{III}} \mathbf{q}_{\text{best}} + \mathbf{x}, \quad (5.14)$$

where \mathbf{q}_{best} is the vector composed by the central values obtained by R22 (see the second column of Table 5.2), except for H_0 , which in this case was fixed at $67.36 \text{ km s}^{-1} \text{ Mpc}^{-1}$ [8], \mathbf{x} is a vector of N (zero mean and covariance \mathbf{C}_{unc}) Gaussian random variables with posterior distribution functions given by:

$$p(\mathbf{x}) = \frac{1}{(2\pi)^{N/2}(\det \mathbf{C}_{\text{unc}})^{1/2}} \exp \left[-\frac{1}{2} \mathbf{x}^T \mathbf{C}_{\text{unc}}^{-1} \mathbf{x} \right]. \quad (5.15)$$

The histograms of residuals for the supernovae from this sample are shown in Figure 5.5. The three previous models of sections 5.1, 5.2 and 5.3 (Model I, II and III, respectively) were considered during the fits performed with this synthetic data sample, for which the least squares solutions are shown in Table 5.2.

We can see that, considering Model III, proposed by W22, all parameters are in line with the true values, as it was expected, since there is consistency between fit and data generation. However, when both Models I and II are used to fit the data, significant biases appear on H_0 and M_B , beyond the statistical uncertainties on these parameters. These biases are fully consistent with the study on systematic effects presented in Chapter 4, because the lack of a degree of freedom in the model to account for the color slope step of the data is equivalent to a non-uniform bias across the calibration and Hubble flow SNeIa samples.

6 | The $f(z)$ CDM approach

The content of this chapter is based on the work Petreca et al. (2024) [103], developed during an internship of six months done at Scuola Superiore Meridionale - Università degli Studi di Napoli, in Italy, under supervision of Dr. Micol Benetti. The main objective of this internship was to study the Hubble constant from the theoretical point of view, proposing a hybrid approach as a solution for the Hubble tension. This method combines the Λ CDM model with cosmography, which was parameterized with different Padé series.

6.1 Extensions to the standard cosmological model

Although the discrepancies in the Hubble constant and the $\sigma_8 - S_8$ values (σ_8 is the galaxy clustering at $8h^{-1}\text{Mpc}$ and $S_8 = \sigma_8\sqrt{\Omega_m/0.3}$, in which Ω_m is the fractional matter energy density of all forms of matter) can have systematic effects as their origin, due to their persistence after several years, many studies are focusing on models that address new physics and generalizations beyond the standard model [104] have arisen as a solution for these problems, which also open the way for the exploration of new techniques in cosmology, such as the cosmography [74, 105].

Several extensions of the standard cosmological model are being studied, among them the possibility of new physics in the early universe (as early dark energy and modifications of the recombination history) and late universe evolution (bulk velocity model, clustering dark energy, diffusion model and dynamical dark energy). The dynamical dark energy has been extensively studied in the literature [106, 107, 108], also based on data to reconstruct the dark energy equation of state parameter w [109]. The phantom-like models, $w < -1$, of this class of dark energy theories generally solve the H_0 tension, however, it seems to increase the discrepancy in the $\sigma_8 - S_8$ values. [110].

On the other hand, cosmography allows data to be analyzed independently of a model, based only on the assumptions of homogeneity and isotropy of the Universe. This technique allows to reconstruct a dynamic evolution of the dark energy term at late times without assuming any particular cosmological model. It is usually based on the Taylor series of the scalar factor $a(t)$ and its higher-order derivatives. This expansion is directly compared with low and high redshift astrophysical data which allows, assuming a fiducial value for the current matter density fraction (dark and baryonic), to reconstruct the Hubble parameter as

a function of redshift. In the last years, improvements have been observed in the development of cosmography in the areas of astrophysics and cosmology, considering rational polynomials in its construction in order to guarantee greater stability at large redshifts [111].

In this chapter, we intend to study an extension of the standard cosmological model, exploring an approach that combines the Λ CDM model with a fast-convergence cosmographic series, a model of the $f(z)$ CDM type. Specifically, the procedure consists of constructing a redshift function $f(z)$ based on specific polynomials, capable of describing the kinematics of the universe up to a given redshift without imposing any dark energy model and then, after this transition redshift, a standard evolution described by the Λ CDM model. Before studying the $f(z)$ CDM approach itself, it is necessary to understand what is cosmography.

6.2 Cosmography

The luminosity distance of an object can be written in terms of its observed redshift z :

$$d_L = (1+z)d(z) = (1+z)\frac{c}{H_0} \int_0^z \frac{dz'}{H(z')}, \quad (6.1)$$

in which $d(z)$ is the comoving distance, c is the speed of light and H_0 is the Hubble constant. For low redshifts, the Hubble-Leimaître law can be used in place of comoving distance $d(z) = v(z)/H_0$. Recalling that $v(z) \approx zc$, then, for low redshifts, the luminosity distance can be written as follows:

$$d_L = \frac{cz}{H_0}. \quad (6.2)$$

For high redshifts, one can assume a cosmological model to make explicit the evolution of $H(z)$ in equation (6.1) in terms of universe fluids density and dynamics. Alternatively, the luminosity distance can be expressed in a model-independent parametric way by adopting the cosmographic approach, a technique capable of tracing back the universe kinematics without the need to assume specific cosmological models [74].

A model-independent reconstruction of the cosmic history should be based on a robust analysis of cosmological observations. In other words, data should be able to provide reliable constraints on the behavior of cosmographic parameters, evolving with redshift, independently of any cosmological model or underlying gravity theory. It has been shown, for example, that adopting SNeIa data it is possible to reconstruct the Hubble parameter [112] and this can be done with any other cosmographic parameter, in principle.

Cosmography relies on the kinematics of cosmological expansion to reconstruct the cosmological dynamics [113, 111]. Specifically, we can expand the scale factor, which is the only

degree of freedom governing the Universe according to the cosmological principle, around the present epoch (t_0):

$$a(t) = 1 + \sum_{k=1}^{\infty} \frac{1}{k!} \left. \frac{d^k a}{dt^k} \right|_{t=t_0} (t - t_0)^k, \quad (6.3)$$

and define the Hubble $H(t)$, deceleration $q(t)$, jerk $j(t)$, snap $s(t)$, lerk $l(t)$ and pop $p(t)$ parameters respectively as:

$$H(t) \equiv \frac{1}{a} \frac{da}{dt}, \quad q(t) \equiv -\frac{1}{aH^2} \frac{d^2 a}{dt^2}, \quad (6.4a)$$

$$j(t) \equiv \frac{1}{aH^3} \frac{d^3 a}{dt^3}, \quad s(t) \equiv \frac{1}{aH^4} \frac{d^4 a}{dt^4}, \quad (6.4b)$$

$$l(t) \equiv \frac{1}{aH^5} \frac{d^5 a}{dt^5}, \quad p(t) \equiv \frac{1}{aH^6} \frac{d^6 a}{dt^6}. \quad (6.4c)$$

These parameters provide information about the dynamics of the universe. The sign of the deceleration parameter indicates if the universe is accelerating or decelerating and the sign of the jerk indicates how the acceleration of the universe changes with time. In contrast, higher-order parameters can be included to refine the evolutionary behavior [113, 44]. These higher-order parameters are not necessarily considered in the expansions, but are presented here because they may be mentioned in the future.

The Hubble parameter can be written also in terms of the redshift, performing a Taylor expansion around $z = 0$ as:

$$H(z) = H(0) + \left. \frac{dH(z)}{dz} \right|_{z=0} z + \left. \frac{d^2 H(z)}{dz^2} \right|_{z=0} z^2 + O(z^3), \quad (6.5)$$

knowing the derivatives of $H(z)$ with respect to time:

$$\frac{dH}{dt} = -H^2(1 + q), \quad \frac{d^2 H}{dt^2} = H^3(j + 3q + 2), \quad \dots, \quad (6.6)$$

and making a time to redshift change of variables:

$$\frac{d}{dt} = -(1 + z)H \frac{d}{dz}, \quad \frac{d^2}{dt^2} = (1 + z)H \left[H + (1 + z) \frac{dH}{dz} \right] \frac{d}{dz} + (1 + z)^2 H^2 \frac{d^2}{dz^2}, \quad \dots, \quad (6.7)$$

it is possible to obtain the derivatives of $H(z)$ with respect to redshift:

$$\frac{dH}{dz} = H \frac{1 + q}{1 + z}, \quad \frac{d^2 H}{dz^2} = H \frac{j - q^2}{(1 + z)^2}, \quad \dots. \quad (6.8)$$

Then, replacing these derivatives (6.8) into equation (6.5):

$$\begin{aligned}
 H(z) = H_0 \{ & 1 + (1 + q_0)z + \frac{1}{2}(j_0 - q_0^2)z^2 - \frac{1}{6}[-3q_0^2 - 3q_0^3 + j_0(3 + 4q_0) + s_0]z^3 + \frac{1}{24}[-4j_0^2 + l_0 \\
 & - 12q_0^2 - 24q_0^3 - 15q_0^4 + j_0(12 + 32q_0 + 25q_0^2) + 8s_0 + 7q_0s_0]z^4 + \frac{1}{120}(p_0 + 15l_0 + 60(s_0 \\
 & + j_0 - j_0^2 + 4j_0q_0 + s_0q_0^2 - q_0^2 - 3q_0^3) - 15s_0j_0 + 11l_0q_0 + 105s_0q_0 - 70j_0^2q_0 + 375j_0q_0^2 \\
 & + 210j_0q_0^3 - 225q_0^4 - 105q_0^5)z^5 + O(z^6)\},
 \end{aligned} \tag{6.9}$$

in which $H_0 = H(0)$, $q_0 = q(0)$ and successively [44]. The expression for the luminosity distance in terms of these cosmographic coefficients can be obtained through equations (6.1) and (6.9):

$$\begin{aligned}
 d_L(z) = \frac{cz}{H_0} \{ & 1 + \frac{z}{2}(1 - q_0) - \frac{z^2}{6}(1 - q_0 - 3q_0^2 + j_0) + \frac{z^3}{24}(2 - 2q_0 - 15q_0^2 - 15q_0^3 + 5j_0 + 10q_0j_0 + s_0) \\
 & - z^4 \left(\frac{1}{20} - \frac{9j_0}{40} + \frac{j_0^2}{12} - \frac{l_0}{120} + \frac{q_0}{20} - \frac{11q_0j_0}{12} + \frac{27q_0^2}{40} - \frac{7j_0q_0^2}{8} + \frac{11q_0^3}{8} + \frac{7q_0^4}{8} - \frac{11s_0}{120} - \frac{q_0s_0}{8} \right) \\
 & + z^5 \left[-\frac{1}{20} - \frac{9j_0}{40} + \frac{j_0^2}{12} - \frac{l_0}{120} + \frac{q_0}{20} - \frac{11q_0j_0}{12} + \frac{27q_0^2}{40} - \frac{7j_0q_0^2}{8} + \frac{11q_0^3}{8} + \frac{7q_0^4}{8} - \frac{11s_0}{120} - \frac{q_0s_0}{8} \right] \\
 & + O(z^6)\}.
 \end{aligned} \tag{6.10}$$

For small redshifts, it is not necessary to consider expansions up to the fifth order in the redshift, as done in the expressions (6.9) and (6.10), however, they are presented here because they are necessary for calculating the coefficients of the Padé series studied in this work.

The slow convergence rate of the Taylor series makes this method poorly predictive for cosmographic analysis for $z > 1$ [113, 111]. This problem can be partially alleviated by adopting the Padé or Chebyshev rational polynomials [74, 111, 114, 115], or logarithmic polynomial series [105], for example, to construct a cosmographic series based only on the assumption of cosmic homogeneity and isotropy.

6.3 Padé series

The Padé series arises in the context of cosmography to improve the convergence speed compared to the Taylor series in $z > 1$. The Padé series are given by the following expression:

$$P_{nm}(z) = \frac{\sum_{i=0}^n a_i z^i}{1 + \sum_{j=1}^m b_j z^j}. \quad (6.11)$$

where n and m indicates the order of the series and also the orders in the numerator and the denominator, respectively. The advantages of Padé in comparison with Taylor approximations are: the Padé series can improve the convergence speed for $z > 1$, since the denominator can stabilize the function; can reduce error propagations in this redshift range; and the series can be calibrated by choosing appropriate orders for a specific situation [111]. In general, a worse stability is noted when the series terms contains polynomials of the same order in the numerator and denominator, and a better stability when the denominator order is lower than the numerator one. Then rational approximations with the same order in the numerator and denominator do not provide accurate cosmographic results [114]. Indeed, P_{22} has been shown to have poor convergence behavior, compared to P_{32} and P_{21} [116], but also this order will be studied in this work together with the other two, because it is widely used in literature. Therefore, one of the goals of this work is to better understand the behavior of Padé approximation in cosmography and compare different orders of polynomials. We also want to understand how Λ CDM can be improved by changing the usually fixed term, Ω_Λ on the background evolution according to redshift.

The Padé series mentioned before that will be used in this work are the following:

$$P_{21}(z) = \frac{P_0 + P_1 z + P_2 z^2}{1 + Q_1 z}, \quad (6.12)$$

$$P_{22}(z) = \frac{P_0 + P_1 z + P_2 z^2}{1 + Q_1 z + Q_2 z^2}, \quad (6.13)$$

$$P_{32}(z) = \frac{P_0 + P_1 z + P_2 z^2 + P_3 z^3}{1 + Q_1 z + Q_2 z^2}, \quad (6.14)$$

in which the coefficients P_0 , P_1 , P_2 , P_3 , Q_1 and Q_2 can be determined by matching the series derivatives at $z = 0$ with those of the Taylor series of a given function of interest $f(z) = \sum_{i=0}^{\infty} c_i z^i$:

$$P_{nm}(0) = f(0), \quad (6.15)$$

$$P'_{nm}(0) = f'(0), \quad (6.16)$$

⋮

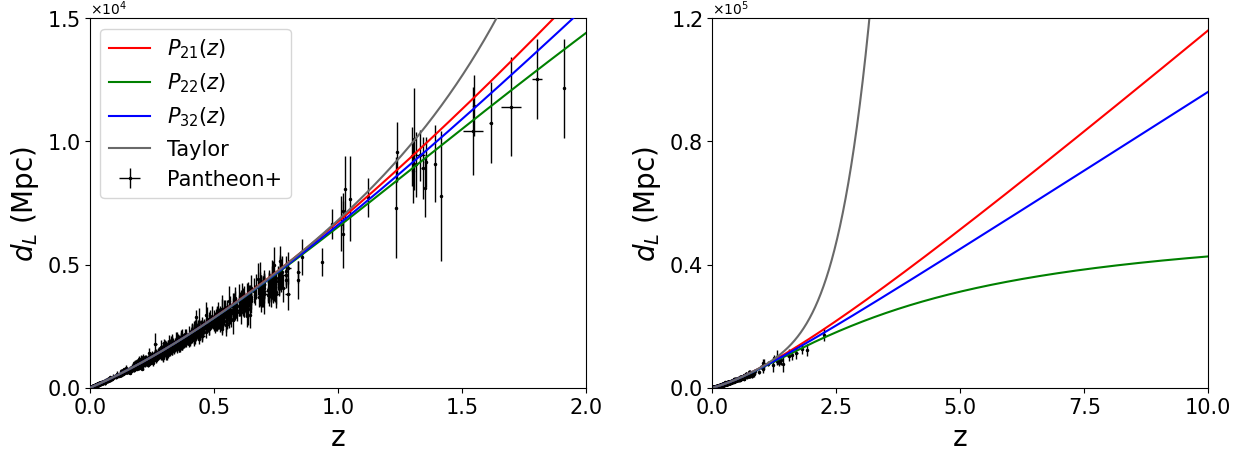


Figure 6.1: Luminosity distance d_L compared with Pantheon+ catalog [98], considering different orders of the Padé series, see equations (6.12), (6.13) and (6.14), together with the Taylor series expansion up to fifth order in redshift. The set of cosmographic parameter values is given by $\{q_0 = -0.55, j_0 = 1, l_0 = 0.685, s_0 = -0.35, p_0 = 1\}$, as used in [116]. Furthermore, the left plot is a zoom of the plot on the right for the region $z \leq 2$.

$$P_{nm}^{(n+m)}(0) = f^{(n+m)}(0). \quad (6.17)$$

This can be done considering for $f(z)$ the luminosity distance Taylor formula of as equation (6.10), as well as considering the background evolution itself, as given by equation (6.9). The complete expressions for both Padé-based $d_L(z)$ and $H(z)$ are reported in Appendix C. Figures 6.1 and 6.3 show a comparison between the Padé-based and the Taylor series for the luminosity distance as a function of redshift together with Pantheon+ SNeIa and Cosmic cronometers data. [117, 118, 119, 120, 121, 122]. It is possible to verify that the truncated Taylor expansion diverges for redshift higher than $z = 2$ while the Padé approximants are able to keep a more stable behavior.

When calculating the Padé-based series and Taylor polynomials for Figure 6.1, the values of cosmographic parameters used were: $q_0 = -0.55, j_0 = 1, s_0 = -0.35, l_0 = 0.685$, and $p_0 = 1$. These coefficients are obtained by comparing the theoretical expression from the Λ CDM model background:

$$H(z) = H_0 \sqrt{\Omega_m(1+z)^3 + \Omega_r(1+z)^4 + 1 - \Omega_r - \Omega_m}, \quad (6.18)$$

and the cosmographic expression for the Hubble parameter of equation (6.9), assuming $H_0 = 70 \text{ km s}^{-1} \text{ Mpc}^{-1}$, $\Omega_r = 5 \times 10^{-5}$ and $\Omega_m = 0.3$ [116]. Clearly, these are only indicative values, and for the present purposes hereafter it will be consider cosmographic parameters only up to the third order (i.e., fourth order derivatives) fixing the higher order ones at zero, $l_0 = p_0 = 0$.

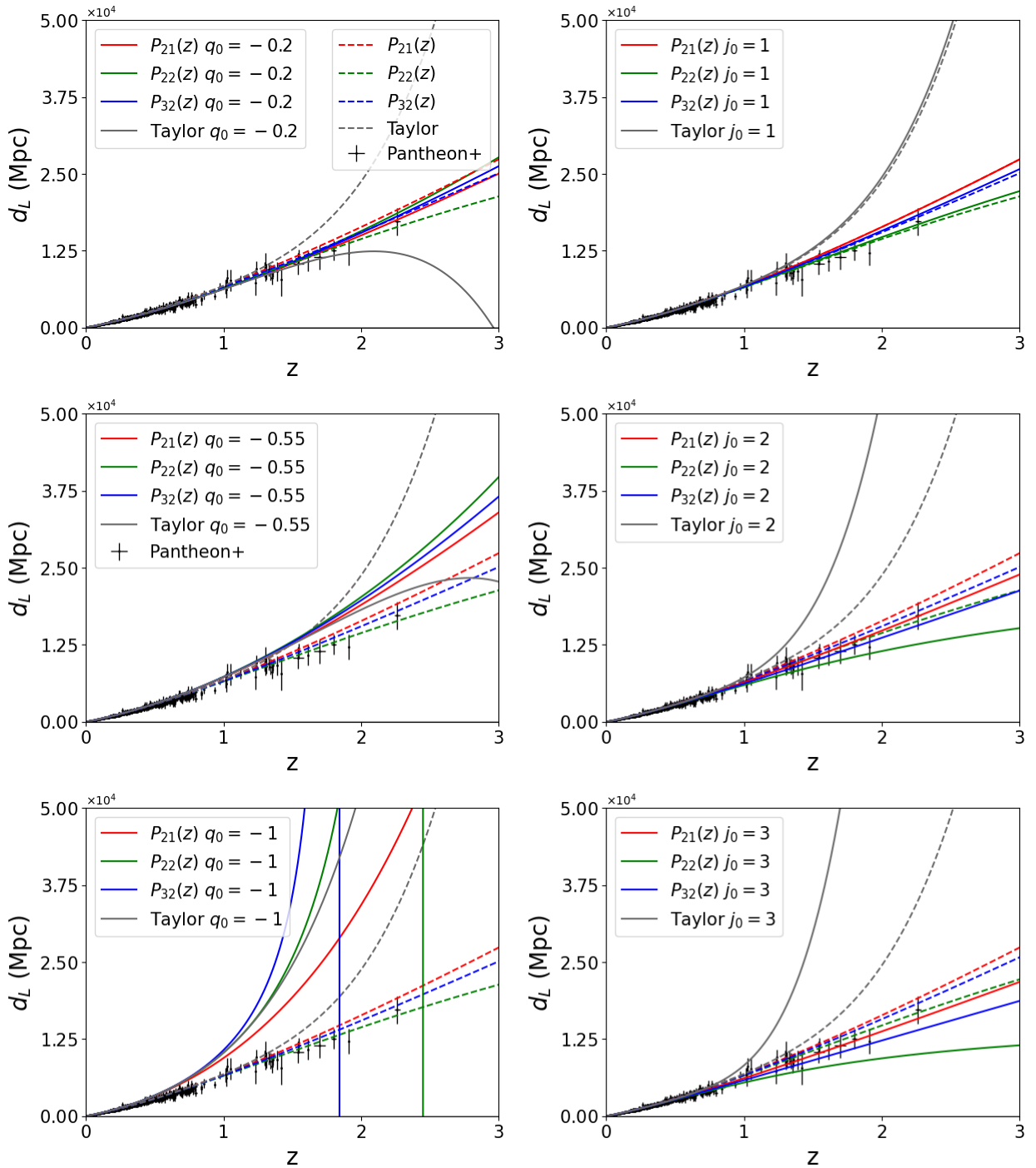


Figure 6.2: On the left, d_L vs z considering P_{21} , P_{22} , P_{32} and the Taylor expansion with $q_0 = -0.2$, $q_0 = -0.55$ and $q_0 = -1$, respectively (full lines). In all these cases $j_0 = 0$, $l_0 = 0$, $s_0 = 0$ and $p_0 = 0$. Furthermore, together with these curves, the curves from Figure 6.1 are presented (dashed lines), in which $q_0 = -0.55$, $j_0 = 1$, $l_0 = 0.685$, $s_0 = -0.35$ and $p_0 = 1$, for comparison purposes. On the right, there are the cases with $q_0 = -0.55$ and $j_0 = 1$, $j_0 = 2$ and $j_0 = 3$, respectively, also with the curves from Figure 6.1.

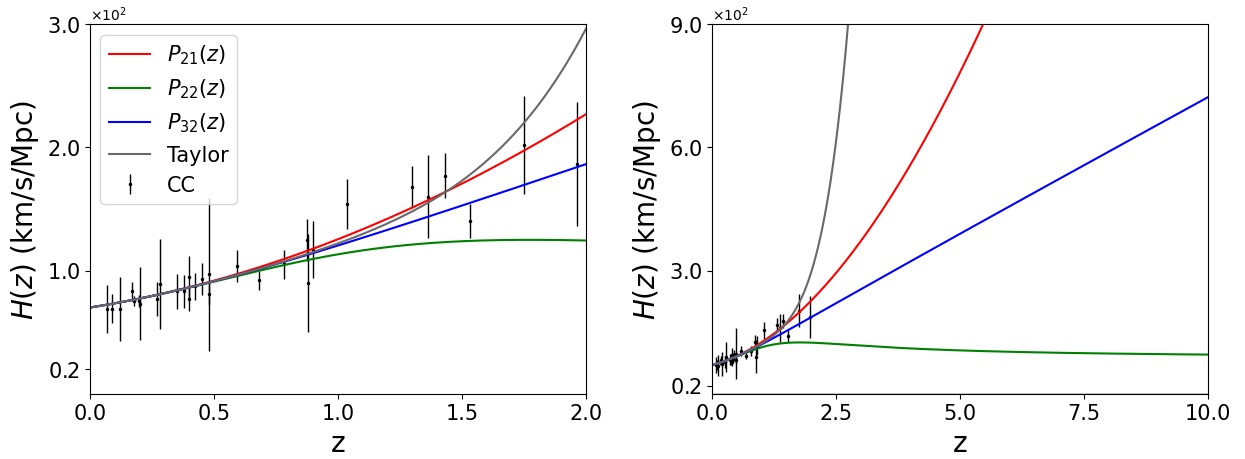


Figure 6.3: The background evolution $H(z)$ compared with Cosmic Chronometers data [117, 118, 119, 120, 121, 122], considering three different orders of Padé series, see equations (6.12), (6.13) and (6.14), together with the Taylor series expansion up to fifth order in redshift, with $H_0 = 70 \text{ km s}^{-1} \text{ Mpc}^{-1}$, $q_0 = -0.55$, $j_0 = 1$, $s_0 = -0.35$, $l_0 = 0.685$ and $p_0 = 1$, like in [116]. The left plot is a zoom of the plot on the right for the region $z < 2$.

The behavior of the luminosity distance under changes of q_0 is analyzed in Figure 6.2, with $q_0 = -0.2$ (on the top left), $q_0 = -0.55$ (in the middle left) and $q_0 = -1$ (at the bottom left) (these curves are represented with full lines, and for all three curves we set $j_0 = 0, l_0 = 0, s_0 = 0$ and $p_0 = 0$), compared with the curves of Figure 6.1 (dashed lines). It is possible to observe from this figure that, as the value of q_0 decreases, the parameter describing the type of acceleration of the universe (if negative, the expansion is accelerated, and if positive, decelerated), the universe acceleration increases and this causes a rise in the derivatives of the curves for d_L . In the picture on the middle left, q_0 has a value considerably lower than the standard one and in this case, the d_L curves are steeper than the nominal ones. Furthermore, in the case where $j_0 = 1$ (graph on the top right), one can see that the differences between the fiducial Padé curves ($q_0 = -0.55, j_0 = 1, l_0 = 0.685, s_0 = -0.35, p_0 = 1$) and the others ($q_0 = -0.55, j_0 = 1, l_0 = s_0 = p_0 = 0$) are very small, what means that variations in the higher order cosmographic parameters, like s_0, l_0 and p_0 , do not play a relevant role on the behavior of the Padé series for d_L .

In the three graphs on the right of Figure 6.2, it is possible to verify the impact of the parameter j_0 in the luminosity distance curves. In all cases $q_0 = -0.55$ and $s_0 = l_0 = p_0 = 0$. In the top right, only the jerk parameter is changed, being $j_0 = 1$. In the middle right is the case with $j_0 = 2$ and on the bottom right is the case with $j_0 = 3$. Note that as the value of j_0 changes, the concavity of the curves is modified.

Figure 6.3 shows plots for the $H(z)$ evolution for P_{21} , P_{22} and P_{32} orders of the Padé series, together with Cosmic Chronometers (CC) data [117, 118, 119, 120, 121, 122]. The

plots on the left and on the right have the same data, however, the ones on the left have a smaller redshift interval. From the plot on the right-hand side, it is possible to verify that all the orders are well-behaved until $z = 10$, but P_{21} is less stable (presents more divergences) than P_{22} and P_{32} , while from the plots on the left, it is observed that the series do not show very significant differences until $z = 1$.

In addition, we noticed that by increasing polynomial order, there is a significant difference change in behavior of both $d_L(z)$ and $H(z)$. Among the three Padé combinations considered, and the fiducial cosmographic values assumed, P_{32} stands out for its convergence properties. Thus, it seems interesting to consider the Padé series of higher orders for their improved stability, although such a choice makes the calculations of the polynomial coefficients more complex. To better understand the role of these coefficients and identify the one that maximizes the difference between the three series considered, the Padé coefficients of equations (6.12)-(6.14) are plotted as a function of q_0 (left column) and j_0 (center and right columns) in Figure 6.4. For the left plots, and for the sake of simplicity and clarity, we adopted $j_0 = 1$ and $s_0 = l_0 = p_0 = 0$. For the center and right column plots, we have $q_0 = -0.55$ and $q_0 = -1$,

It is possible to state that, depending on the series analyzed and the cosmographic values assumed, Padé coefficients always diverge for a specific value. For example, in the case of P_{32} , this happens at $q_0 = -1.3$, which is outside the values of interest (i.e., $q_0 = -0.55$), while for P_{21} the divergence occurs at $q_0 = -1$, which is more closer to the fiducial value. This obviously depends on the value of j_0 chosen. The same happens for the jerk parameter, where the divergence moves to larger values of j_0 as q_0 decreases. The existence of this divergence, therefore, defines the exploration range of each parameter. At the same time, the Padé coefficients can be directly constrained by the data, and take values approximately in the range $[-2;2]$ [123, 124, 125]. This additional information can be used to exclude ranges of cosmographic parameter values that generate coefficients far from these constraints.

Also, it is noted that higher-order cosmographic parameters can play an important role in the P_{32} approximation. Indeed, in Figure 6.5 it is explored the dependence with the snap value assuming $q_0 = -0.55$, $j_0 = 1$ and $l_0 = p_0 = 0$ on the left, while in the central and right column it is showed the q_0 and j_0 dependencies assuming $s_0 = -0.35$ and $s_0 = 0.35$, respectively and also considering $l_0 = p_0 = 0$. From the left column, it is noted that introducing a non-zero value of s_0 does not significantly change the values of Padé coefficients, which show an almost constant behavior, except the series P_{32} where P_1 , Q_1 , Q_2 seem to have some sensitivity to the snap. On the other hand, it is possible to see that assuming a non-zero value of s_0 can significantly change the singular behavior of the Padé coefficients when they are seen as functions of j_0 (right column), going so far as to eliminate it from the range of interest for

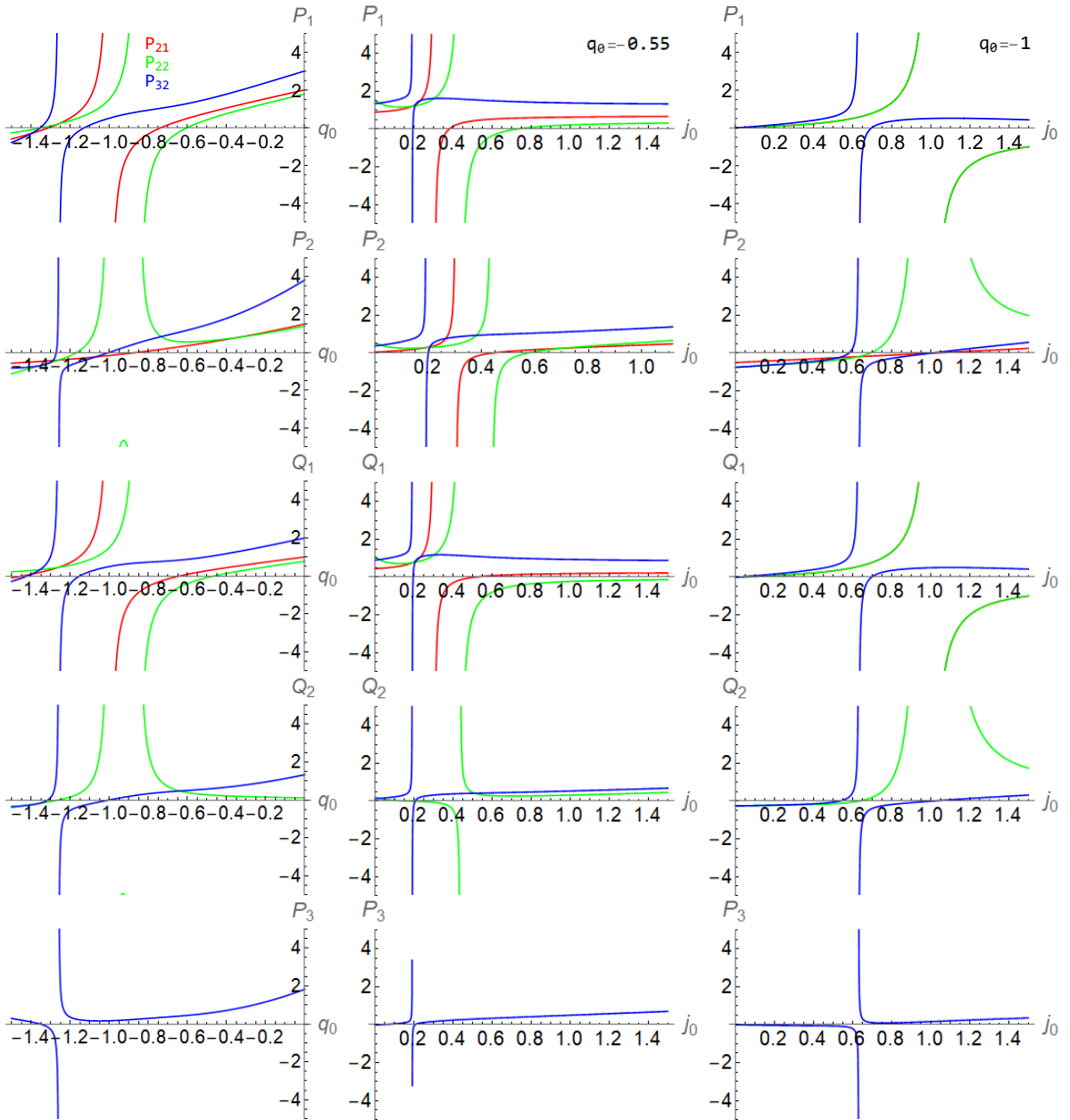


Figure 6.4: P_1 , P_2 , P_3 , Q_1 and Q_2 coefficients behavior as a function of q_0 (left), j_0 (center and right) for the three Padé series. The red curves are not present in the graphs on the top and bottom right because they are overlapped by the green curves. The values considered for the cosmography parameters on the left are $j_0 = 1$, $s_0 = 0$, and $l_0 = 0$. In the central, $q_0 = -0.55$, while we assume $q_0 = -1$ on the right (also considering $s_0 = l_0 = 0$).

the series P_{32} and P_{22} in the case of $s_0 = 0.35$ (dashed line). Thus, one can conclude that although the cosmographic parameters beyond the jerk are generally not well constrained by the data [74, 116], their values can influence the stability of the Padé series coefficients, and this fact can be used to avoid numerical problems in the analyses. Unfortunately, $s_0 = 0.35$

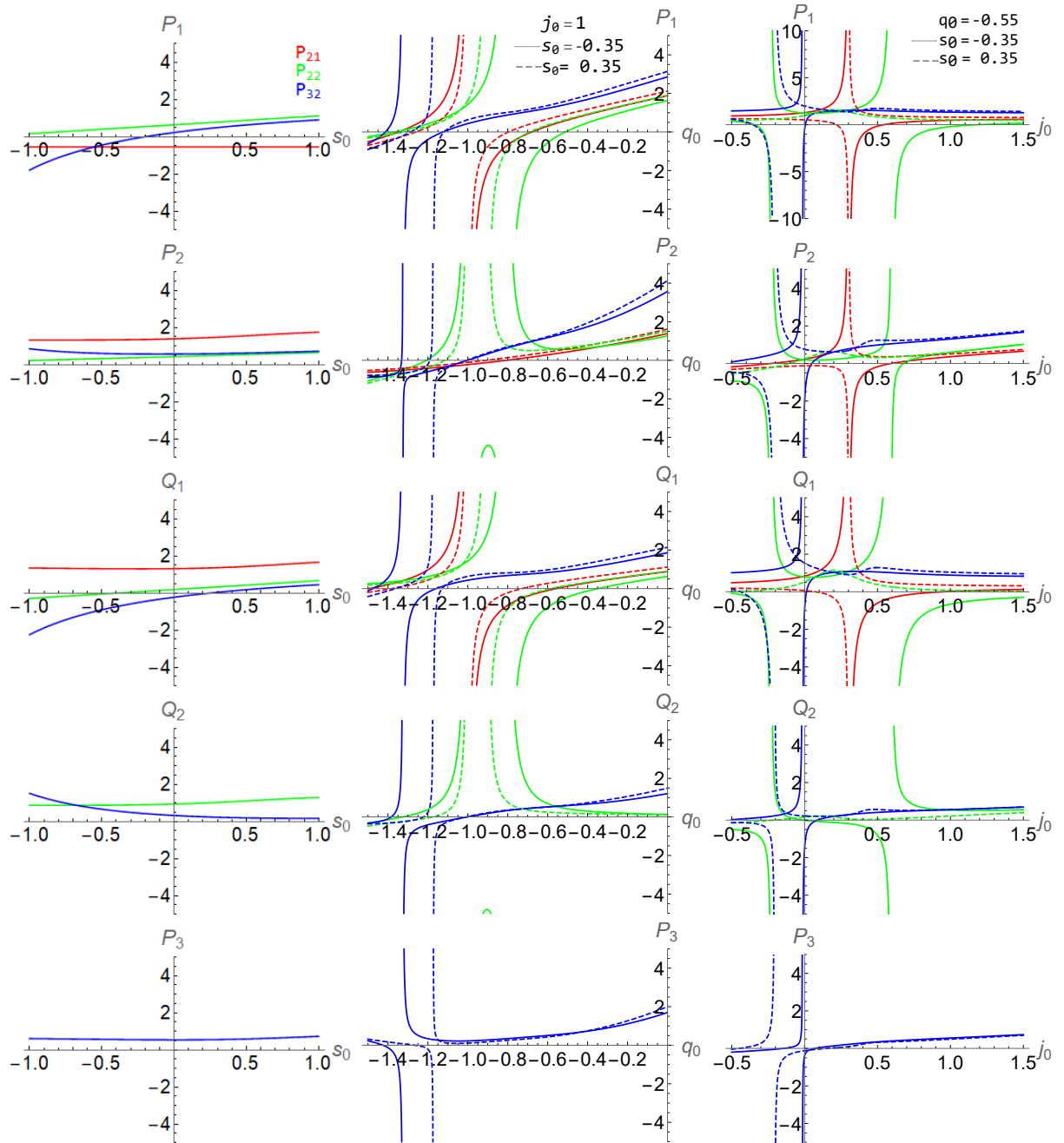


Figure 6.5: P_1 , P_2 , P_3 , Q_1 and Q_2 coefficients behavior as a function of s_0 for the three Padé series (on the left), with $q_0 = -0.55$ and $j_0 = 1$. These Padé series are presented also as a function of q_0 (central), with $j_0 = 1$, $s_0 = -0.35$ (solid lines) and $s_0 = 0.35$ (dashed lines) and as a function of j_0 , with $q_0 = -0.55$ for the same values of s_0 . Here all plots consider $l_0 = p_0 = 0$.

does not remove the singularities (see central column) at $q_0 = -1.0$ for P_{21} , $q_0 = -0.9$ for P_{22} and $q_0 = -1.2$ for P_{32} . At the same time, exploring $s_0 < 0$ shifts these singularities of q_0 to smaller values, but very slowly, for example, at $s_0 = -0.35$ the divergence is moved

to $q_0 = -1.4$ for P_{32} . It is important to stress that it is not desirable to consider a value of s_0 significantly different from zero because this parameter has physical meaning and the observations give indicative but important constraints on its values to explore [74]. A rigorous analysis of the divergence shows that it cannot be removed, at most, it can be shifted to a range of values that does not affect the analysis of interest. This point will be revised when the cosmographic parameter priors are discussed.

6.4 The $f(z)$ CDM approach: connecting the Λ CDM model with cosmography

Let us now move beyond the standard cosmography as introduced in the previous sections, which we refer to hereafter as *vanilla*, and introduce the possibility of considering a cosmographic series to parameterize the dark energy contribution to the total energy density. In other words, the cosmographic series, here, is not used to parameterize the evolution of the universe in its entirety but it is placed within a cosmological model in view of describing the dark energy contribution. In the following picture, the analysis of cosmographic parameters is required to give information on cosmic expansion and then on dark energy. Furthermore, the approach allows the use of both early and late time data to constrain the evolution of the universe at all scales. In this way, it is not necessary to fix the values of cosmological parameters, i.e., matter density, as it is necessary to do in the standard cosmographic analyses, but it can be left as a free parameter to be restricted with the data at the same time as the deceleration and jerk values. This approach has been proposed in reference [74], assuming a background evolution equation as:

$$H(z) = H_0 \sqrt{\Omega_k(1+z)^2 + \Omega_m(1+z)^3 + \Omega_r(1+z)^4 + \Omega_f P_{nm}(z)}, \quad (6.19)$$

with $\Omega_k + \Omega_m + \Omega_r + \Omega_f = 1$ and $P_{nm}(z)$ the chosen Padé series, as introduced in section 6.3. Alternatively, one can avoid to take a specific form and reconstruct the function with the data, as shown in [126].

While in the *vanilla* cosmography the whole background evolution is given by the Padé approximation of equations (6.12)-(6.14) in equation (6.19), $H(z)$ is given by the evolution of the cosmological fluids and only the dark energy density dependence with redshift is parameterized by the Padé series, weighted by the density Ω_f . This makes it possible to capture the behavior of interest, eliminating the degeneracy between cosmographic parameters and the matter density, which here evolves as predicted by the standard cosmological model. Thus,

the cosmographic parameters of the $f(z)$ CDM approach are different from those of *vanilla* cosmography. The relation between the *vanilla* q_0 and j_0 , and those constrained by equation (6.19) (hereafter \bar{q}_0 , \bar{j}_0 , etc.) can be determined by equating the derivatives of the two expressions for $H(z)$, that determined through Padé series $P_{nm}(z)$ (see Appendix C) and that from the $f(z)$ CDM approach, given by equation (6.19). This must be done at $z = 0$, because at this point the expressions for the Hubble parameter will be the same:

$$\begin{aligned} \frac{H'(0)}{H_0} &= P'_{nm}(0), \\ \frac{H''(0)}{H_0} &= P''_{nm}(0), \\ &\vdots \\ \frac{H^{(n+m)}(0)}{H_0} &= P^{(n+m)}_{nm}(0), \end{aligned} \tag{6.20}$$

so that, from the first derivatives, it is possible to determine \bar{q}_0 as a function of q_0 , from the second derivatives it is possible to determine \bar{j}_0 as a function of j_0 and the further orders from the higher derivatives. Although the cosmographic and $f(z)$ CDM expressions for $H(z)$ are not the same for all redshifts, at $z = 0$ they are and this allows the equivalent cosmographic coefficients to be determined. As these coefficients are constant and do not depend on z , it is possible to determine them at $z=0$. Specifically, for the first two orders:

$$\bar{q}_0 = \frac{2\Omega_m - 1 - 2q_0}{\Omega_m - 1}, \tag{6.21}$$

$$\bar{j}_0 = \frac{3 + 4q_0^2 + q_0(8 - 12\Omega_m) - 2j_0(\Omega_m - 1) - 12\Omega_m + 10\Omega_m^2}{(\Omega_m - 1)^2}, \tag{6.22}$$

where we can set $\Omega_r = \Omega_k = 0$. These relations are plotted in Figure 6.6, where it is made explicit that the *fiducial* values $q_0 = -0.55$ and $j_0 = 1$ (red line) correspond to $\bar{q}_0 = -1.0$ and $\bar{j}_0 = 1.0$ (black line), respectively.

In addition, the behavior of $\bar{H}(z)$ (which is $H(z)$ in function of \bar{q}_0 , \bar{j}_0 , \bar{s}_0 and \bar{l}_0) as a function of z is presented in Figure 6.7 for three cases: equation (6.19) for P_{21} , P_{22} and P_{32} . Both plots of Figure 6.7 consider $\bar{q}_0 = 1$, $\bar{j}_0 = 1$ and $\bar{s}_0 = \bar{l}_0 = \bar{p}_0 = 0$, and the differences between them is the redshift range considered, $z < 2$ (left) and $z < 10$ (right). It is possible verify from the right-hand side plot that the curves are practically the same until $z = 10$, except for the Taylor expansion which diverges at approximately $z = 6$. In the two redshift ranges, the background considering P_{21} and P_{22} are very similar and we can not see differences between them. Furthermore, the cosmic clock data [117, 118, 119, 120, 121, 122] are plotted

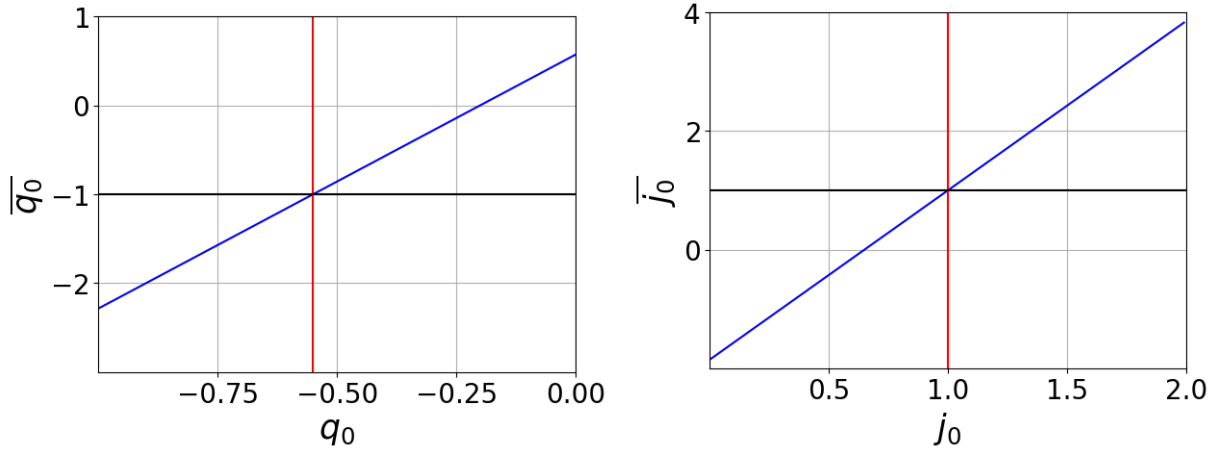


Figure 6.6: The \bar{q}_0 and \bar{j}_0 parameters from $f(z)$ CDM model as functions of the q_0 and j_0 cosmographic parameters, respectively, as described by equations (6.21)-(6.22). Red lines indicate the cosmographic *fiducial* values $q_0 = -0.55$ and $j_0 = 1$, while the black lines stand for the corresponding $f(z)$ CDM parameters, $\bar{q}_0 = -1.00$ and $\bar{j}_0 = 1.00$.

together with the curves and we can verify that all curves agree with the data.

6.5 Parameter constraints with the $f(z)$ CDM approach

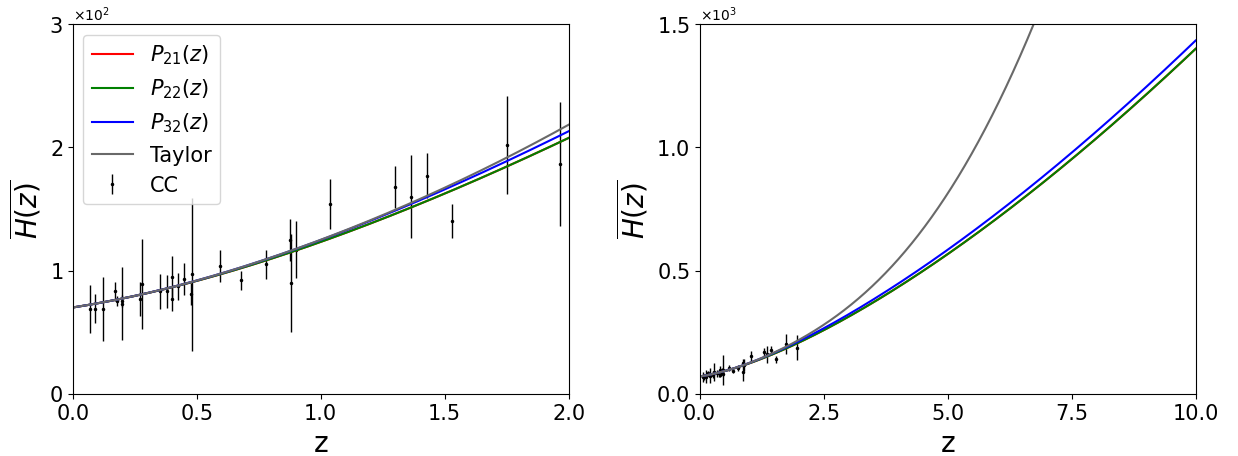


Figure 6.7: $\overline{H}(z)$ is the background evolution given by equation (6.19) and that considers $H_0 = 70 \text{ km s}^{-1} \text{ Mpc}^{-1}$, $\bar{q}_0 = -1$, $\bar{j}_0 = 1$ and $\bar{s}_0 = \bar{l}_0 = 0$. On the left, the plots of $\overline{H}(z)$ as a function of z for three cases: considering P_{21} , P_{22} and P_{32} into equation (6.19). Together with the curves, the cosmic clock data [117, 118, 119, 120, 121, 122] are presented and it is not possible to see the red curve, from P_{21} order, because it is under the green curve, from P_{22} . On the right, the same plots in a larger range of redshift.

Let us illustrate now the data used to estimate the parameters of the $f(z)$ CDM model, as well as the codes adopted in this analysis, and the observational data set employed. As mentioned earlier, the $f(z)$ CDM approach, unlike the *vanilla* cosmography, allows us to use a joint data set of large- and small-scale data. Thus, information from the most robust data releases of several independent measurements is selected, covering from early and late cosmological periods:

- Cosmic Microwave Background Radiation (CMBR) measurements, through the Planck (2018) data [9], considering both temperature power spectra (TT) over the range $\ell \in [2 - 2508]$ and low- ℓ (2 - 29) temperature-polarization cross-correlation spectrum, and HFI polarization EE spectrum at $\ell \leq 29$. It is also considered CMB lensing reconstruction power spectrum [9, 127];
- Baryon Acoustic Oscillation (BAO) distance measurements, using 6dFGS [10], SDSS-MGS [11], and BOSS DR12 [12] surveys;
- Type Ia Supernovae (Pantheon+ sample), that is the latest compilation of 1701 SNIa covering the redshift range [0.01 : 2.3] [128, 129], with objects selection according to SHOES [130]. This sample has a more accurate low redshift data set with respect to the Pantheon catalog and applies more rigid selections on supernova light curves.
- Cosmic Chronometers (CC) data, measurements of the expansion rate $H(z)$ from the relative ages of passively evolving galaxies [13, 14, 15, 16, 17, 18, 19, 20].

The modifications have been implemented in the Boltzmann solver CAMB [131] according to equation (6.19), with Padé approximants given by equations (C.2)-(C.6). The MCMC package for parameter estimation COSMOMC [132] has been also used to constrain the parameters and perform the statistical analysis. Furthermore, the standard set of cosmological parameters are considered free in our analysis: the baryon density ($\Omega_b h^2$), the cold dark matter density ($\Omega_c h^2$), the ratio between the sound horizon and the angular diameter distance at decoupling (Θ_{MC}), the optical depth (τ), the primordial scalar amplitude (A_s), and the primordial spectral index (n_s). To parameterize the current universe evolution, \bar{q}_0 and \bar{j}_0 are also constrained. Note that these parameters are correlated with the cosmographic deceleration and jerk parameters by equations (6.21)-(6.22), with the central fiducial value of $\bar{q}_0 = -1$ and $\bar{j}_0 = 1$. Flat priors over wide ranges of values for each parameter are considered. In particular, \bar{q}_0 and \bar{j}_0 are free to vary into the ranges [-3:0.5] and [-2:4], respectively, that correspond to cosmographic values of $q_0 \in [-1.25 : -0.025]$ and $j_0 \in [-0.05 : 2.05]$ (see Figure 6.6).

	P_{21}	P_{22}	P_{32}
$100\Omega_b h^2$	2.240 ± 0.014	2.244 ± 0.016	2.240 ± 0.014
$\Omega_c h^2$	0.1195 ± 0.0010	0.1187 ± 0.0011	0.1196 ± 0.0012
η	0.9661 ± 0.0038	0.9673 ± 0.0041	0.9656 ± 0.0045
$\overline{q_0}$	-0.86 ± 0.06	-1.06 ± 0.12	-0.70 ± 0.09
$\overline{j_0}$	0.45 ± 0.17	1.71 ± 0.38	0.32 ± 0.24
H_0	67.00 ± 0.76	66.51 ± 0.84	66.45 ± 0.70
σ_8	0.8065 ± 0.0087	0.7980 ± 0.0084	0.8035 ± 0.0100
Ω_m	0.3177 ± 0.0073	0.3207 ± 0.0086	0.3233 ± 0.0069
$\Delta\chi_{\text{eff}}^2$	0	3.1	-0.9

Table 6.1: Mean values and 1σ uncertainties for the cosmological and cosmographic parameters of each model considered in this work. The data set used joint information of CMB TT+TE+EE+lowE+lensing, BAO, Pantheon+ and CC. We fixed $\overline{s_0} = 0$ for P_{21} and P_{22} and $\overline{s_0} = 1.2$ for P_{32} . In the upper section of the table, are some of the most significant primary parameters of our analysis, and in the lower part some of the derived parameters of interest. Here $\Delta\chi_{\text{eff}}^2 = \chi_{\text{eff}}^2(P_{nm}) - \chi_{\text{eff}}^2(P_{21})$.

For such prior ranges, a reasonable stability in Padé’s coefficients for the P_{32} approximation was achieved, assuming $\overline{s_0} = 1.2$. Indeed, by fixing such a value, it is possible to remove the divergences shown in Figure 6.4-6.5. Unfortunately, for the other two Padé parameterizations, it was not possible to improve stability using values of $\overline{s_0}$ other than zero so, for P_{21} and P_{22} , $\overline{s_0} = 0$ in the analysis, as constrained in previous results [74]. This, therefore, marks a point in favor of P_{32} , whose complexity, compared to other parameterizations, allows mathematical divergences to be shifted to a range outside of the one of interest in our analysis.

It is relevant to stress that, as shown in the left column of Figure 6.5, Padé’s coefficients have a rather smooth dependence on s_0 , and the main role of the snap parameter is to shift the divergences at specific values of q_0 and j_0 to values outside the region of interest here. It has been shown in previous works that it is not possible to tightly constrain this parameter because large uncertainties are related to its value [116, 111]. In addition, we tested whether the variation of $\overline{s_0}$ changes the parameter constraints, finding that the value of $\overline{s_0}$ does not affect the value of the cosmological parameters and has the only role of varying the range width of cosmographic values, but not the value of the posterior peak of both $\overline{q_0}$ and $\overline{j_0}$. In the case of a poor choice of the $\overline{s_0}$ value, the confidence level regions of the analysis are not well defined, but still leave the preferred value of the parameters in agreement within 1σ .

Table 6.1 and Figure 6.8 show the constrained parameters considering the joint data set of CMB, BAO, SNe and CC by COSMOMC. Firstly, we note that P_{21} and P_{32} show a

	P_{21}	P_{22}	P_{32}
$\overline{q_0}$	-0.86 ± 0.06	-1.06 ± 0.12	-0.70 ± 0.09
$\overline{j_0}$	0.45 ± 0.17	1.71 ± 0.38	0.32 ± 0.24
Ω_m	0.3177 ± 0.0073	0.3207 ± 0.0086	0.3233 ± 0.0069
q_0	-0.475 ± 0.024	-0.535 ± 0.043	-0.420 ± 0.032
j_0	0.215 ± 0.058	1.20 ± 0.14	0.755 ± 0.081

Table 6.2: Mean values and 1σ uncertainties for the free parameters $\overline{q_0}$ and $\overline{j_0}$ for each Padé approximation considered in this work and the corresponding cosmographic values, calculated using the relations given by equations (6.21)-(6.22).

similar behavior, leading to constraints $\overline{q_0} > -1$ and $\overline{j_0} < 1$, whereas P_{22} prefers more negative deceleration parameter values and higher jerk. This is fully compatible with previous constraints of P_{22} using CMBR data [74], where the main differences between that analysis and the present one is the use of a H_0 prior there, given by the Riess et al. (2019) [133] (i.e. $H_0 = 74.03 \pm 1.42 \text{ km s}^{-1} \text{ Mpc}^{-1}$) and the data set considered (here is not only used CMBR data). The consideration of the prior forces results in [74] to be constrained at a more negative deceleration parameter, i.e. $\overline{q_0} = -1.19 \pm 0.10$, which is, in any case, in agreement within 1σ with present results.

It is worth noticing that the mean values for $\overline{q_0}$ and $\overline{j_0}$ of the present analysis correspond to cosmographic q_0 and j_0 values as shown in Table 6.2. This allows us to compare these constraints with previous cosmographic analyses performed by using large scale data, i.e. without including CMBR information. So, although the present data set includes both small and large scale measurements, the results are fully compatible with reference [116], and agree within 2σ with references [114, 134]. As expected, the inclusion of CMBR data gives more control over high order terms, better constraining the term j_0 and limiting it to values below unity, whereas, using only large-scale data does not give a good bound over this term, which is constrained to higher values with higher uncertainties. This is also true for higher order parameters, which are often associated with an error higher than their mean value or are not bound at all [134]. Trying to leave these parameters unconstrained, in MCMC analysis, not only does not bring any interesting constraints but also risks the oversample of the model.

6.6 Overview

In this analysis, cosmography is used to describe the current acceleration of the Universe beyond the Λ CDM model. Specifically, we consider the $f(z)$ CDM model, where radiation

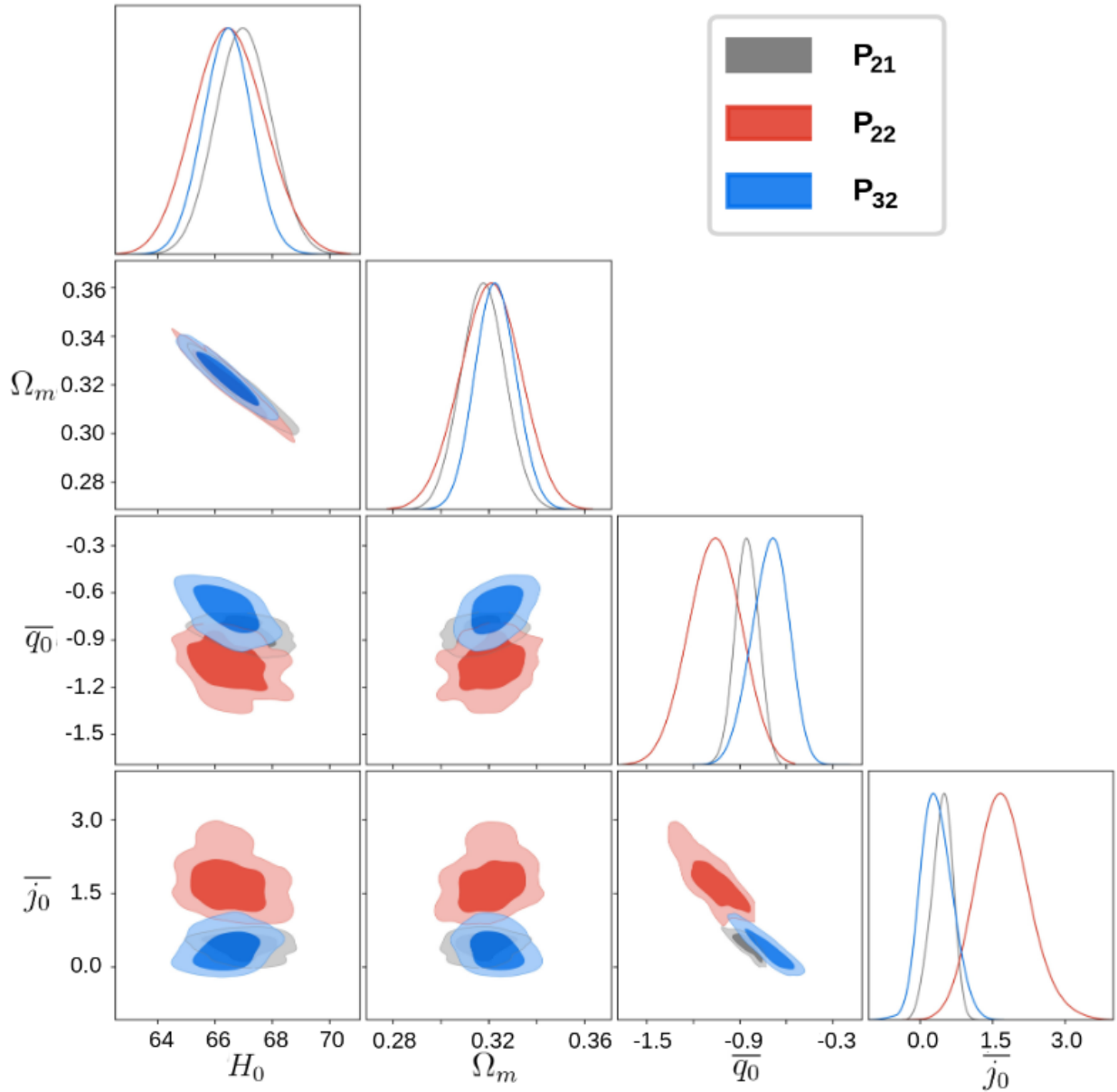


Figure 6.8: Posterior distributions for the cosmological and cosmographic parameters of the $f(z)$ CDM model with background evolution given by equation (6.19), considering $f(z)$ given by P_{32} , P_{22} , P_{21} Padé approximations.

and matter evolution are described as in the standard cosmological model and the energy density of dark energy is parameterized with a Padé cosmographic series, as in equation (6.19), without assuming any specific redshift evolution for this component. This allows us to constrain the model directly by data at all scales, i.e. both CMBR and late time data. The combination of these data sets allows us to simultaneously constrain the cosmographic parameters with late time data, matter density (usually fixed in the *vanilla* cosmography), and CMBR information. It is important to emphasize that our Padé cosmography parameterization only describes the behavior of dark energy, leaving matter and radiation to evolve in their standard way. The present values of cosmographic parameters can be traced back to the *vanilla* ones using equations (6.21)-(6.22) and the analysis shows that, using both late and early times data, it is possible to constrain cosmographic parameters up to the third order with significant accuracy. In this context, the CMBR contribute significantly to the constraint of the jerk parameter, improving the accuracy with respect to the case where only late time measurements are used [116, 114, 134].

Here three different Padé's parameterizations have been analyzed, namely P_{32} , P_{22} and P_{21} . P_{32} and P_{21} are the most quoted in the literature, as the difference in order between the numerator and denominator improves the convergence of the series at high redshifts. On the other hand, the second is less stable but widely used in the literature [74, 111, 126, 123, 114]. We considered it for the sake of completeness of the analysis in view of giving a final answer to the question: *Which is the best choice for Padé series?*

We showed that constraints on the cosmographic parameters of the P_{22} series show some differences with respect to the other two choices (see Table 6.1 and 6.2), leading to larger values of j_0 . On the other hand, a similar behavior is seen for P_{21} and P_{32} , as expected [116]. P_{21} is quite simple, converges for high redshifts and shows similar results even using higher orders, such as P_{32} . However, it shows singularities that cannot be eliminated (see Figure 6.4-6.5). The greater complexity of the P_{32} series manages to stem the problem by shifting the values of s_0 , which can diverge to values not interesting for the analysis. This means a larger explored parameter region and greater rigorous MCMC analysis. For this reason, the conclusion is that the answer depends of what is more relevant for the analysis, a simple parameterization function or a larger region of parameter exploration. In this work, is more relevant to have a good region to explore the parameters to ensure that they are well constrained.

7 | Conclusions

This work explores some possible sources of systematic errors that can affect the determination of the Hubble constant. The first part of the analysis focuses on investigating the sources of error associated with the analysis and modeling of data used as input for the cosmic distance ladder. The second part of the analysis aims to investigate whether the tension in the Hubble constant could have as its origin an incorrect description of the background evolution of the Universe. Some background evolution models are then studied, and a hybrid approach involving the standard cosmological model and cosmography was proposed and tested.

In Chapter 3, we presented the properties of SH0ES and Pantheon+ datasets and validated the analyses tools by recovering results of the literature. Table 3.1 is an illustrative example of the agreement of our results with the original work. Then, we considered a new data sample that mixes cepheids and ancillary data from SH0ES 31 with high quality supernovae data from Pantheon+ 98. Such a selection and merge procedure allowed us to access SNeIa ancillary data in the form of redshift, color and stretch. The merged sample was also validated by performing a least squares fit of distance ladder parameters, as can be seen, for example, in Table 3.4.

In Chapter 4, a methodical study of the response of the cosmic distance ladder to biases introduced on key parts of its rungs was done. Particular attention was given to the impact on the Hubble constant H_0 and on the absolute magnitude of SNeIa M_B . We showed that these two parameters are particularly sensitive to SNeIa magnitude biases that are non-uniform across the second and third rungs of the ladder (see Figures 4.1, 4.2 and 4.3). When systematic shifts on the SNeIa magnitudes are the same for calibration and Hubble flow objects, they are completely absorbed by the supernovae absolute magnitude (see Figure 4.4).

On the other hand, the systematic errors inserted into the metallicity data of the cepheids do not affect the value of H_0 , regardless of their magnitudes, as can be seen in Figure 4.5. This is because the cepheid metallicity standardization coefficient Z_W is able to fully absorb the bias on [O/H]. To be precise, except for Z_W , all the remaining parameters of the ladder are essentially insensitive to the absolute scale of cepheid metallicities. At the end of Chapter 4, in section 4.1, we have also investigated the impact of neglecting correlations in the data sample. A simplified test was performed by generating synthetic data samples with a degree of correlation fully consistent with the one observed in the real SH0ES data

set, and then reconstructed under the hypothesis of complete independence of data points. In that particular case, no statistically significant bias was observed in the fitted parameters, but their uncertainties turned up to be underestimated (see Table [4.6](#)).

The systematic errors associated with the modeling of the data, studied in Chapter [5](#), also indicate interesting lines of investigation for the solution of the Hubble constant tension. As can be seen on Table [5.1](#), we were unable to reproduce with real data claims in the literature, more precisely, those presented in Wojtak et al. (2022) [\[101\]](#) that the distance ladder-based value of H_0 can be made consistent with the CMB-based value by extending the ladder parameters in such a way as to allow different SNeIa color slopes in the calibration (β_{cal}) and Hubble flow (β) samples in the presence of a non-standard ($c_{\text{ref}} \neq 0$) reference color. So far, our fits show that the two fitted color slopes are consistent with each other within uncertainties and no reference color is found that leads to the aforementioned consistency of Hubble parameters. In the second part, we have used synthetic samples to discard the hypothesis that a data set with covariance similar to SH0ES did not have the resolution to distinguish a color slope step $\Delta\beta = \beta_{\text{cal}} - \beta = 4.57 - 3.09 = 1.48$. The most interesting feature of the controlled test was that for a synthetic dataset with $H_0 = 67.36 \text{ km s}^{-1} \text{ Mpc}^{-1}$, $\beta_{\text{cal}} = 4.57$, $\beta = 3.09$ and $c_{\text{ref}} = -0.13$, in case the fit is performed with a single color slope, the fitted value of H_0 becomes consistent with the SN-based value (see Table [5.2](#)). This is fully consistent with Wojtak et al. (2022) claims. Since there are differences in the datasets, covariance matrices and inference methods (we use a least squares estimator, whereas W22 samples a likelihood where the covariance matrix itself is also sampled), this line of investigation will keep being explored by us in the near future. We also plan to open a new investigation branch focused on the physical mechanisms behind a possible evolution (redshift dependence) of color slopes.

Finally, some theoretical models for the evolution of the Universe are reviewed in Chapter [6](#). A hybrid model combining the Λ CDM model and cosmography is proposed, in which the cosmographic part is parameterized by three orders of the Padé series: P_{21} , P_{22} and P_{32} . The models considering these three orders are analyzed, using data from the cosmic microwave background radiation, acoustic baryonic oscillations, cosmic clocks and supernovae, but none of them is able to solve the tension, as can be seen in Table [6.1](#) and Figure [6.8](#). However, it is possible to state that among the orders of the Padé series studied, the most reliable is P_{32} , because it is possible to eliminate the divergences of the model during the restriction of the cosmological parameters, whereas with the others it is not. The content of this chapter is based on the work Petreca et al. (2024) [\[103\]](#).

A | Data covariance matrix

The data covariance matrix \mathbf{C} of the objects belonging to the cosmic distance ladder used in Riess et al. (2022) is non-trivial, because there are common sources of uncertainty between the data of cepheids in the first rung and also between the supernovae from the calibration and the Hubble flow sample:

$$\mathbf{C} = \begin{pmatrix} \sigma_{\text{tot},1}^2 & \dots & Z_{\text{cov}} & Z_{\text{cov}} & 0 & 0 & 0 & 0 & \dots & 0 & 0 & 0 & 0 & 0 & 0 & 0 & \dots & 0 \\ \dots & \dots & \dots & \dots & \dots & \dots & \dots & \dots & \dots & \dots & \dots & \dots & \dots & \dots & \dots & \dots & \dots & \dots \\ Z_{\text{cov}} & \dots & \sigma_{\text{tot,nh}}^2 & Z_{\text{cov}} & 0 & 0 & 0 & 0 & \dots & 0 & 0 & 0 & 0 & 0 & 0 & 0 & \dots & 0 \\ \hline Z_{\text{cov}} & \dots & Z_{\text{cov}} & \sigma_{\text{tot,N4258}}^2 & 0 & 0 & 0 & 0 & \dots & 0 & 0 & 0 & 0 & 0 & 0 & 0 & \dots & 0 \\ 0 & \dots & 0 & 0 & \sigma_{\text{tot,M31}}^2 & 0 & 0 & 0 & \dots & 0 & 0 & 0 & 0 & 0 & 0 & 0 & \dots & 0 \\ 0 & \dots & 0 & 0 & 0 & \sigma_{\text{tot,LMC}}^2 & 0 & 0 & \dots & 0 & 0 & 0 & 0 & 0 & 0 & 0 & \dots & 0 \\ 0 & \dots & 0 & 0 & 0 & 0 & \sigma_{\text{tot,SMC}}^2 & 0 & \dots & 0 & 0 & 0 & 0 & 0 & 0 & 0 & \dots & 0 \\ \hline 0 & \dots & 0 & 0 & 0 & 0 & 0 & \sigma_{m_B,1}^2 & \dots & \text{SN}_{\text{cov}} & 0 & 0 & 0 & 0 & 0 & \text{SN}_{\text{cov}} & \dots & \text{SN}_{\text{cov}} \\ \dots & \dots & \dots & \dots & \dots & \dots & \dots & \dots & \dots & \dots & \dots & \dots & \dots & \dots & \dots & \dots & \dots & \dots \\ 0 & \dots & 0 & 0 & 0 & 0 & 0 & \text{SN}_{\text{cov}} & \dots & \sigma_{m_B,\text{ncc}}^2 & 0 & 0 & 0 & 0 & 0 & \text{SN}_{\text{cov}} & \dots & \text{SN}_{\text{cov}} \\ \hline 0 & \dots & 0 & 0 & 0 & 0 & 0 & 0 & \dots & 0 & \sigma_{\text{HST}}^2 & 0 & 0 & 0 & 0 & 0 & \dots & 0 \\ 0 & \dots & 0 & 0 & 0 & 0 & 0 & 0 & \dots & 0 & 0 & \sigma_{\text{Gaia}}^2 & 0 & 0 & 0 & 0 & \dots & 0 \\ 0 & \dots & 0 & 0 & 0 & 0 & 0 & 0 & \dots & 0 & 0 & 0 & \sigma_{\text{grnd}}^2 & 0 & 0 & 0 & \dots & 0 \\ 0 & \dots & 0 & 0 & 0 & 0 & 0 & 0 & \dots & 0 & 0 & 0 & 0 & \sigma_{\mu,\text{N4258}}^2 & 0 & 0 & \dots & 0 \\ 0 & \dots & 0 & 0 & 0 & 0 & 0 & 0 & \dots & 0 & 0 & 0 & 0 & 0 & \sigma_{\mu,\text{LMC}}^2 & 0 & \dots & 0 \\ \hline 0 & \dots & 0 & 0 & 0 & 0 & 0 & \text{SN}_{\text{cov}} & \dots & \text{SN}_{\text{cov}} & 0 & 0 & 0 & 0 & 0 & \sigma_{m_B,z,1}^2 & \dots & \text{SN}_{\text{cov}} \\ \dots & \dots & \dots & \dots & \dots & \dots & \dots & \dots & \dots & \dots & \dots & \dots & \dots & \dots & \dots & \dots & \dots & \dots \\ 0 & \dots & 0 & 0 & 0 & 0 & 0 & \text{SN}_{\text{cov}} & \dots & \text{SN}_{\text{cov}} & 0 & 0 & 0 & 0 & 0 & \text{SN}_{\text{cov}} & \dots & \sigma_{m_B,z,\text{nhf}}^2 \end{pmatrix} \quad (\text{A.1})$$

The number of cepheid hosts is nh, the number of SNeIa in these hosts is ncc, and the number of SNeIa in the Hubble flow is nhf. σ_{HST} and σ_{Gaia} denote the uncertainties in $M_{H,1,\text{Gaia}}^W$ and $M_{H,1,\text{HST}}^W$, while σ_{grnd} denotes the uncertainty in ground-based photometry. $\sigma_{\text{tot},1}$ represents a $n \times n$ covariance matrix for the n cepheids in the first host:

$$\sigma_{\text{tot},i} = \begin{pmatrix} \sigma_{\text{tot},1,1} & \dots & C_{1,1,n,\text{bkgd}} \\ \dots & \dots & \dots \\ C_{1,1,n,\text{bkgd}} & \dots & \sigma_{\text{tot},1,n} \end{pmatrix} \quad (\text{A.2})$$

in which $\sigma_{\text{tot},1,1}$ is the uncertainty of each cepheid. Furthermore, $C_{i,j,k,\text{bkgd}}$ is the background covariance:

$$C_{i,j,k,\text{bkgd}} = 0.2^2 (\text{bkgd}_{i,j}) (\text{bkgd}_{i,k}). \quad (\text{A.3})$$

According to [31], by inserting artificial stars in the neighborhood of each cepheid image, it is possible to estimate the sky background and test the cepheid photometry. Through this procedure, a systematic uncertainty of 20% was obtained for the background (in units of the

cepheid magnitude correction) as the covariance “error floor” of any pair of cepheids, j , k in the same i th host. In equation (A.3), the term “bkgd” represents the change in cepheid magnitude due to the addition of the mean level of the crowded background from unresolved sources derived from the artificial stars [31].

The term SN_{cov} is the covariance between SNe and Z_{cov} is the metallicity covariance given by:

$$Z_{\text{cov}} = Z_W^2 ([\text{O}/\text{H}]_{i,\text{avg}} - [\text{O}/\text{H}]_{i,\text{PP04}})([\text{O}/\text{H}]_{j,\text{avg}} - [\text{O}/\text{H}]_{j,\text{PP04}}). \quad (\text{A.4})$$

where period uncertainties are comparatively negligible [135] and PP04 indicates Pettini & Pagel calibration [136]. The mean difference of 0.05 dex between the average and PP04 scale represents a systematic uncertainty in the abundance scale, propagated here in the covariance matrix.

B | Complete tables and plots

Here are shown all plots and data about parameters in function of the systematic errors.

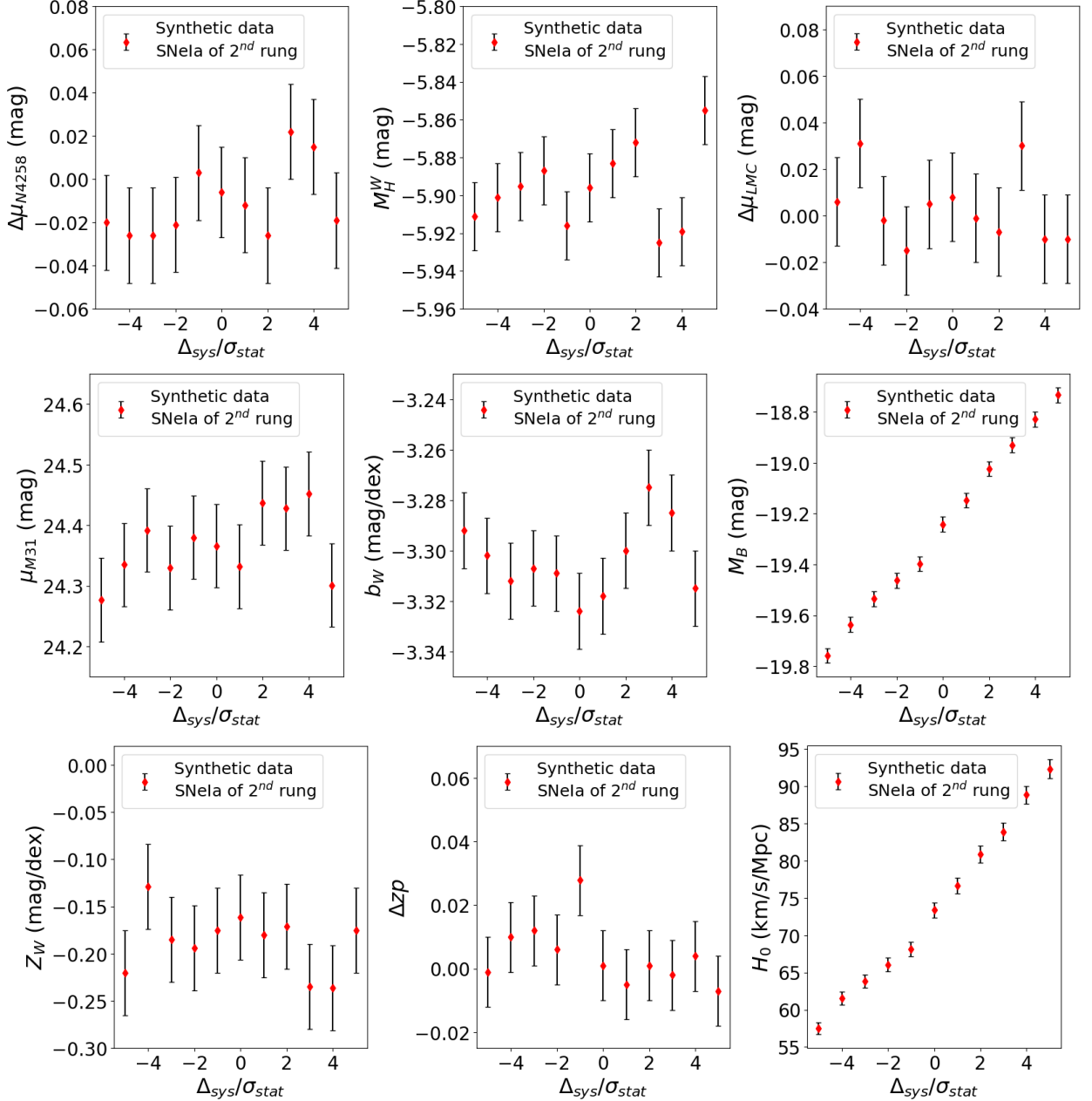


Figure B.1: All fitted parameters from the cosmic distance ladder as a function of the magnitude of a hypothetical bias on the apparent magnitudes of 2nd rung synthetic SNeIa. The systematic errors are given in units of the statistical fluctuation $\sigma_{\text{stat}} = 0.098$ mag.

B | Appendix: Complete tables and plots

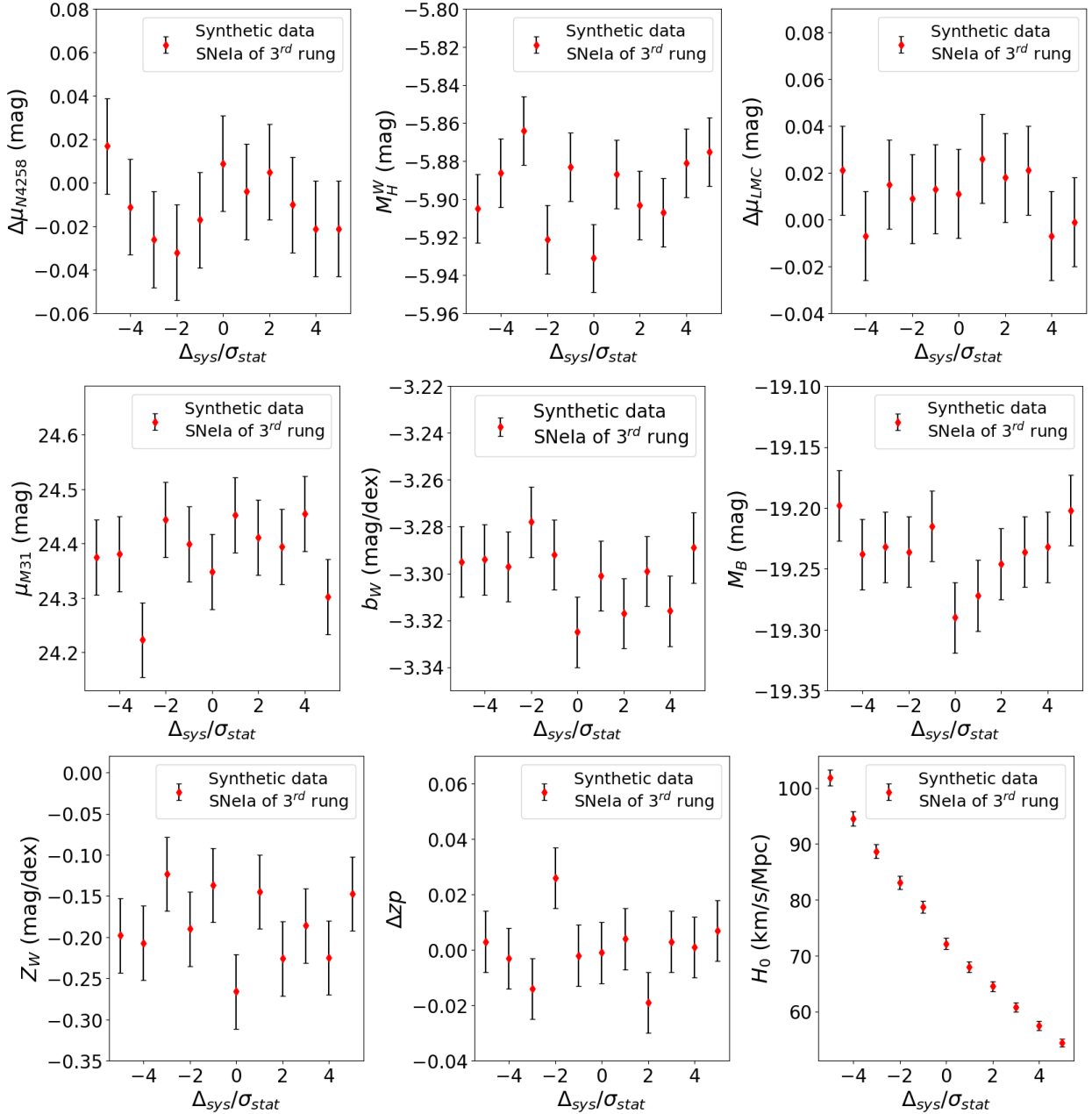


Figure B.2: All fitted parameters from the cosmic distance ladder as a function of the magnitude of a hypothetical bias on the apparent magnitudes of 3rd rung synthetic SNeIa. The systematic errors are given in units of the statistical fluctuation $\sigma_{\text{stat}} = 0.135$ mag.

$\Delta_{\text{sys}}/\sigma_{\text{stat}}$	$H_0 \pm \sigma_{H_0}$ ($\text{km s}^{-1} \text{Mpc}^{-1}$)	$\Delta\mu_{N4258} \pm \sigma_{\Delta\mu_{N4258}}$ (mag)	$M_H^W \pm \sigma_{M_H^W}$ (mag)	$\Delta\mu_{LMC} \pm \sigma_{\Delta\mu_{LMC}}$ (mag)	$\mu_{M31} \pm \sigma_{\mu_{M31}}$ (mag)	$b_W \pm \sigma_{b_W}$ (mag/dex)	$M_B \pm \sigma_{M_B}$ (mag)	$Z_W \pm \sigma_{Z_W}$ (mag/dex)	$\Delta z_p \pm \sigma_{\Delta z_p}$
-	-	-	-	-	-	-	-	-	-
-5	57.48 ± 0.79	-0.020 ± 0.022	-5.911 ± 0.018	0.006 ± 0.019	24.277 ± 0.069	-3.292 ± 0.015	-19.758 ± 0.029	-0.220 ± 0.045	-0.001 ± 0.011
-4	61.55 ± 0.85	-0.026 ± 0.022	-5.901 ± 0.018	0.031 ± 0.019	24.335 ± 0.069	-3.302 ± 0.015	-19.636 ± 0.029	-0.129 ± 0.045	0.010 ± 0.011
-3	63.85 ± 0.88	-0.026 ± 0.022	-5.895 ± 0.018	-0.002 ± 0.019	24.392 ± 0.069	-3.312 ± 0.015	-19.535 ± 0.029	-0.185 ± 0.045	0.012 ± 0.011
-2	66.05 ± 0.91	-0.021 ± 0.022	-5.887 ± 0.018	-0.015 ± 0.019	24.330 ± 0.069	-3.307 ± 0.015	-19.463 ± 0.029	-0.194 ± 0.045	0.006 ± 0.011
-1	68.13 ± 0.94	0.003 ± 0.022	-5.916 ± 0.018	0.005 ± 0.019	24.380 ± 0.069	-3.309 ± 0.015	-19.398 ± 0.029	-0.175 ± 0.045	0.028 ± 0.011
0	73.37 ± 1.01	-0.006 ± 0.021	-5.896 ± 0.018	0.008 ± 0.019	24.366 ± 0.069	-3.324 ± 0.015	-19.242 ± 0.029	-0.161 ± 0.045	0.001 ± 0.011
1	76.62 ± 1.06	-0.012 ± 0.022	-5.883 ± 0.018	-0.001 ± 0.019	24.332 ± 0.069	-3.318 ± 0.015	-19.147 ± 0.029	-0.180 ± 0.045	-0.005 ± 0.011
2	80.87 ± 1.12	-0.026 ± 0.022	-5.872 ± 0.018	-0.007 ± 0.019	24.437 ± 0.069	-3.300 ± 0.015	-19.024 ± 0.029	-0.171 ± 0.045	0.001 ± 0.011
3	83.90 ± 1.16	0.022 ± 0.022	-5.925 ± 0.018	0.030 ± 0.019	24.428 ± 0.069	-3.275 ± 0.015	-18.930 ± 0.029	-0.235 ± 0.045	-0.002 ± 0.011
4	88.83 ± 1.22	0.015 ± 0.022	-5.919 ± 0.018	-0.010 ± 0.019	24.452 ± 0.069	-3.285 ± 0.015	-18.829 ± 0.029	-0.236 ± 0.045	0.004 ± 0.011
5	92.32 ± 1.27	-0.019 ± 0.022	-5.855 ± 0.018	-0.010 ± 0.019	24.301 ± 0.069	-3.285 ± 0.015	-18.734 ± 0.029	-0.175 ± 0.045	-0.007 ± 0.011

Table B.1: Least squares solutions for all fitted parameters from the cosmic distance ladder using synthetic data affected by systematic shifts on the apparent magnitudes of second rung SNeIa with different magnitudes Δ_{sys} , in units of $\sigma_{\text{stat}} = 0.098$ mag.

$\Delta_{\text{sys}}/\sigma_{\text{stat}}$	$H_0 \pm \sigma_{H_0}$ ($\text{km s}^{-1} \text{Mpc}^{-1}$)	$\Delta\mu_{N4258} \pm \sigma_{\Delta\mu_{N4258}}$ (mag)	$M_H^W \pm \sigma_{M_H^W}$ (mag)	$\Delta\mu_{LMC} \pm \sigma_{\Delta\mu_{LMC}}$ (mag)	$\mu_{M31} \pm \sigma_{\mu_{M31}}$ (mag)	$b_W \pm \sigma_{b_W}$ (mag/dex)	$M_B \pm \sigma_{M_B}$ (mag)	$Z_W \pm \sigma_{Z_W}$ (mag/dex)	$\Delta z_p \pm \sigma_{\Delta z_p}$
-	-	-	-	-	-	-	-	-	-
-5	101.83 ± 1.40	0.017 ± 0.022	-5.905 ± 0.018	0.021 ± 0.019	24.375 ± 0.069	-3.295 ± 0.015	-19.198 ± 0.029	-0.198 ± 0.045	0.003 ± 0.011
-4	94.50 ± 1.30	-0.011 ± 0.022	-5.886 ± 0.018	-0.007 ± 0.019	24.381 ± 0.069	-3.294 ± 0.015	-19.238 ± 0.029	-0.207 ± 0.045	-0.014 ± 0.011
-3	88.65 ± 1.22	-0.026 ± 0.022	-5.864 ± 0.018	0.015 ± 0.019	24.223 ± 0.069	-3.297 ± 0.015	-19.232 ± 0.029	-0.123 ± 0.045	-0.014 ± 0.011
-2	83.11 ± 1.15	-0.032 ± 0.022	-5.921 ± 0.018	0.009 ± 0.019	24.444 ± 0.069	-3.278 ± 0.015	-19.236 ± 0.029	-0.190 ± 0.045	0.026 ± 0.011
-1	78.73 ± 1.09	-0.017 ± 0.022	-5.883 ± 0.018	0.013 ± 0.019	24.399 ± 0.069	-3.292 ± 0.015	-19.215 ± 0.029	-0.137 ± 0.045	-0.002 ± 0.011
0	72.15 ± 0.99	0.009 ± 0.022	-5.931 ± 0.018	0.011 ± 0.019	24.348 ± 0.069	-3.325 ± 0.015	-19.290 ± 0.029	-0.266 ± 0.045	-0.001 ± 0.011
1	68.03 ± 0.94	-0.004 ± 0.022	-5.887 ± 0.018	0.026 ± 0.019	24.453 ± 0.069	-3.301 ± 0.015	-19.272 ± 0.029	-0.145 ± 0.045	0.004 ± 0.011
2	64.52 ± 0.89	0.005 ± 0.022	-5.903 ± 0.018	0.018 ± 0.019	24.411 ± 0.069	-3.317 ± 0.015	-19.246 ± 0.029	-0.226 ± 0.045	-0.019 ± 0.011
3	60.75 ± 0.84	-0.010 ± 0.022	-5.907 ± 0.018	0.021 ± 0.019	24.395 ± 0.069	-3.299 ± 0.015	-19.236 ± 0.029	-0.186 ± 0.045	0.003 ± 0.011
4	57.49 ± 0.79	-0.021 ± 0.022	-5.881 ± 0.018	-0.007 ± 0.019	24.455 ± 0.069	-3.316 ± 0.015	-19.232 ± 0.029	-0.225 ± 0.045	0.001 ± 0.011
5	54.43 ± 0.75	-0.021 ± 0.022	-5.875 ± 0.018	-0.001 ± 0.019	24.302 ± 0.069	-3.289 ± 0.015	-19.202 ± 0.029	-0.147 ± 0.045	0.007 ± 0.011

Table B.2: Least squares solutions for all fitted parameters from the cosmic distance ladder using synthetic data affected by systematic shifts on the apparent magnitudes of third rung SNeIa with different magnitudes Δ_{sys} , in units of $\sigma_{\text{stat}} = 0.135$ mag.

B | Appendix: Complete tables and plots

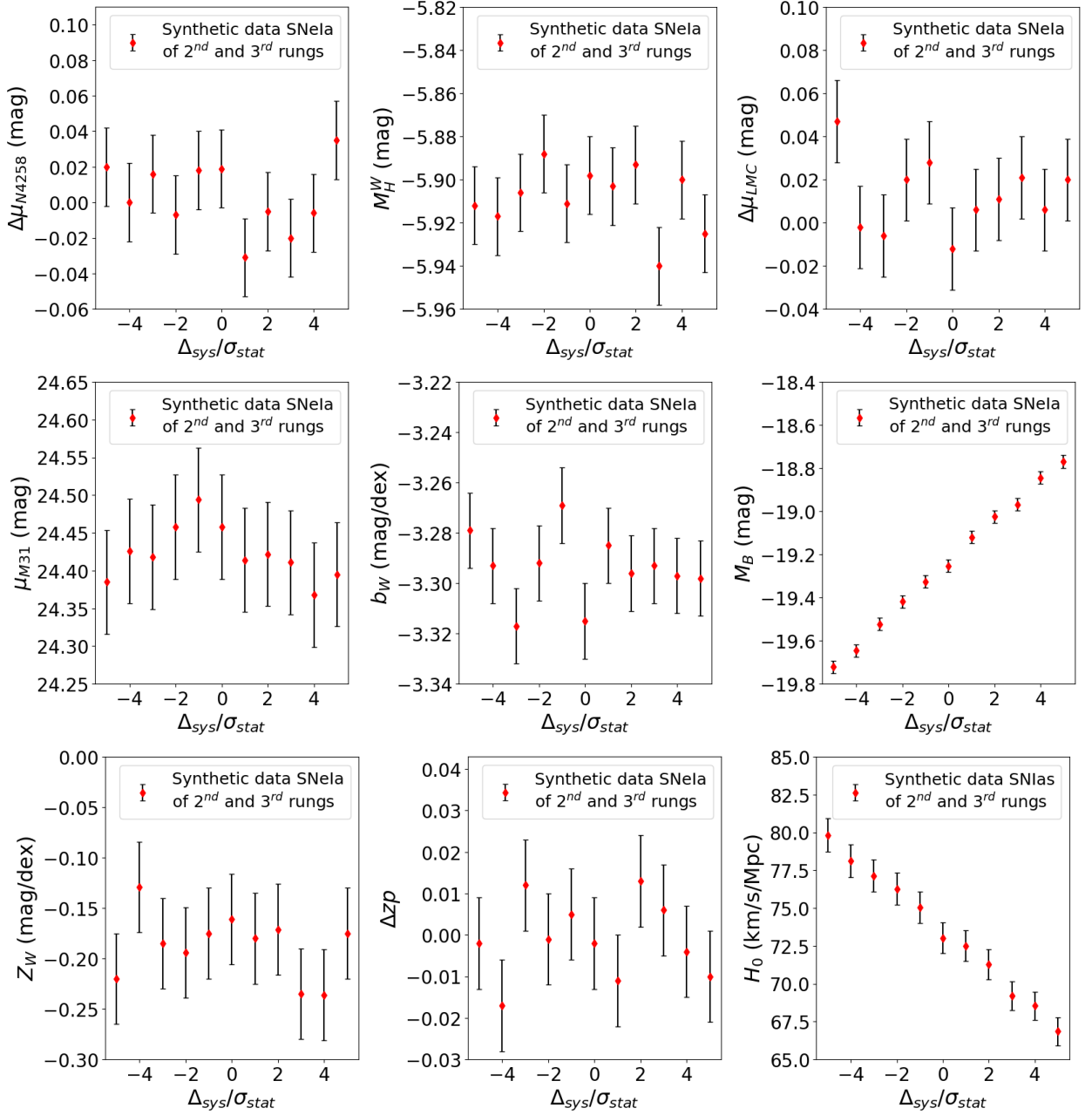


Figure B.3: All fitted parameters from the cosmic distance ladder as a function of the magnitude of a hypothetical bias on the apparent magnitudes of 2nd and 3rd rung synthetic SNeIa. The systematic errors are given in units of the statistical fluctuations $\sigma_{\text{stat}} = 0.098$ mag and $\sigma_{\text{stat}} = 0.135$ mag, respectively.

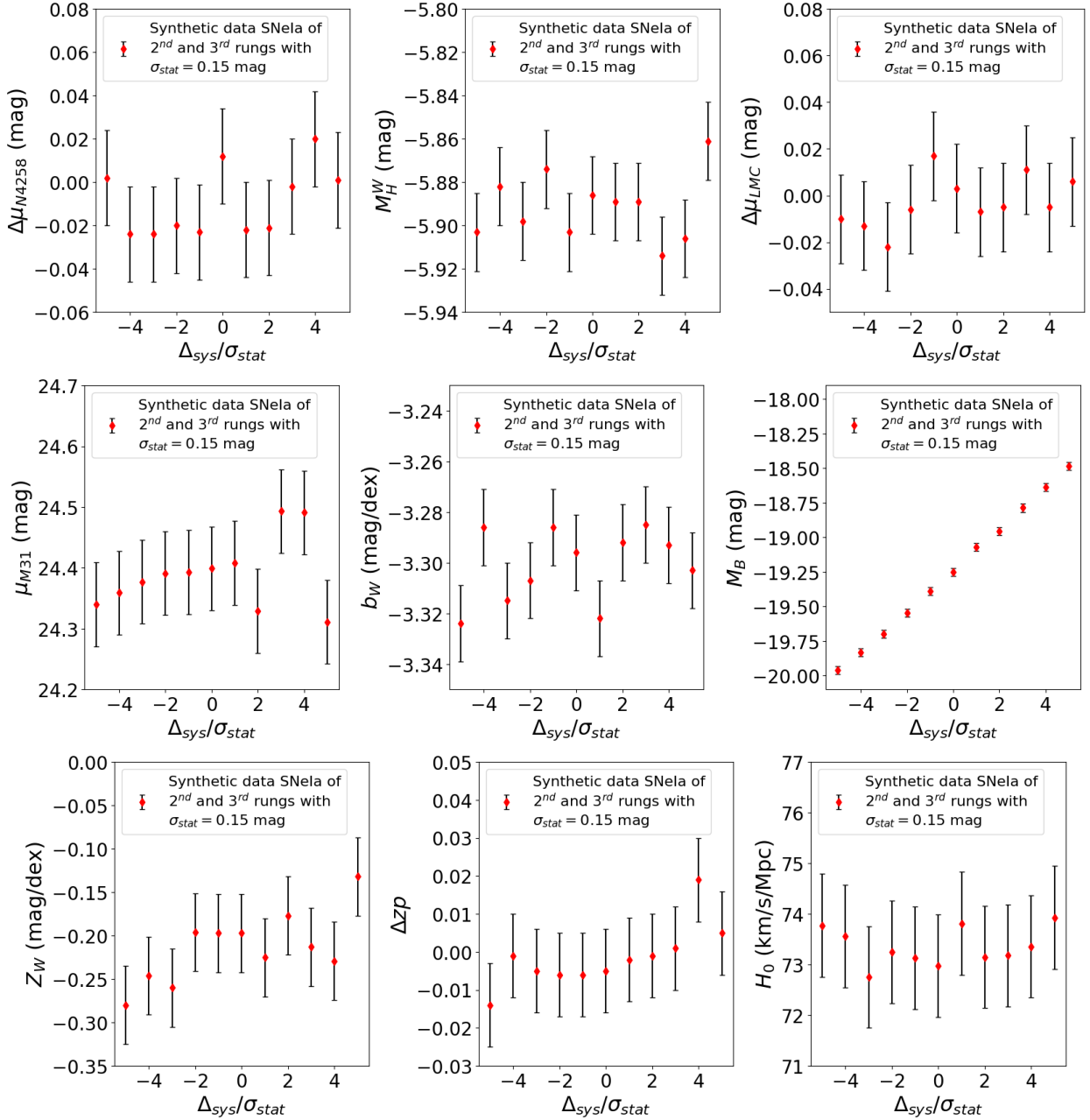


Figure B.4: All fitted parameters from the cosmic distance ladder as a function of the magnitude of a hypothetical bias on the apparent magnitudes of 2nd and 3rd rung synthetic SNeIa. The systematic errors are given in units of the statistical fluctuation $\sigma_{\text{stat}} = 0.15$ mag.

$\Delta_{\text{sys}}/\sigma_{\text{stat}}$	$H_0 \pm \sigma_{H_0}$ ($\text{km s}^{-1} \text{Mpc}^{-1}$)	$\Delta\mu_{N4258} \pm \sigma_{\Delta\mu_{N4258}}$ (mag)	$M_H^W \pm \sigma_{M_H^W}$ (mag)	$\Delta\mu_{LMC} \pm \sigma_{\Delta\mu_{LMC}}$ (mag)	$\mu_{M31} \pm \sigma_{\mu_{M31}}$ (mag)	$b_W \pm \sigma_{b_W}$ (mag/dex)	$M_B \pm \sigma_{M_B}$ (mag)	$Z_W \pm \sigma_{Z_W}$ (mag/dex)	$\Delta z_p \pm \sigma_{\Delta z_p}$
-5	79.82 ± 1.10	0.020 ± 0.022	-5.912 ± 0.018	0.047 ± 0.019	24.385 ± 0.069	-3.279 ± 0.015	-19.722 ± 0.029	-0.128 ± 0.045	-0.002 ± 0.011
-4	78.12 ± 1.08	0.000 ± 0.022	-5.917 ± 0.018	-0.002 ± 0.019	24.426 ± 0.069	-3.293 ± 0.015	-19.646 ± 0.029	-0.287 ± 0.045	-0.017 ± 0.011
-3	77.15 ± 1.06	0.016 ± 0.022	-5.906 ± 0.018	-0.006 ± 0.019	24.418 ± 0.069	-3.317 ± 0.015	-19.523 ± 0.029	-0.215 ± 0.045	0.012 ± 0.011
-2	76.28 ± 1.05	-0.007 ± 0.022	-5.888 ± 0.018	0.020 ± 0.019	24.458 ± 0.069	-3.292 ± 0.015	-19.419 ± 0.029	-0.181 ± 0.045	-0.001 ± 0.011
-1	75.06 ± 1.03	0.018 ± 0.022	-5.911 ± 0.018	0.028 ± 0.019	24.494 ± 0.069	-3.269 ± 0.015	-19.326 ± 0.029	-0.151 ± 0.045	0.005 ± 0.011
0	73.03 ± 1.01	0.019 ± 0.022	-5.898 ± 0.018	-0.012 ± 0.019	24.458 ± 0.069	-3.315 ± 0.015	-19.253 ± 0.029	-0.229 ± 0.045	-0.002 ± 0.011
1	72.52 ± 1.00	-0.031 ± 0.022	-5.903 ± 0.018	0.006 ± 0.019	24.414 ± 0.069	-3.285 ± 0.015	-19.120 ± 0.029	-0.266 ± 0.045	-0.011 ± 0.011
2	71.29 ± 0.98	-0.005 ± 0.022	-5.893 ± 0.018	0.011 ± 0.019	24.422 ± 0.069	-3.296 ± 0.015	-19.025 ± 0.029	-0.166 ± 0.045	0.013 ± 0.011
3	69.19 ± 0.95	-0.020 ± 0.022	-5.940 ± 0.018	0.021 ± 0.019	24.411 ± 0.069	-3.293 ± 0.015	-18.968 ± 0.029	-0.222 ± 0.045	0.006 ± 0.011
4	68.54 ± 0.95	-0.006 ± 0.022	-5.900 ± 0.018	0.006 ± 0.019	24.368 ± 0.069	-3.297 ± 0.015	-18.844 ± 0.029	-0.218 ± 0.045	-0.004 ± 0.011
5	66.86 ± 0.92	0.035 ± 0.022	-5.925 ± 0.018	0.020 ± 0.019	24.395 ± 0.069	-3.298 ± 0.015	-18.769 ± 0.029	-0.226 ± 0.045	-0.010 ± 0.011

Table B.3: Least squares solutions for all fitted parameters from the cosmic distance ladder using synthetic data affected by systematic shifts on the apparent magnitudes of second and third rung SNIa with different magnitudes Δ_{sys} , in units of $\sigma_{\text{stat}} = 0.098$ mag and $\sigma_{\text{stat}} = 0.135$ mag, respectively.

$\Delta_{\text{sys}}/\sigma_{\text{stat}}$	$H_0 \pm \sigma_{H_0}$ ($\text{km s}^{-1} \text{Mpc}^{-1}$)	$\Delta\mu_{N4258} \pm \sigma_{\Delta\mu_{N4258}}$ (mag)	$M_H^W \pm \sigma_{M_H^W}$ (mag)	$\Delta\mu_{LMC} \pm \sigma_{\Delta\mu_{LMC}}$ (mag)	$\mu_{M31} \pm \sigma_{\mu_{M31}}$ (mag)	$b_W \pm \sigma_{b_W}$ (mag/dex)	$M_B \pm \sigma_{M_B}$ (mag)	$Z_W \pm \sigma_{Z_W}$ (mag/dex)	$\Delta z_p \pm \sigma_{\Delta z_p}$
-5	73.77 ± 1.02	0.002 ± 0.022	-5.903 ± 0.018	-0.010 ± 0.019	24.340 ± 0.069	-3.324 ± 0.015	-19.962 ± 0.029	-0.280 ± 0.045	-0.014 ± 0.011
-4	73.56 ± 1.01	-0.024 ± 0.022	-5.882 ± 0.018	-0.013 ± 0.019	24.359 ± 0.069	-3.286 ± 0.015	-19.833 ± 0.029	-0.246 ± 0.045	-0.001 ± 0.011
-3	72.76 ± 1.00	-0.024 ± 0.022	-5.898 ± 0.018	-0.022 ± 0.019	24.377 ± 0.069	-3.315 ± 0.015	-19.697 ± 0.029	-0.260 ± 0.045	-0.005 ± 0.011
-2	73.25 ± 1.01	-0.020 ± 0.022	-5.874 ± 0.018	-0.006 ± 0.019	24.391 ± 0.069	-3.307 ± 0.015	-19.545 ± 0.029	-0.196 ± 0.045	-0.006 ± 0.011
-1	73.13 ± 1.01	-0.023 ± 0.022	-5.903 ± 0.018	0.017 ± 0.019	24.393 ± 0.069	-3.286 ± 0.015	-19.390 ± 0.029	-0.197 ± 0.045	-0.006 ± 0.011
0	72.98 ± 1.01	0.012 ± 0.022	-5.886 ± 0.018	0.003 ± 0.019	24.399 ± 0.069	-3.296 ± 0.015	-19.252 ± 0.029	-0.197 ± 0.045	-0.005 ± 0.011
1	73.81 ± 1.02	-0.022 ± 0.022	-5.889 ± 0.018	-0.007 ± 0.019	24.408 ± 0.069	-3.322 ± 0.015	-19.072 ± 0.029	-0.225 ± 0.045	-0.002 ± 0.011
2	73.15 ± 1.01	-0.021 ± 0.022	-5.889 ± 0.018	-0.005 ± 0.019	24.329 ± 0.069	-3.292 ± 0.015	-18.955 ± 0.029	-0.177 ± 0.045	-0.001 ± 0.011
3	73.18 ± 1.01	-0.002 ± 0.022	-5.914 ± 0.018	0.011 ± 0.019	24.493 ± 0.069	-3.285 ± 0.015	-18.787 ± 0.029	-0.213 ± 0.045	0.001 ± 0.011
4	73.36 ± 1.01	0.020 ± 0.022	-5.906 ± 0.018	-0.005 ± 0.019	24.491 ± 0.069	-3.293 ± 0.015	-18.636 ± 0.029	-0.229 ± 0.045	0.019 ± 0.011
5	73.93 ± 1.02	0.001 ± 0.022	-5.861 ± 0.018	0.006 ± 0.019	24.311 ± 0.069	-3.293 ± 0.015	-18.485 ± 0.029	-0.132 ± 0.045	0.005 ± 0.011

Table B.4: Least squares solutions for all fitted parameters from the cosmic distance ladder using synthetic data affected by systematic shifts on the apparent magnitudes of second and third rung SNIa with different magnitudes Δ_{sys} , in units of $\sigma_{\text{stat}} = 0.15$ mag.

B | Appendix: Complete tables and plots

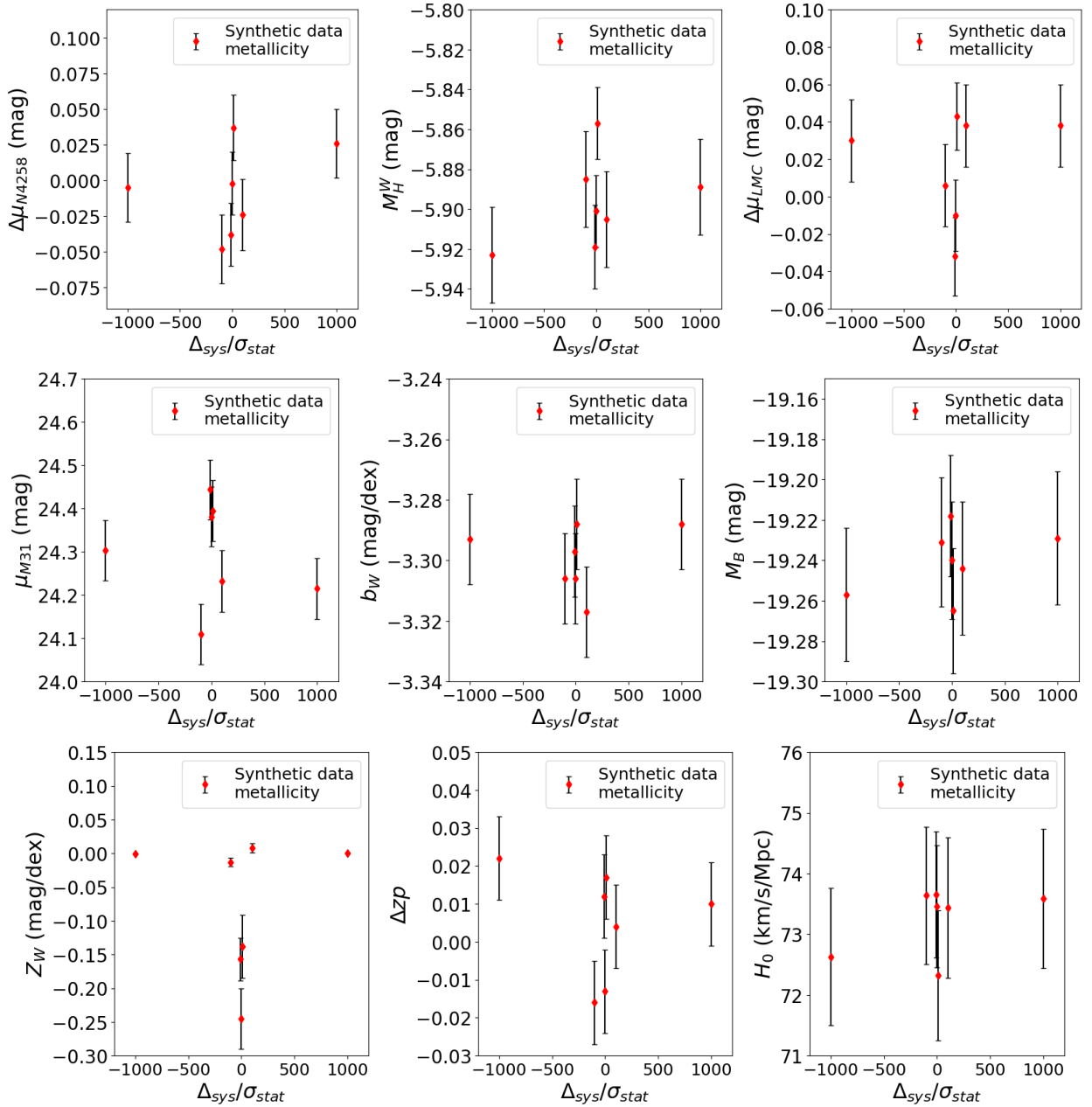


Figure B.5: All fitted parameters from the cosmic distance ladder as a function of the magnitude of a hypothetical bias on the metallicity data of cepheids. The systematic errors are given in units of the statistical fluctuation $\sigma_{\text{stat}} = 0.05$ dex.

$\Delta_{\text{sys}}/\sigma_{\text{stat}}$	$H_0 \pm \sigma_{H_0}$ ($\text{km s}^{-1} \text{Mpc}^{-1}$)	$\Delta\mu_{N4258} \pm \sigma_{\Delta\mu_{N4258}}$ (mag)	$M_H^W \pm \sigma_{M_H^W}$ (mag)	$\Delta\mu_{LMC} \pm \sigma_{\Delta\mu_{LMC}}$ (mag)	$\mu_{M31} \pm \sigma_{\mu_{M31}}$ (mag)	$b_W \pm \sigma_{b_W}$ (mag/dex)	$M_B \pm \sigma_{M_B}$ (mag)	$Z_W \pm \sigma_{Z_W}$ (mag/dex)	$\Delta z_p \pm \sigma_{\Delta z_p}$
-10^4	73.64 ± 1.15	-0.029 ± 0.024	-5.872 ± 0.024	0.049 ± 0.022	24.304 ± 0.070	-3.307 ± 0.015	-19.235 ± 0.033	$-(2.3 \pm 6.7) \times 10^{-5}$	-0.002 ± 0.011
-10^3	72.63 ± 1.13	-0.005 ± 0.024	-5.923 ± 0.024	0.030 ± 0.022	24.303 ± 0.070	-3.293 ± 0.015	-19.257 ± 0.033	$-(7.4 \pm 6.6) \times 10^{-4}$	0.022 ± 0.011
-10^2	73.64 ± 1.13	-0.048 ± 0.024	-5.885 ± 0.024	0.006 ± 0.022	24.109 ± 0.070	-3.306 ± 0.015	-19.231 ± 0.032	-0.013 ± 0.006	-0.016 ± 0.011
-10	73.65 ± 1.04	-0.038 ± 0.022	-5.919 ± 0.021	-0.032 ± 0.021	24.444 ± 0.069	-3.297 ± 0.015	-19.218 ± 0.030	-0.157 ± 0.032	0.012 ± 0.011
0	73.46 ± 1.01	-0.002 ± 0.022	-5.901 ± 0.018	-0.010 ± 0.019	24.381 ± 0.069	-3.306 ± 0.015	-19.240 ± 0.029	-0.245 ± 0.045	-0.013 ± 0.011
10	72.32 ± 1.07	0.037 ± 0.023	-5.857 ± 0.018	0.043 ± 0.018	24.395 ± 0.070	-3.288 ± 0.015	-19.265 ± 0.031	-0.138 ± 0.047	0.017 ± 0.011
10^2	73.44 ± 1.16	-0.024 ± 0.025	-5.905 ± 0.024	0.038 ± 0.022	24.232 ± 0.071	-3.317 ± 0.015	-19.244 ± 0.033	0.008 ± 0.007	0.004 ± 0.011
10^3	73.59 ± 1.15	0.026 ± 0.024	-5.889 ± 0.024	0.038 ± 0.022	24.215 ± 0.070	-3.288 ± 0.015	-19.229 ± 0.033	$-(4.9 \pm 6.8) \times 10^{-4}$	0.010 ± 0.011
10^4	73.52 ± 1.15	-0.010 ± 0.024	-5.881 ± 0.024	0.025 ± 0.022	24.371 ± 0.070	-3.308 ± 0.015	-19.230 ± 0.033	$(7.2 \pm 6.7) \times 10^{-5}$	-0.005 ± 0.011

Table B.5: Least squares solutions for all fitted parameters from the cosmic distance ladder using metallicity data of cepheids affected by systematic shifts with different magnitudes Δ_{sys} , in units of $\sigma_{\text{stat}} = 0.05$ dex.

C | Cosmographic expressions

Here are presented the formulas of luminosity distance and background evolution for the three Padé series plotted in Figures [6.1](#) and [6.3](#), nominally P_{21} , P_{22} and P_{32} .

P_{21} equations of the luminosity distance and the Hubble rate:

$$d_L^{P_{21}}(z) = \frac{cz}{H_0} \frac{6(q_0 - 1) + z[-5 - 2j_0 + q_0(8 + 3q_0)]}{-2(3 + z + j_0z) + 2q_0(3 + z + 3zq_0)} \quad (\text{C.1})$$

$$H^{P_{21}}(z) = H_0(3(j_0^2 - q_0^4) + 2q_0s_0)z^2 + (-12q_0^3 + 2s_0)z(1 + z) - 6q_0^2(1 + z)^2 + 2j_0(3 + (6 + 7q_0)z + (3 + 7q_0 + q_0^2)z^2) / (-6q_0^3z + 2s_0z - 6q_0^2(1 + z) + j_0(6 + (6 + 8q_0)z)) \quad (\text{C.2})$$

P_{22} equations of the luminosity distance and the Hubble rate:

$$d_L^{P_{22}}(z) = \frac{cz}{H_0} 6[10 + 9z - 6q_0 + q_0^2z + s_0z - 2q_0^2(3 + 7z) - q_0(16 + 19z) + j_0(4 + (9 + 6q_0)z)]\{60 + 24z + 6s_0z - 2z^2 + 4j_0^2z^2 - 9q_0^4z^2 - 3s_0z^2 + 6q_0^3z(-9 + 4z) + q_0^2(-36 - 114z + 19z^2) + j_0[24 + 6(7 + 8q_0)z + z^2(-7 - 23q_0 + 6q_0^2)] + q_0[-96 - 36z + z^2(4 + 3s_0)]\}^{-1} \quad (\text{C.3})$$

$$H^{P_{22}}(z) = H_0(24s_0 + 6l_0z + 72s_0z + 30j_0^3z^2 + 6l_0z^2 - 45q_0^6z^2 + 48s_0z^2 + 4s_0^2z^2 - 90q_0^5z(1 + 2z) - 18q_0^4(2 + 21z + 21z^2) + j_0^2(36 + 12(4 + 5q_0)z + (48 + 120q_0 - 5q_0^2)z^2) + 3q_0^3(-48 - 144z + (-96 + 5s_0)z^2) + 9q_0^2(-8 + 2(-8 + 3s_0)z + (-8 + l_0 + 12s_0)z^2) + 6q_0(l_0z(1 + 2z) + s_0(4 + 23z + 23z^2)) + j_0(60q_0^4z^2 + 90q_0^3z(1 + 2z) + 6q_0^2(4 + 77z + 77z^2) + 7q_0(24 + 72z + (48 + 5s_0)z^2) + 3(24 + 4(12 + s_0)z + (24l_0 + 8s_0)z^2)) / (24s_0 + 6l_0z - 54q_0^5z + 48s_0z + 12j_0^3z^2 - 9q_0^6z^2 + 4s_0^2z^2 - 18q_0^4(2 + 11z) + 3q_0^2(-24 + 2(-12 + 5s_0)z + l_0z^2) + j_0^2(36 + 12(1 + 2q_0)z - 23q_0^2z^2) - 3q_0^3(48 + 72z + s_0z^2) + 6q_0(l_0z + s_0(4 + 15z)) + j_0(72 + 66q_0^3z + 12(6 + s_0)z - 3l_0z^2 + 24q_0^4z^2 + 6q_0^2(4 + 45z) + q_0(168 + 264z + 11s_0z^2)))) \quad (\text{C.4})$$

P_{32} equations of the luminosity distance and the Hubble rate:

$$\begin{aligned}
 d_L^{P_{32}(z)} = \frac{cz}{H_0} & \left\{ -120 - 180s_0 - 156z - 36l_0z - 426s_0z - 40z^2 + 80j_0^3z^2 - 30l_0z^2 - 135q_0^6z^2 - \right. \\
 & 210s_0z^2 + 15s_0^2z^2 - 270q_0^5z(3 + 4z) + 9q_0^4(-60 + 50z + 63z^2) + 2q_0^3(720 + 1767z + 887z^2) \\
 & + 3j_0^2(80 + 20(13 + 2q_0)z + (177 + 40q_0 - 60q_0^2)z^2) + 6q_0^2[190 + 5(67 + 9s_0)z + (125 + 3l_0 \\
 & + 58s_0)z^2] - 6q_0[s_0(-30 + 4z + 17z^2) - 2(20 + (31 + 3l_0)z + (9 + 4l_0)z^2)] + 6j_0[-70 + \\
 & (-127 + 10s_0)z + 45q_0^4z^2 + (-47 - 2l_0 + 13s_0)z^2 + 5q_0^3z(30 + 41z) - 3q_0^2(-20 + 75z + \\
 & 69z^2) + 2q_0(-115 - 274z + (-136 + 5s_0)z^2)] \left. \right\} \left\{ 3[-40 - 60s_0 - 32z - 12l_0z - 112s_0z4z^2 + \right. \\
 & 40j_0^3z^2 - 4l_0z^2 - 135q_0^6z^2 - 24s_0z^2 + 5s_0^2z^2 - 30q_0^5z(12 + 5z) + 3q_0^4(-60 + 160z + 71z^2) + \\
 & j_0^2(80 + 20(11 + 4q_0)z + (57 + 20q_0 - 40q_0^2)z^2) + 6q_0^3(80 + 188z + (44 + 5s_0)z^2) + 2q_0^2(190 \\
 & + 20(13 + 3s_0)z + (46 + 6l_0 + 21s_0)z^2) + 4q_0(20 + (16 + 3l_0)z + (2 + l_0)z^2 + s_0(15 - 17z \\
 & - 9z^2)) + 2j_0(-70 + 2(-46 + 5s_0)z + 90q_0^4z^2 + (-16 - 2l_0 + 3s_0)z^2 + 15q_0^3z(12 + 5z) + \\
 & \left. q_0^2(60 - 370z - 141z^2) + 2q_0(-115 - 234z + 2(-26 + 5s_0)z^2)] \right\}^{-1}
 \end{aligned}
 \tag{C.5}$$

$$\begin{aligned}
 H^{P_{32}}(z) = & cH_0\{-540q_0^6 - 180q_0^3s_0 + 240s_0^2 + 36p_0q_0^2z - 1620q_0^6z - 1620q_0^7z - 540q_0^3s_0z - \\
 & 180q_0^4s_0z + 720s_0^2z + 660q_0s_0^2z + 72p_0q_0^2z^2 + 72p_0q_0^3z^2 - 1620q_0^6z^2 - 3240q_0^7z^2 - 1215q_0^8z^2 \\
 & - 12p_0s_0z^2 - 540q_0^3s_0z^2 - 360q_0^4s_0z^2 + 360q_0^5s_0z^2 + 720s_0^2z^2 + 1320q_0s_0^2z^2 + 315q_0^2s_0^2z^2 + \\
 & 36p_0q_0^2z^3 + 72p_0q_0^3z^3 + 18p_0q_0^4z^3 - 540q_0^6z^3 - 1620q_0^7z^3 - 1215q_0^8z^3 - 135q_0^9z^3 - 12p_0s_0z^3 \\
 & - 12p_0q_0s_0z^3 - 180q_0^3s_0z^3 - 180q_0^4s_0z^3 + 360q_0^5s_0z^3 + 270q_0^6s_0z^3 + 240s_0^2z^3 + 660q_0s_0^2z^3 + \\
 & 315q_0^2s_0^2z^3 - 45q_0^3s_0^2z^3 - 40s_0^3z^3 + 15l_0^2z^2(1+z+q_0z) + 60j_0^4z^2(10+(10+9q_0)z) + 10j_0^3 \times \\
 & \times (72+12(18+19q_0)z+3(72+152q_0+29q_0^2)z^2+(72+228q_0+87q_0^2-82q_0^3+3s_0)z^3) \\
 & + 6l_0(-12q_0^5z^3+12q_0^4z^2(1+z)+23q_0s_0z^2(1+z)+66q_0^3z(1+z)^2+10s_0z(1+z)^2+3q_0^2 \times \\
 & \times (10+30z+30z^2+(10+s_0)z^3)) + 6j_0(45q_0^7z^3+600q_0^6z^2(1+z)-105q_0^3s_0z^2(1+z)+ \\
 & 780q_0^5z(1+z)^2-120q_0^4(-2-6z-6z^2+(-2+s_0)z^3)+l_0(-30-2(45+28q_0)z+(-90 \\
 & -112q_0+41q_0^2)z^2+(-30-56q_0+41q_0^2+33q_0^3+10s_0)z^3)-2z(1+z)(-25s_0^2z+3p_0(1 \\
 & +z))+2q_0^2(-p_0z^2+95s_0(1+z)^2)+2q_0(10s_0^2z^3-7p_0z^2(1+z)+55s_0(1+z)^3))+3j_0^2 \times \\
 & \times (75q_0^5z^3-1125q_0^4z^2(1+z)-1580q_0^3z(1+z)^2+20q_0^2(-23-69z-69z^2+(-23+10 \times \\
 & \times_0)z^3)+2q_0z^2(-13l_0z+225s_0(1+z))+2z(50s_0(1+z)^2-z(3p_0z+35l_0(1+z))))\}\{3(- \\
 & 180q_0^6-60q_0^3s_0+80s_0^2+12p_0q_0^2z-360q_0^6z-360q_0^7z-120q_0^3s_0z+160s_0^2z+140q_0s_0^2z+ \\
 & 80j_0^4z^2+5l_0^2z^2+12p_0q_0^2z^2+12p_0q_0^3z^2-180q_0^6z^2-360q_0^7z^2-135q_0^8z^2-4p_0s_0z^2-60q_0^3s_0z^2 \\
 & +90q_0^5s_0z^2+80s_0^2z^2+140q_0s_0^2z^2+5q_0^2s_0^2z^2+40j_0^3(6+(12+13q_0)z+(6+13q_0+3q_0^2)z^2) \\
 & +l_0(-18q_0^4z^2+26q_0s_0z^2+72q_0^3z(1+z)+20s_0z(1+z)+60q_0^2(1+z)^2)-5j_0^2(8l_0z^2+95 \times \\
 & \times q_0^4z^2-48q_0s_0z^2+224q_0^3z(1+z)-20s_0z(1+z)+92q_0^2(1+z)^2)+2j_0(225q_0^6z^2-115q_0^3 \times \\
 & \times s_0z^2+540q_0^5z(1+z)+80q_0^2s_0z(1+z)+240q_0^4(1+z)^2-6z(p_0+p_0z-5s_0^2z)+l_0(-30 \\
 & -2(30+13q_0)z+(-30-26q_0+37q_0^2)z^2)+2q_0(-4p_0z^2+55s_0(1+z)^2)\}\}^{-1}
 \end{aligned}
 \tag{C.6}$$

Bibliography

- [1] Kyle Barbary, Rbiswas4, Danny Goldstein, et al. sncosmo/sncosmo: v1.4.0, November 2016.
- [2] Daniel Foreman-Mackey, David W. Hogg, Dustin Lang, and Jonathan Goodman. emcee: The mcmc hammer. *Publications of the Astronomical Society of the Pacific*, 125(925):306, feb 2013.
- [3] Henrietta S. Leavitt. 1777 variables in the Magellanic Clouds. *Annals of Harvard College Observatory*, 60:87–108.3, January 1908.
- [4] V. M. Slipher. Spectrographic Observations of Nebulae. *Popular Astronomy*, 23:21–24, January 1915.
- [5] Edwin Hubble. A Relation between Distance and Radial Velocity among Extra-Galactic Nebulae. *Proceedings of the National Academy of Science*, 15(3):168–173, March 1929.
- [6] Edwin Hubble and Milton L. Humason. The Velocity-Distance Relation among Extra-Galactic Nebulae. *The Astrophysical Journal*, 74:43, July 1931.
- [7] M. Fukugita, C. J. Hogan, and P. J. E. Peebles. The cosmic distance scale and the hubble constant. *Nature*, 366, nov 1993.
- [8] Planck Collaboration, N. Aghanim, Y. Akrami, et al. Planck 2018 results. VI. Cosmological parameters. *Astronomy & Astrophysics*, 641:A6, September 2020.
- [9] N. Aghanim et al. Planck 2018 results. V. CMB power spectra and likelihoods. *Astron. Astrophys.*, 641:A5, 2020.
- [10] Florian Beutler, Chris Blake, Matthew Colless, D.Heath Jones, Lister Staveley-Smith, Lachlan Campbell, Quentin Parker, Will Saunders, and Fred Watson. The 6dF Galaxy Survey: Baryon Acoustic Oscillations and the Local Hubble Constant. *Mon. Not. Roy. Astron. Soc.*, 416:3017–3032, 2011.
- [11] Ashley J. Ross, Lado Samushia, Cullan Howlett, Will J. Percival, Angela Burden, and Marc Manera. The clustering of the SDSS DR7 main Galaxy sample – I. A 4 per cent distance measure at $z = 0.15$. *Mon. Not. Roy. Astron. Soc.*, 449(1):835–847, 2015.

Bibliography

- [12] Shadab Alam et al. The clustering of galaxies in the completed SDSS-III Baryon Oscillation Spectroscopic Survey: cosmological analysis of the DR12 galaxy sample. *Mon. Not. Roy. Astron. Soc.*, 470(3):2617–2652, 2017.
- [13] Raul Jimenez and Abraham Loeb. Constraining cosmological parameters based on relative galaxy ages. *Astrophys. J.*, 573:37–42, 2002.
- [14] Joan Simon, Licia Verde, and Raul Jimenez. Constraints on the redshift dependence of the dark energy potential. *Phys. Rev. D*, 71:123001, 2005.
- [15] Daniel Stern, Raul Jimenez, Licia Verde, Marc Kamionkowski, and S.Adam Stanford. Cosmic Chronometers: Constraining the Equation of State of Dark Energy. I: $H(z)$ Measurements. *JCAP*, 02:008, 2010.
- [16] Michele Moresco. Raising the bar: new constraints on the Hubble parameter with cosmic chronometers at $z \sim 2$. *Mon. Not. Roy. Astron. Soc.*, 450(1):L16–L20, 2015.
- [17] Cong Zhang, Han Zhang, Shuo Yuan, Tong-Jie Zhang, and Yan-Chun Sun. Four new observational $H(z)$ data from luminous red galaxies in the Sloan Digital Sky Survey data release seven. *Res. Astron. Astrophys.*, 14(10):1221–1233, 2014.
- [18] Michele Moresco, Lucia Pozzetti, Andrea Cimatti, Raul Jimenez, Claudia Maraston, Licia Verde, Daniel Thomas, Annalisa Citro, Rita Tojeiro, and David Wilkinson. A 6% measurement of the Hubble parameter at $z \sim 0.45$: direct evidence of the epoch of cosmic re-acceleration. *JCAP*, 05:014, 2016.
- [19] A.L. Ratsimbazafy, S.I. Loubser, S.M. Crawford, C.M. Cress, B.A. Bassett, R.C. Nichol, and P. Väisänen. Age-dating Luminous Red Galaxies observed with the Southern African Large Telescope. *Mon. Not. Roy. Astron. Soc.*, 467(3):3239–3254, 2017.
- [20] M. Moresco et al. Improved constraints on the expansion rate of the Universe up to $z \sim 1.1$ from the spectroscopic evolution of cosmic chronometers. *JCAP*, 08:006, 2012.
- [21] B. F. Schutz. Determining the Hubble constant from gravitational wave observations. *Nature*, 323(6086):310–311, September 1986.
- [22] B. P. Abbott, R. Abbott, T. D. Abbott, et al. A gravitational-wave standard siren measurement of the Hubble constant. *Nature*, 551(7678):85–88, November 2017.
- [23] Wendy L. Freedman, Barry F. Madore, Brad K. Gibson, et al. Final results from the hubble space telescope key project to measure the hubble constant*. *The Astrophysical Journal*, 553(1):47, may 2001.

Bibliography

- [24] Adam G. Riess, Lucas Macri, Stefano Casertano, et al. A Redetermination of the Hubble Constant with the Hubble Space Telescope from a Differential Distance Ladder. *The Astrophysical Journal*, 699(1):539–563, July 2009.
- [25] Adam G. Riess, Lucas Macri, Stefano Casertano, Hubert Lampeitl, Henry C. Ferguson, Alexei V. Filippenko, Saurabh W. Jha, Weidong Li, and Ryan Chornock. A 3% Solution: Determination of the Hubble Constant with the Hubble Space Telescope and Wide Field Camera 3. *The Astrophysical Journal*, 730(2):119, April 2011.
- [26] Wendy L. Freedman, Barry F. Madore, Victoria Scowcroft, Chris Burns, Andy Monson, S. Eric Persson, Mark Seibert, and Jane Rigby. Carnegie hubble program: A mid-infrared calibration of the hubble constant. *The Astrophysical Journal*, 758(1):24, sep 2012.
- [27] Adam G. Riess, Lucas M. Macri, Samantha L. Hoffmann, et al. A 2.4% Determination of the Local Value of the Hubble Constant. *The Astrophysical Journal*, 826(1):56, July 2016.
- [28] A. Riess. The expansion of the universe is faster than expected. *Nature Reviews Physics*, jan 2020.
- [29] Wendy L. Freedman, Barry F. Madore, Taylor Hoyt, et al. Calibration of the tip of the red giant branch. *The Astrophysical Journal*, 891(1):57, mar 2020.
- [30] Adam G. Riess, Stefano Casertano, Wenlong Yuan, J. Bradley Bowers, Lucas Macri, Joel C. Zinn, and Dan Scolnic. Cosmic distances calibrated to 1and hubble space telescope photometry of 75 milky way cepheids confirm tension with λ cdm. *The Astrophysical Journal Letters*, 908(1):L6, feb 2021.
- [31] Adam G. Riess, Wenlong Yuan, Lucas M. Macri, et al. A comprehensive measurement of the local value of the hubble constant with $1 \text{ km s}^{-1} \text{ mpc}^{-1}$ uncertainty from the hubble space telescope and the sh0es team. *The Astrophysical Journal Letters*, 934(1):L7, July 2022.
- [32] J. C. Mather, E. S. Cheng, Jr. Eplee, R. E., et al. A Preliminary Measurement of the Cosmic Microwave Background Spectrum by the Cosmic Background Explorer (COBE) Satellite. *Astrophysical Journal Letters*, 354:L37, May 1990.
- [33] G. F. Smoot, C. L. Bennett, A. Kogut, et al. Structure in the COBE Differential Microwave Radiometer First-Year Maps. *Astrophysical Journal Letters*, 396:L1, September 1992.

Bibliography

- [34] J. C. Mather, E. S. Cheng, D. A. Cottingham, et al. Measurement of the Cosmic Microwave Background Spectrum by the COBE FIRAS Instrument. *Astrophysical Journal*, 420:439, January 1994.
- [35] E. Komatsu, J. Dunkley, M. R. Nolta, C. L. Bennett, B. Gold, G. Hinshaw, N. Jarosik, D. Larson, M. Limon, L. Page, D. N. Spergel, M. Halpern, R. S. Hill, A. Kogut, S. S. Meyer, G. S. Tucker, J. L. Weiland, E. Wollack, and E. L. Wright. Five-year wilkinson microwave anisotropy probe* observations: Cosmological interpretation. *The Astrophysical Journal Supplement Series*, 180(2):330, feb 2009.
- [36] Planck Collaboration, Aghanim, N., Armitage-Caplan, C., et al. Planck 2013 results. xxvii. doppler boosting of the cmb: Eppur si muove. *A&A*, 571:A27, 2014.
- [37] Planck Collaboration, P.A.R. Ade, N. Aghanim, et al. Planck 2015 results. xiii. cosmological parameters. *Astronomy & Astrophysics*, 594:A13, September 2016.
- [38] Suhail Dhawan, Stephen Thorp, Kaisey S Mandel., et al. A BayeSN distance ladder: H_0 from a consistent modelling of Type Ia supernovae from the optical to the near-infrared. *Monthly Notices of the Royal Astronomical Society*, 524(1):235–244, September 2023.
- [39] Wendy L. Freedman and Barry F. Madore. Progress in direct measurements of the hubble constant. *Journal of Cosmology and Astroparticle Physics*, 2023(11):050, nov 2023.
- [40] Wendy L. Freedman. Correction: Cosmology at a crossroads. *Nature Astronomy*, 1:0169, June 2017.
- [41] Martín López-Corredoira. Hubble tensions: a historical statistical analysis. *Monthly Notices of the Royal Astronomical Society*, 517(4):5805–5809, 11 2022.
- [42] Sean M. Carroll. The Cosmological constant. *Living Rev. Rel.*, 4:1, 2001.
- [43] Varun Sahni and Alexei A. Starobinsky. The Case for a positive cosmological Lambda term. *Int. J. Mod. Phys. D*, 9:373–444, 2000.
- [44] S. Capozziello, R. Lazkoz, and V. Salzano. Comprehensive cosmographic analysis by markov chain method. *Phys. Rev. D*, 84:124061, Dec 2011.
- [45] Salvatore Capozziello and Mauro Francaviglia. Extended Theories of Gravity and their Cosmological and Astrophysical Applications. *Gen. Rel. Grav.*, 40:357–420, 2008.

Bibliography

- [46] Kazuharu Bamba, Salvatore Capozziello, Shin'ichi Nojiri, and Sergei D. Odintsov. Dark energy cosmology: the equivalent description via different theoretical models and cosmography tests. *Astrophys. Space Sci.*, 342:155–228, 2012.
- [47] S. Nojiri, S. D. Odintsov, and V. K. Oikonomou. Modified Gravity Theories on a Nutshell: Inflation, Bounce and Late-time Evolution. *Phys. Rept.*, 692:1–104, 2017.
- [48] Arman Shafieloo, Ujjaini Alam, Varun Sahni, and Alexei A. Starobinsky. Smoothing Supernova Data to Reconstruct the Expansion History of the Universe and its Age. *Mon. Not. Roy. Astron. Soc.*, 366:1081–1095, 2006.
- [49] Varun Sahni, Arman Shafieloo, and Alexei A. Starobinsky. Two new diagnostics of dark energy. *Phys. Rev. D*, 78:103502, 2008.
- [50] Ruth A. Daly and S. G. Djorgovski. A model-independent determination of the expansion and acceleration rates of the universe as a function of redshift and constraints on dark energy. *Astrophys. J.*, 597:9–20, 2003.
- [51] Benjamin L'Huillier, Arman Shafieloo, and Hyungjin Kim. Model-independent cosmological constraints from growth and expansion. *Mon. Not. Roy. Astron. Soc.*, 476(3):3263–3268, 2018.
- [52] A. A. Penzias and R. W. Wilson. A Measurement of Excess Antenna Temperature at 4080 Mc/s. *Astrophysical Journal*, 142:419–421, July 1965.
- [53] R. H. Dicke, P. J. E. Peebles, P. G. Roll, and D. T. Wilkinson. Cosmic Black-Body Radiation. *Astrophysical Journal*, 142:414–419, July 1965.
- [54] R. A. Alpher, H. Bethe, and G. Gamow. The Origin of Chemical Elements. *Physical Review*, 73(7):803–804, April 1948.
- [55] R. K. Sachs and A. M. Wolfe. Perturbations of a Cosmological Model and Angular Variations of the Microwave Background. *Astrophysical Journal*, 147:73, January 1967.
- [56] P. J. E. Peebles and J. T. Yu. Primeval Adiabatic Perturbation in an Expanding Universe. *Astrophysical Journal*, 162:815, December 1970.
- [57] Ya. B. Zeldovich and R. A. Sunyaev. The Interaction of Matter and Radiation in a Hot-Model Universe. *Astrophysics and Space Science*, 4(3):301–316, July 1969.
- [58] R. A. Sunyaev and Ya. B. Zeldovich. Small-Scale Fluctuations of Relic Radiation. *Astrophysics and Space Science*, 7(1):3–19, April 1970.

Bibliography

- [59] R. A. Sunyaev and Ya. B. Zeldovich. The Observations of Relic Radiation as a Test of the Nature of X-Ray Radiation from the Clusters of Galaxies. *Comments on Astrophysics and Space Physics*, 4:173, November 1972.
- [60] R. A. Sunyaev and Ia. B. Zeldovich. Microwave background radiation as a probe of the contemporary structure and history of the universe. *Annual review of astronomy and astrophysics*, 18:537–560, January 1980.
- [61] N. Vittorio and J. Silk. Fine-scale anisotropy of the cosmic microwave background in a universe dominated by cold dark matter. *Astrophysical Journal Letters*, 285:L39–L43, October 1984.
- [62] J. R. Bond and G. Efstathiou. Cosmic background radiation anisotropies in universes dominated by nonbaryonic dark matter. *Astrophysical Journal Letters*, 285:L45–L48, October 1984.
- [63] Naoshi Sugiyama. Gauge Invariant Cosmological Perturbations with Cold Dark Matter. *Progress of Theoretical Physics*, 81(5):1021–1036, 05 1989.
- [64] Naoshi Sugiyama and Naoteru Gouda. Perturbations of the Cosmic Microwave Background Radiation and Structure Formations. *Progress of Theoretical Physics*, 88(5):803–844, 11 1992.
- [65] D. J. Fixsen, E. S. Cheng, J. M. Gales, et al. The cosmic microwave background spectrum from the full cobe* firas data set. *The Astrophysical Journal*, 473(2):576, dec 1996.
- [66] D. N. Spergel, L. Verde, H. V. Peiris, et al. First-year wilkinson microwave anisotropy probe (wmap)* observations: Determination of cosmological parameters. *The Astrophysical Journal Supplement Series*, 148(1):175, sep 2003.
- [67] C. L. Bennett, M. Halpern, G. Hinshaw, et al. First-year wilkinson microwave anisotropy probe (wmap)* observations: Preliminary maps and basic results. *The Astrophysical Journal Supplement Series*, 148(1):1, sep 2003.
- [68] Viatcheslav Mukhanov. *Physical Foundations of Cosmology*. Cambridge University Press, 2005.
- [69] Scott Dodelson. *Modern Cosmology*. Academic press, 2003.

Bibliography

- [70] Esteban Ricardo Chalbaud Mogollón. *Efeitos cinemáticos e a quebra de isotropia estatística das flutuações da radiação cósmica de fundo*. Master dissertation, Universidade de São paulo, 2021.
- [71] Antony Lewis and Anthony Challinor. CAMB: Code for Anisotropies in the Microwave Background. Astrophysics Source Code Library, record ascl:1102.026, February 2011.
- [72] Wayne Hu and Scott Dodelson. Cosmic microwave background anisotropies. *Annual Review of Astronomy and Astrophysics*, 40(1):171–216, 2002.
- [73] Pablo Lemos and Paul Shah. The cosmic microwave background and h_0 , 2023.
- [74] Micol Benetti and Salvatore Capozziello. Connecting early and late epochs by $f(z)$ CDM cosmography. *Journal of Cosmology and Astroparticle Physics*, 2019(12):008–008, dec 2019.
- [75] F. Thévenin, M. Falanga, G. Pietrzyński C. Kuo, and M. Yamaguchi. Modern geometric methods of distance determination. *Space Science Reviews*, pages 1572–9672, nov 2017.
- [76] The cosmic distance ladder. <https://www.aavso.org/cosmic-distance-ladder>. Accessed: 2023-11-05.
- [77] The University of Western Australia. Measuring the universe 4: Explanation of the cosmic distance ladder (background sheet). *Spice*, 2011.
- [78] Bradley W. Carroll and Dale A. Ostlie. *An Introduction to Modern Astrophysics*. Pearson New International Edition, 1996.
- [79] Peter Schneider. *Extragalactic Astronomy and Cosmology*. Springer, 2006.
- [80] David W. Hogg, Ivan K. Baldry, Michael R. Blanton, and Daniel J. Eisenstein. The K correction. 10 2002.
- [81] Jay M. Pasachoff and Jason W. Mativi. Demonstrating the Cosmic Distance Ladder with Cepheids. *The Physics Teacher*, 58(1):6–7, 01 2020.
- [82] B. Leibundgut. Type ia supernovae. *The Astronomy and Astrophysics Review*, 10:1432–0754, sep 2000.
- [83] David Branch and GA Tammann. Type ia supernovae as standard candles. *Annual review of astronomy and astrophysics*, 30(1):359–389, 1992.

Bibliography

- [84] M. M. Phillips. The Absolute Magnitudes of Type IA Supernovae. *The Astrophysical Journal Letters*, 413:L105, August 1993.
- [85] Guy, J., Astier, P., Baumont, S., et al. Salt2: using distant supernovae to improve the use of type ia supernovae as distance indicators ^{***}. *Astronomy & Astrophysics*, 466(1):11–21, 2007.
- [86] G Taylor, D O Jones, B Popovic, et al. SALT2 versus SALT3: updated model surfaces and their impacts on type Ia supernova cosmology. *Monthly Notices of the Royal Astronomical Society*, 520(4):5209–5224, 01 2023.
- [87] Dillon Brout and Daniel Scolnic. It’s dust: Solving the mysteries of the intrinsic scatter and host-galaxy dependence of standardized type ia supernova brightnesses. *The Astrophysical Journal*, 909(1):26, mar 2021.
- [88] D. Brout, D. Scolnic, B. Popovic, et al. The pantheon+ analysis: Cosmological constraints. *The Astrophysical Journal*, 938(2):110, oct 2022.
- [89] Roman, M., Hardin, D., Betoule, M., et al. Dependence of type ia supernova luminosities on their local environment. *A&A*, 615:A68, 2018.
- [90] Wendy L. Freedman, Barry F. Madore, Dylan Hatt, et al. The carnegie-chicago hubble program. viii. an independent determination of the hubble constant based on the tip of the red giant branch*. *The Astrophysical Journal*, 882(1):34, aug 2019.
- [91] Gagandeep S. Anand, R. Brent Tully, Luca Rizzi, et al. Comparing tip of the red giant branch distance scales: An independent reduction of the carnegie-chicago hubble program and the value of the hubble constant. *The Astrophysical Journal*, 932(1):15, jun 2022.
- [92] John P. Blakeslee, Joseph B. Jensen, Chung-Pei Ma, et al. The hubble constant from infrared surface brightness fluctuation distances*. *The Astrophysical Journal*, 911(1):65, apr 2021.
- [93] Daniel E. Holz, Scott A. Hughes, and Bernard F. Schutz. Measuring cosmic distances with standard sirens. *Physics Today*, 71(12):34–40, 12 2018.
- [94] A. Palmese, C. R. Bom, S. Mucesh, and W. G. Hartley. A standard siren measurement of the hubble constant using gravitational-wave events from the first three ligo/virgo observing runs and the desi legacy survey. *The Astrophysical Journal*, 943(1):56, jan 2023.

Bibliography

- [95] Dariusz Graczyk, Grzegorz Pietrzyński, Ian B. Thompson, et al. A Distance Determination to the Small Magellanic Cloud with an Accuracy of Better than Two Percent Based on Late-type Eclipsing Binary Stars. *The Astrophysical Journal*, 904(1):13, November 2020.
- [96] G. Pietrzyński, D. Graczyk, A. Gallenne, et al. A distance to the large magellanic cloud that is precise to one per cent. *Nature*, 567(7747):200–203, mar 2019.
- [97] M. J. Reid, D. W. Pesce, and A. G. Riess. An Improved Distance to NGC 4258 and Its Implications for the Hubble Constant. *The Astrophysical Journal Letters*, 886(2):L27, December 2019.
- [98] Dan Scolnic et al. The Pantheon+ Analysis: The Full Data Set and Light-curve Release. *Astrophys. J.*, 938(2):113, 2022.
- [99] Erik R. Peterson, W. D’Arcy Kenworthy, Daniel Scolnic, et al. The pantheon+ analysis: Evaluating peculiar velocity corrections in cosmological analyses with nearby type ia supernovae. *The Astrophysical Journal*, 938(2):112, oct 2022.
- [100] Adam G. Riess, Gagandeep S. Anand, Wenlong Yuan, Stefano Casertano, Andrew Dolphin, Lucas M. Macri, Louise Breuval, Dan Scolnic, Marshall Perrin, and Richard I. Anderson. Crowded no more: The accuracy of the hubble constant tested with high-resolution observations of cepheids by jwst. *The Astrophysical Journal Letters*, 956(1):L18, oct 2023.
- [101] Radoslaw Wojtak and Jens Hjorth. Intrinsic tension in the supernova sector of the local Hubble constant measurement and its implications. *Monthly Notices of the Royal Astronomical Society*, 515(2):2790–2799, 07 2022.
- [102] J. Guy, P. Astier, S. Nobili, N. Regnault, and R. Pain. SALT: a spectral adaptive light curve template for type Ia supernovae. *A&A*, 443(3):781–791, December 2005.
- [103] A. Turmina Petreca, M. Benetti, and S. Capozziello. Beyond λ cdm with $f(z)$ cdm: Criticalities and solutions of padé cosmography. *Physics of the Dark Universe*, 44:101453, 2024.
- [104] Elcio Abdalla et al. Cosmology intertwined: A review of the particle physics, astrophysics, and cosmology associated with the cosmological tensions and anomalies. *Journal of High Energy Astrophysics*, 34:49–211, 2022.

Bibliography

- [105] Bargiacchi, G., Risaliti, G., Benetti, M., et al. Cosmography by orthogonalized logarithmic polynomials. *A&A*, 649, 2021.
- [106] Weiqiang Yang, Eleonora Di Valentino, Supriya Pan, Yabo Wu, and Jianbo Lu. Dynamical dark energy after planck CMB final release and h_0 tension. *Monthly Notices of the Royal Astronomical Society*, 501(4):5845–5858, dec 2020.
- [107] Nandan Roy, Sangita Goswami, and Sudipta Das. Quintessence or phantom: Study of scalar field dark energy models through a general parametrization of the hubble parameter, 2022.
- [108] Ravi Kumar Sharma, Kanhaiya Lal Pandey, and Subinoy Das. Implications of an Extended Dark Energy Model with Massive Neutrinos. *The Astrophysical Journal*, 934(2):113, August 2022.
- [109] Gong-Bo Zhao et al. Dynamical dark energy in light of the latest observations. *Nature Astronomy*, 1:627–632, August 2017.
- [110] George Alestas and Leandros Perivolaropoulos. Late-time approaches to the hubble tension deforming $h(z)$, worsen the growth tension. *Monthly Notices of the Royal Astronomical Society*, 504(3):3956–3962, apr 2021.
- [111] Salvatore Capozziello, Rocco D’Agostino, and Orlando Luongo. Extended Gravity Cosmography. *Int. J. Mod. Phys. D*, 28(10):1930016, 2019.
- [112] Ishida, E. E. O. and de Souza, R. S. Hubble parameter reconstruction from a principal component analysis: minimizing the bias. *A&A*, 527:A49, 2011.
- [113] Francisco S. N. Lobo, Jose Pedro Mimoso, and Matt Visser. Cosmographic analysis of redshift drift. *JCAP*, 04:043, 2020.
- [114] Salvatore Capozziello, Ruchika, and Anjan A. Sen. Model independent constraints on dark energy evolution from low-redshift observations. *Mon. Not. Roy. Astron. Soc.*, 484:4484, 2019.
- [115] Christine Gruber and Orlando Luongo. Cosmographic analysis of the equation of state of the universe through Padé approximations. *Phys. Rev. D*, 89(10):103506, 2014.
- [116] S. Capozziello, R. D’Agostino, and O. Luongo. High-redshift cosmography: auxiliary variables versus Padé polynomials. *Mon. Not. Roy. Astron. Soc.*, 494(2):2576–2590, 2020.

Bibliography

- [117] Daniel Stern, Raul Jimenez, Licia Verde, et al. Cosmic Chronometers: Constraining the Equation of State of Dark Energy. I: $H(z)$ Measurements. *JCAP*, 02:008, 2010.
- [118] Michele Moresco. Raising the bar: new constraints on the Hubble parameter with cosmic chronometers at $z \sim 2$. *Mon. Not. Roy. Astron. Soc.*, 450(1):L16–L20, 2015.
- [119] Cong Zhang, Han Zhang, Shuo Yuan, et al. Four new observational $H(z)$ data from luminous red galaxies in the Sloan Digital Sky Survey data release seven. *Res. Astron. Astrophys.*, 14(10):1221–1233, 2014.
- [120] Michele Moresco, Lucia Pozzetti, Andrea Cimatti, et al. A 6% measurement of the Hubble parameter at $z \sim 0.45$: direct evidence of the epoch of cosmic re-acceleration. *JCAP*, 05:014, 2016.
- [121] A.L. Ratsimbazafy, S.I. Loubser, S.M. Crawford, et al. Age-dating Luminous Red Galaxies observed with the Southern African Large Telescope. *Mon. Not. Roy. Astron. Soc.*, 467(3):3239–3254, 2017.
- [122] M. Moresco et al. Improved constraints on the expansion rate of the Universe up to $z \sim 1.1$ from the spectroscopic evolution of cosmic chronometers. *JCAP*, 08:006, 2012.
- [123] Koushik Dutta, Anirban Roy, Ruchika, et al. Cosmology with low-redshift observations: No signal for new physics. *Phys. Rev. D*, 100(10):103501, 2019.
- [124] Ya-Nan Zhou, De-Zi Liu, Xiao-Bo Zou, and Hao Wei. New generalizations of cosmography inspired by the Padé approximant. *Eur. Phys. J. C*, 76(5):281, 2016.
- [125] Yang Liu, Zhengxiang Li, Hongwei Yu, and Puxun Wu. Bias of reconstructing the dark energy equation of state from the Padé cosmography. *Astrophys. Space Sci.*, 366(11):112, 2021.
- [126] Koushik Dutta, Ruchika, Anirban Roy, Anjan A. Sen, and M. M. Sheikh-Jabbari. Beyond Λ CDM with low and high redshift data: implications for dark energy. *Gen. Rel. Grav.*, 52(2):15, 2020.
- [127] N. Aghanim et al. Planck 2018 results. VIII. Gravitational lensing. *Astron. Astrophys.*, 641:A8, 2020.
- [128] Dan Scolnic et al. The Pantheon+ Analysis: The Full Data Set and Light-curve Release. *Astrophys. J.*, 938(2):113, 2022.

Bibliography

- [129] Dillon Brout et al. The Pantheon+ Analysis: Cosmological Constraints. *Astrophys. J.*, 938(2):110, 2022.
- [130] Adam G. Riess et al. A Comprehensive Measurement of the Local Value of the Hubble Constant with $1 \text{ km s}^{-1} \text{ Mpc}^{-1}$ Uncertainty from the Hubble Space Telescope and the SH0ES Team. *Astrophys. J. Lett.*, 934(1):L7, 2022.
- [131] Antony Lewis, Anthony Challinor, and Anthony Lasenby. Efficient computation of CMB anisotropies in closed FRW models. *Astrophys. J.*, 538:473–476, 2000.
- [132] Antony Lewis and Sarah Bridle. Cosmological parameters from CMB and other data: A Monte Carlo approach. *Phys. Rev. D*, 66:103511, 2002.
- [133] Adam G. Riess, Stefano Casertano, Wenlong Yuan, Lucas M. Macri, and Dan Scolnic. Large Magellanic Cloud Cepheid Standards Provide a 1% Foundation for the Determination of the Hubble Constant and Stronger Evidence for Physics beyond Λ CDM. *Astrophys. J.*, 876(1):85, 2019.
- [134] Rocco D’Agostino and Rafael C. Nunes. Cosmographic view on the H_0 and σ_8 tensions. *Phys. Rev. D*, 108(2):023523, 2023.
- [135] W. Yuan, L. M. Macri, B. M. Peterson, A. G. Riess, M. M. Fausnaugh, S. L. Hoffmann, G. S. Anand, M. C. Bentz, E. Dalla Bontà, R. I. Davies, G. De Rosa, L. Ferrarese, C. J. Grier, E. K. S. Hicks, C. A. Onken, R. W. Pogge, T. Storchi-Bergmann, and M. Vestergaard. The cepheid distance to the narrow-line seyfert 1 galaxy ngc 4051. *The Astrophysical Journal*, 913(1):3, may 2021.
- [136] Max Pettini and Bernard E. J. Pagel. $[\text{O iii}]/[\text{N ii}]$ as an abundance indicator at high redshift. *Monthly Notices of the Royal Astronomical Society*, 348(3):L59–L63, 03 2004.